UNIVERSITY OF CALGARY

Processing of Multicomponent Seismic Data from West-Central Alberta

by

Hussain Aldhaw

A THESIS

SUBMITTED TO THE FACULTY OF GRADUATE STUDIES

IN PARTIAL FULFILMENT OF THE REQUIREMENTS FOR THE

DEGREE OF MASTER OF SCIENCE

GRADUATE PROGRAM IN GEOLOGY AND GEOPHYSICS

CALGARY, ALBERTA

NOVEMBER, 2019

Abstract

Bigstone 3C3D was acquired in 2014 near Fox Creek, Alberta. The total volume acquired is 200 sq. km. A portion of approximately 44 sq.km. of the total volume is selected and processed for PP and PS data from geometry to post stack time migration, including registering the events of P-P and P-S data. However, near surface is generally challenging for the P-S data as it is hard to pick first breaks. That is also related to velocity analysis as statics and velocity are dependent to each other.

In order to overcome this obstacle, we did further investigation to the near surface and used well data with P-wave velocities to give an optimum processed P-S data.

In addition, we investigated the binning of P-P and P-S synthetic data based on a nearby well to test the binning effect on some seismic attributes such as fold, azimuth distribution, offset distribution, etc.

Acknowledgement

I would like to thank everybody who helped with this project, mainly Dr. Donald Lawton who supervised through out the whole project. Also, I would like to thank Helen Isaac for being patient with answering all my questions regarding ProMax. Same thing goes to Kevin Hall for his patience to figure out all the mistakes I did to the system, and for helping with other technical stuff related to Linux and Vista.

I would like also to extend my gratitude to Eagle Canada Inc. for acquiring the data used in this project and making it available.

Also, I would like to thank all of CREWES students and faculty who contributed to this project with explaining some theoretical aspects, answering questions, offering a piece of information or just with a smile.

Lastly, I would like to thank Saudi Aramco for offering this scholarship to pursue my M.S. and funding me through these awesome two years spent here in Calgary.

Table of Contents

List of Tables

List of Figures and Illustrations

List of Symbols, Abbreviation and Nomenclature

Symbol	Definition
*	Convolution
Δt	Trace difference
1D	One dimesion
3C	Three component
3D	Three dimensions
ACP	Asymototе Conversion Point
CCP	Common Coversion Point
CDP	Common depth point
CMP	Common mid-point
CNA	Coherent noise attenuation
db	Decibel
DMO	Dip move-out
E-W	East - West
f	Frequency
f-k	Frequency - Wavenumber
f-x	Frequency - Distance
H1	First horizontal component
H2	Second horizontal component
Hz	Hertz
m/s	Meter per second

ms .... Millisecond

NMO .... Normal move-out

N-S .... North - South

ϴ .... Theta

P wave .... Compressional wave

P-S .... Compressional shear wave

QC .... Quality control

r .... Reflectivity time series

R .... Radial component

RMS .... Root mean square

S .... Synthetic seismogram

S wave .... Shear wave

SCAC .... Surface consistent amplitude scaling

sq.km .... squared kilometer

S-S .... Shear - shear wave

T .... Transverse component

v .... Velocity

V_p .... Compressional wave velocity

V_s .... Shear wave velocity

w .... wavelet

X .... Source to conversion point offset

Xp .... Total source - receiver offset

Chapter One: **Introduction**

1.1 Introduction

Converted shear waves (P-S) is the case where P wave travels downward and the S wave reflects upward. This leads to having a different asymmetric ray path geometry compared to the common symmetric P wave reflection points. Because the reflection angle of the converted wave is smaller than the incidence angle, the reflection closer to the receiver than P wave reflection point. This geometry is given by Snell's law. However, because we have asymmetric reflection points coming from different offsets, amplitudes differ from one reflection point to another. That is why there is another aspect we should take in account when dealing with P-S wave propagation, which is the amplitude variation with offset described by Zoeppritz equations (Stewart et al, 2002).

P-S wave processing is important for couple of reasons, including: creating a correct and clear 3D depth image is not attainable in some cases using P waves alone, especially when two layers have similar P wave properties, making a low-reflectivity interface (Stewart et al, 2002). Here might be a higher S-wave contrast between the two layers that yields a higher reflectivity interface. Also, P-S acquisition is cheaper than S-S for example, because S-S listening times in recording are much longer than P-S, which makes it costly. Lastly, the reason why a lot of researchers are showing interests in P-S surveys is because P-S surveys now are relatively inexpensive, broadly applicable and effective in obtaining S-wave information.

When it comes to acquisition, the asymmetrical geometry of P-S propagation leads to illumination differences in the subsurface than what is expected in the P wave data (Stewart et al, 2002). This should be taken into account in addition to other factors like the effect of anisotropy, crooked lines, etc. Also, 3C geophones are required. Yet the recording of land and marine multicomponent data still constrained by some factors such as the short supply of some of the equipment.

Data processing is also an important step when dealing with P-S data, because there are many factors, methods, approaches and solutions to consider, starting from geometry all the way to migration. For example, one of the methods used before was called the “asymptotic binning” where the whole trace is put at the location defined by a reflector depth that is large compared to the source-receiver offset (Lawton, 1993). Other issues are the static corrections. Large and variable statics have an undesirable effect on PS data, causing attenuation which is a limitation of surface P-S analysis. For P and S event separation, filtering methods such as f-k filtering and match-filters are used to remove P-S reflections from the vertical geophone data. For NMO analysis, a shifted hyperbola was introduced to correct the offset travel-time accurately. This method suggests including a fourth order term in the moveout equation. After NMO, comes another important step which is the Fresnel zone (averaging aperture) that decides which P-S data to be migrated (Stewart et al, 2002). All show the importance of the processing stage in every step, or every parameter, can lead to a big difference in frequency content, amplitude, coherence or event location.

1.2 Thesis objectives

The main goal of this thesis was to process a portion of a large 3C 3D data set and to show the value of multicomponent seismic data for subsurface imaging and rock properties for both P-

P and P-S data. These data can also be use for micro seismic focal depth investigation in the area. This was accomplished by the following tasks:

- Constructing a surface consistent workflow to process the P-P wave data to migration, and a workflow for P-S wave data that images the surface as accurately as possible. This workflow preserves the amplitudes and frequency content of the data.
- Evaluating the survey design and acquisition parameters of 3C 3D Bigstone.
- Investigating the shallow data of the radial component for detailed velocity analysis.
- Registering events in the P-S data with P-P data.
- Testing the optimum binning for P-S synthetic data to understand the fold distribution, illumination and other attributes.

1.3 Thesis structure

The structure of thesis includes six chapters. The first chapter gives a brief introduction of multicomponent seismic surveys and data. In addition, it goes through the basic information of the data used in this project. The second chapter explains the theory of each step used in processing both P-P and P-S data. The third chapter covers the evaluation of different seismic attributes such as fold and illumination of synthetic P-P and P-S data using varying acquisition and binning parameters. The fourth chapter walks us through the P-P data processing and showing examples of shot gathers and stacks before and after each step. The fifth chapter covers the processing of P-S data with the emphasize on the steps that are different from P-P processing workflow. Finally, the sixth chapter provides the conclusions of this project.

1.4 Data

The original size of the Bigstone 3C 3D survey is approximately 200 sq.km as shown in the schematic survey map in Figure 1.1. It is located in Alberta, but the exact study location is confidential. Only a smaller segment of the full area is selected for this thesis. The segmented area is approximately 44 sq.km as shown in the geometry map in Figure 1.2, and it was selected based on several reasons; there is a nearby well that will help during some of the processing steps such as velocity analysis. Also, a lot of interpretation work has already been undertaken in the same area by (Weir et al, 2018). Moreover, the area has micro seismic activity that could be incorporated in the output of this project.

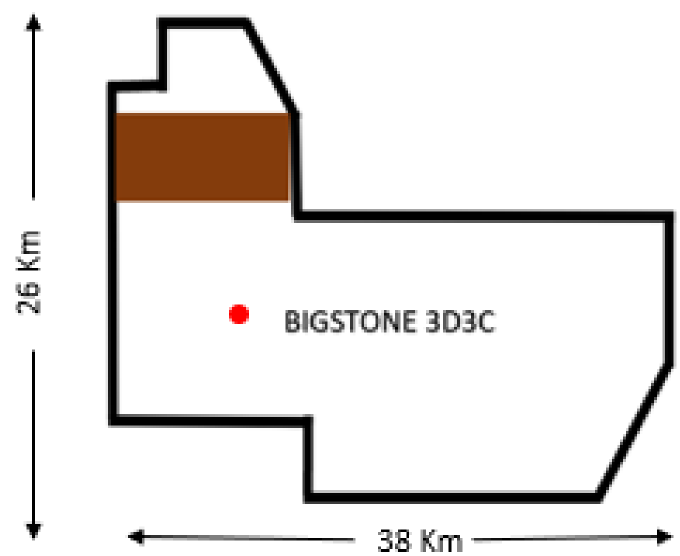

Figure 1.1: Bigstone 3C 3D schematic project map, the shaded area is the selected area for this thesis

1.5 Acquisition Parameters

Table 1.1: General Acquisition Parameters for the 3C 3D Bigstone survey

Survey Type	Orthogonal
Surface Area	44 Sq.Km
Widest Survey E-W	8 Km
Widest Survey N-S	5.5 Km
Bin Size	30 m x 30 m

Table 1.2: Recording Parameters for 3C 3D Bigstone survey

Sample Rate	1 ms
Record Length	5 seconds
Low Cut Filter	3 Hz
High Cut Filter	400 Hz
Geophone Type	Accelerometer

Table 1.3: Receiver Parameters for 3C 3D Bigstone survey

Direction	N-S
Group Interval	60 m
Receiver Line Interval	360 m
Number of Receiver Lines	23

Table 1.4: Source Parameters for 3C 3D Bigstone survey

Direction	E-W
Type	Dynamite
Hole Depth	12 m
Charge Size	3 kg
Source Interval	60 m
Source Line Interval	420 m
Number of Source Lines	12

1.6 Well Data

There is one well located in the south of the chosen area. The well data available from this well are caliper, density, sonic and gamma ray logs.

1.7 Software

Promax SeisSpace was used to process the 3C 3D data set. For the optimum binning test for the P-S synthetic data, SYNGRAM was used to create synthetic gathers from well log data and PS Design was used to simulate P-S surveys and to study the seismic attributes. Finally, VISTA was used to condition the data including segmenting it and editing its headers, and also used to create ACP and CCP stacks. Finally, TomoPlus was used to calculate statics for the vertical component data using first break picks.

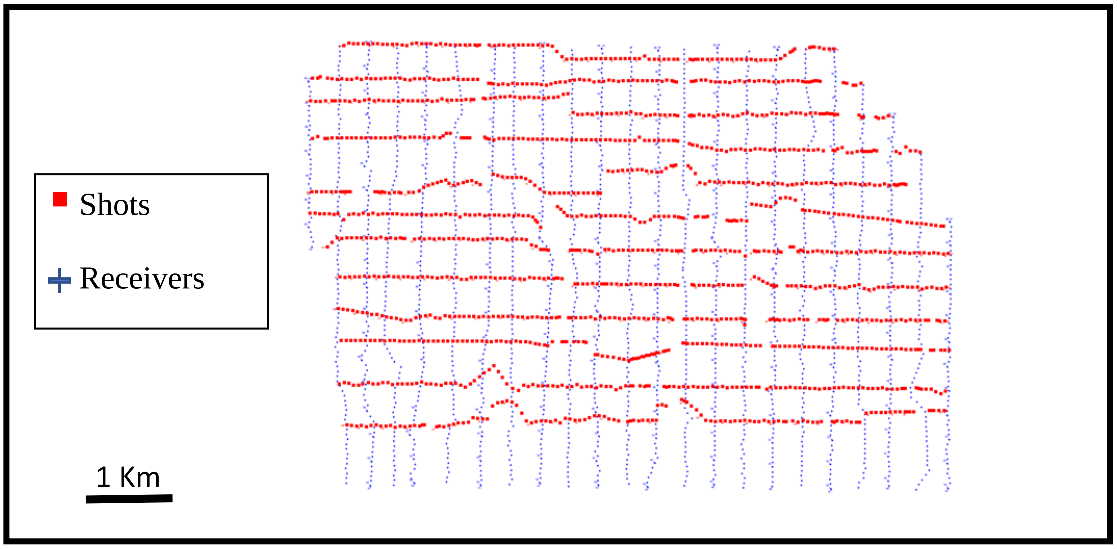

Figure 1.2: Shot and receiver lines for the selected area of the data

Following is a detailed list of software used in this thesis:

VISTA2D/3D®: Schlumberger seismic processing software, PROMAX SeisSpace 3D: Halliburton seismic processing software, SYNGRAM, PS Design and TomoPlus.

Chapter Two: **BACKGROUND**

2.1 Multicomponent Data

Since the 1990s, multicomponent seismic methods have been used in practice and for improving exploration in the oil and gas industry. That is due to the contribution of dedicated researchers at universities and oil companies, and the investigations are still going for the multicomponent methods including the type of the receivers and other acquisition instruments, processing techniques and data interpretation. It is now widely acknowledged by the industry that multicomponent seismic method has been a fruitful tool that utilizes the S-wave, beside the conventional P-wave, to understand the subsurface better (Xu, 2011).

If we are to define the multicomponent seismic data, it is the method that records the vibrational energy on three orthogonal components using unconventional instruments. On land, these instruments are usually geophones with three orthogonal motion detectors that is different from the conventional single motion (vertical) sensor geophone. These three-component geophones detect the vertical particle movement and two orthogonal horizontal particle movement caused by the travel of acoustic and elastic waves in the subsurface (Xu, 2011).

2.2 Advantages of Multicomponent Data

If we have P-S reflection data, what benefits can it offer? How to use it to improve the quality of our processing and interpretation methods? Multicomponent surveys have shown advantages over conventional surveys in seismic imaging, lithology identification, anisotropy analysis, fluid description examples and reservoir monitoring surveys (Stewart et al, 2003).

A very common case in imaging that demonstrates the advantage of P-S images over P-wave images is for gas chimneys and features below them. P wave data are very sensitive to gas saturation making high frequencies attenuate and their energy dissipate (Stewart et al, 2003). S-waves are less sensitive to rock saturants, and can penetrate through gas saturated sediments without losing energy to scattering (Stewart et al, 2003). This leads to a better imaged section of the structural reservoir located within or below gas chimneys.

The difference in resolution between the image of steeply dipping feature in the migrated P-wave section and the migrated P-S wave section is less clear, yet an improvement in imaging still could be noticed in the P-S section (Stewart et al, 2003). The reason behind that could be that structurally complicated areas have high velocity layers in the near surface causing both P and S energy to propagate at angles far from vertical (Stewart et al, 2003). This may cause both energies to be recorded on both vertical and radial channels, unless better separation methods are used.

Another example of P-S imaging benefits are in the near surface. Surveys have shown more highly resolved reflectors in the near surface on P-S sections than on P sections (Stewart et al, 2003). That could be caused by many factors such as: greater relative changes in S velocity than P velocity, the greater impact of density change on P-S reflectivity, and S-wave have lower velocities and have shorter wavelengths than P-waves with the same frequency (Stewart et al, 2003).

An important application of P-S data is for lithology identification (Stewart et al, 2003). P-wave data are good for imaging structures. But when it comes to identify the type of rocks and fluids in the section, P data are limited in these regards, but P-S data add an important parameter that allows us to do some analysis to help us identify lithologies, including V_p/V_s which is a good indicator of rock type (Stewart et al, 2003).

All these applications show how every piece of information is important to process the seismic data, provide a correct image in the subsurface and interpret it. What makes converted wave seismic very beneficial is that we can deal with it as a separate data, process them, draw attributes from them and interpret them. Then we can do many comparisons and correlations with P-wave data. See where they agree and where they differ. Also, every one of those experiments help us understand the subsurface in terms of composition, structure and processes and help us provide better images and draw more information from the subsurface.

2.3 Processing of Multicomponent Data

In this thesis, the processing of the P-wave data followed the conventional processing flow. However, for processing the converted P-S data additional steps are required such as data rotation, near surface correction and velocity analysis.

2.3.1 Rotating horizontal components

3C 3D seismic surveys record reflections of the vertical component and two orthogonal horizontal components namely H1 and H2 as seen in Figure 2.1. These components are referenced to the source-receiver plane. Due to the source and receiver geometry in the 3D survey, geophones record data from different source-receiver azimuths. Therefore, a rotation of the data to the source-receiver plane and the orthogonal plane must be made to acquire the radial and the transverse components, respectively.

In order to obtain the radial and transverse components, the angle Θ between the H1 component azimuth and the source-receiver azimuth must be known. That could be accomplished manually through the hodogram analysis or automatically by sorting the data into receiver and selecting some offsets where there is a good first break. Then the radial and transverse components are obtained from equations 2.1 and 2.2:

$$R = H1cos\Theta\ + \mathrm{H2sin}\Theta \tag{2.1}$$

$$T = H1sin\Theta - \mathrm{H2cos}\Theta \tag{2.2}$$

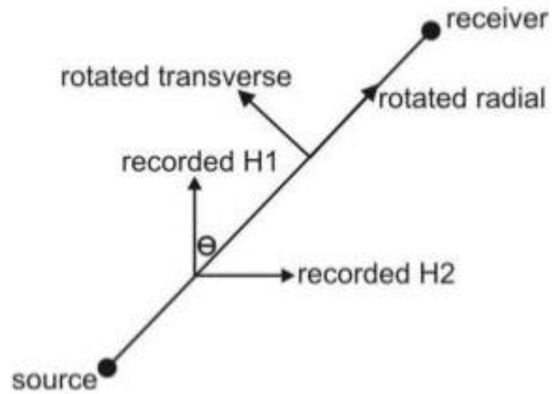

Figure 2.1: Rotation of H1 and H2 components into radial and transverse components

2.3.2 Binning

For P-wave data, the binning process is completed using conventional midpoint binning to create the CMP grid for the survey. However, for P-S wave the conversion of P-waves to S-waves results in the travel path being asymmetric for flat reflectors, as shown in Figure 2.2, which rules out the standard common midpoint binning used for P-waves data. The raypaths of the converted waves are asymmetric and the reflection points in the subsurface are always closer to the receiver than the midpoint. Different techniques are required to stack such data where common conversion point (CCP) is considered instead of common mid-point (CMP) in the conventional surveys (Lawton, 1993). The Common Conversion Point (CCP) techniques could be asymptotic (Behle and Dohr, 1985; Fromm et al., 1985), Single Depth (Tessmer and Behle, 1988; Tessmer et al., 1990), on depth-variant CCP mapping (Eaton et al., 1990; Stewart, 1991), and converted-wave DMO (Harrison, 1992). In this paper we will only consider both the asymptotic and depth-variant binning methods.

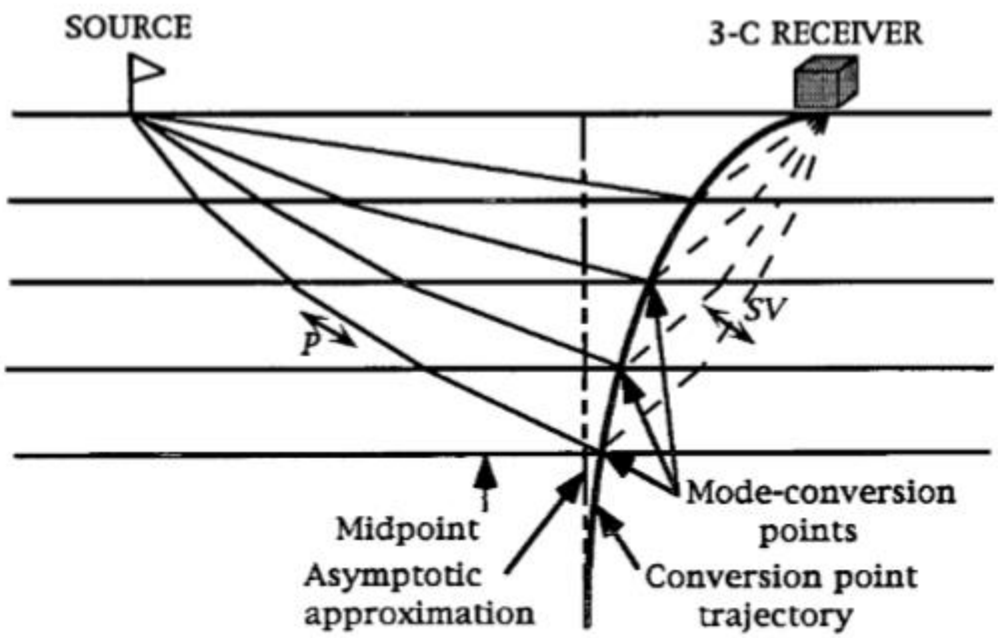

Figure 2.2: P-S raypaths, conversion points and asymptotic approximation (Schafer, 1992)

2.3.3 Near surface correction

It is known for P-wave data processing that the near surface causes a delay in time, which could be dealt with by the different static correction methods (Saul, 2017). Moreover, S-waves are slower than P-waves, and fluids do not have any effect on S-wave propagation. For these reasons, the effect of near surface layer on converted wave data is more serious and correcting it is more critical.

The tomography static approach for the vertical component was developed using the following workflow: picking first breaks, examining traveltimes and removing bad picks, building 1D velocity model following 3D surface topography, imaging 3D near surface using refraction tomography to output a velocity layer model, viewing the velocity model and picking intermediate and floating datums, calculating long- and short-wavelength statics, exporting ASCII static file, updating trace headers with new static values and finally applying static corrections.

For the P-S data, we used the same source static values calculated from the vertical component. However, the receiver static correction is very different and the converted reflection raypath differs from the vertical one due to the change of the location of the conversion point in the subsurface. To calculate the receiver static correction for the radial component, we first create receiver stacks after NMO correction. The static effects on P-S data could be large due to the complex and variable shear wave velocities (Gunning, 2014). Then, the receiver static correction followed a four-step workflow: pick horizons on the receiver stack, smooth horizons, subtract original horizons from smoothed ones, apply the difference as receiver static values (Gunning, 2014).

2.3.4 Noise attenuation

A radial trace filter was applied to the data because it works efficiently on coherent noise in 3D data without the need for data regularization (Henley, 2007). Figure 2.3 shows the coherent noise generated in a typical 3D survey, and how the noise wavefronts would look if they were recorded on receiver lines from a far offset shot. Only the receiver line that indicates the shot location will have traces uniformly distributed while other receiver lines will show traces distributed hyperbolically (Henley, 2007).

The method used to organize the traces to detect the coherent noise in this workflow is to order the traces by increasing absolute source-receiver offset. Figure 2.4 shows a possible way to do that within a narrow angular segment. In practice, the offset trace header must be modified into increasing source-receiver offset. That means a normal split shot gather with negative offsets in one side and positive ones on the other, instead of the normal offset where it decreases until it reaches the receiver line closest to the shot then starts to increase again, as shown in Figure 2.5 (Henley, 2007).

(a)

(b)

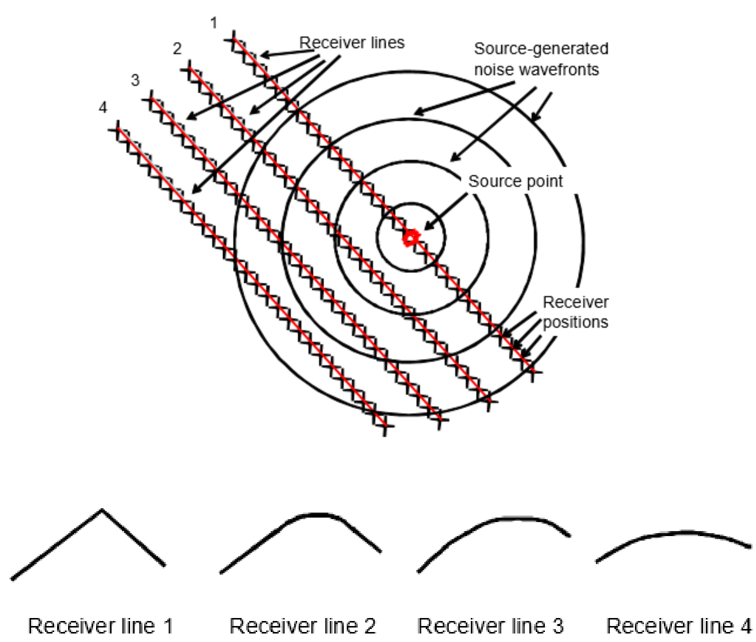

Figure 2.3: (a) Coherent noise wavefronts and their relationship to the 3D seismic geometry. (b) Wavefront arrival times as a function of receiver lines (from Henley, 2007).

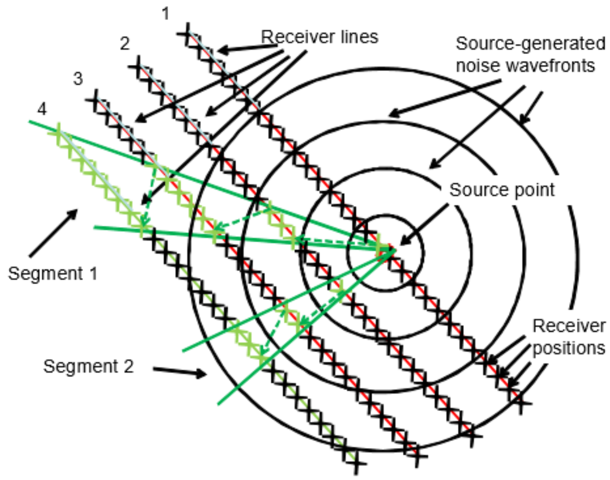

Figure 2.4: Schematic showing a possible way to gather traces for coherent noise attenuation—sorted by ascending offset within a narrow angular segment (Henley, 2007).

Noise must be removed before the deconvolution step in order to not let noise interfere with the process of compressing the wavelet in time. The noise attenuation workflow used for this step is: surface wave attenuation, coherent noise attenuation and finally bandpass filter.

Surface wave attenuation performs a frequency dependent mix of adjacent traces. It could be applied on shot domain or receiver domain because this method operates on the frequency-space domain. The number of traces to mix at each frequency is calculated by equation 2.3 (ProMax, 1997):

$$Mix = v \times \frac{f}{\Delta t} \tag{2.3}$$

Where v is the velocity, f is frequency and Δt is the trace spacing. Frequency components higher than the cut-off frequency remain unchanged. Lastly, data are transformed back to the time-space domain.

(a)

(b)

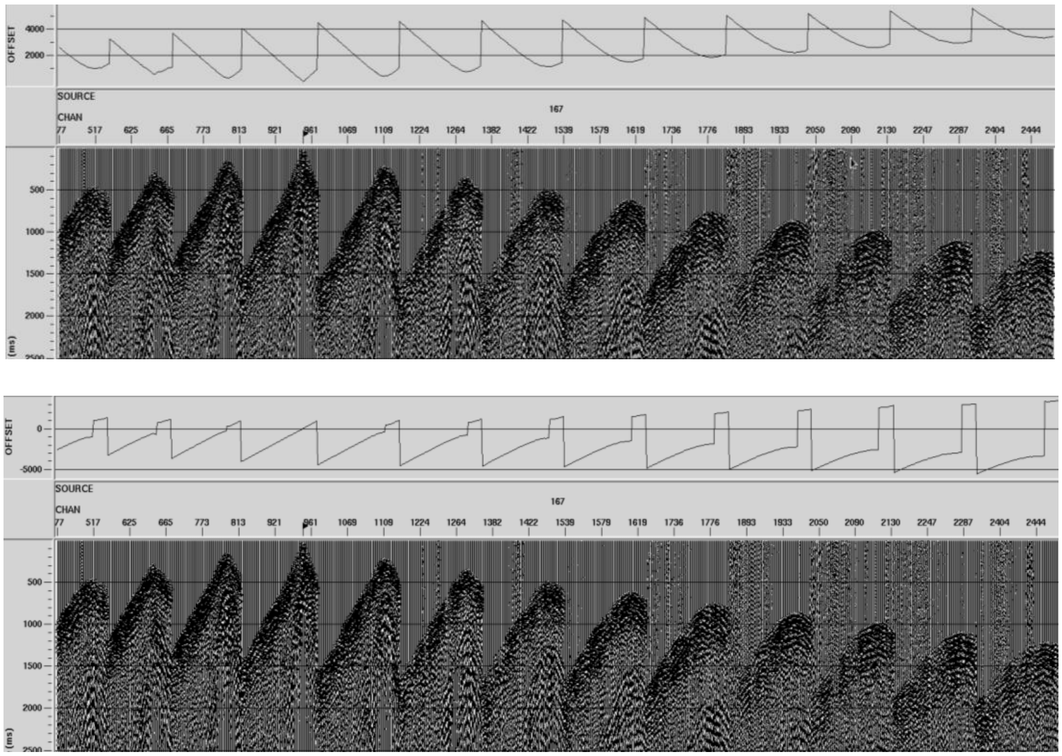

Figure 2.5: (a) Raw shot gather before and (b) after modifying offset trace headers

Coherent noise attenuation also operates on the frequency-space domain. The noise should be characterized by a band of energy in the f-k domain, by pairs of velocity and frequency. This process targets source noise generated and linear noise.

Finally, bandpass filter was applied to remove the low frequency noise.

2.3.5 Deconvolution

Deconvolution is the process to increase the temporal resolution by removing the seismic wavelet from the seismic trace (Yilmaz, 2001). As a result, multiples are attenuated and the amplitude spectrum is better balanced (Isaac, 1996). There are several deconvolution methods (spiking, predictive, etc.) which assume that the wavelet is invariant in time where the effects of attenuation and frequency and amplitude variation are not considered (Margrave and Lamoureux, 2002). Deconvolution used in this processing workflow is minimum phase predictive deconvolution that compresses the basic wavelet and attenuates short-period multiples. To yield optimum results, a geometric spreading compensation is applied to recover the amplitude loss due to spherical divergence. Moreover, exponential gain is applied to compensate for spherical divergence and transmission losses (Yilmaz, 2001).

2.3.6 Velocity analysis

Stacking velocities are interpreted following the procedure of comparing a series of stacked traces in which a range of velocities were applied to correct for normal moveout (NMO). The typical practice involves picking a velocity in a panel as a function of time to properly correct pre-stack data. The correction removes the time delay caused by the separation of the source and receiver on the surface.

2.3.7 Residual statics

Residual static corrections are necessary to remove the residual near-surface traveltime delays caused by the result of varying velocity or/and varying of the depth of the weathering layer. Source and receiver residual statics are computed using the Maximum Power Autostatics. 3D Maximum Power Autostatics method builds an initial pilot trace model from different time gates of surrounding traces for each CDP. These pilot traces are formed by flattening all traces along the autostatic horizon over the number of CDPs indicated in the autostatic horizon. Then, all these traces are summed to form a pilot trace. After that, trace from a specific CDP is subtracted from the pilot trace and that forms a new pilot trace which leads to forming a shift-power trace. We sum again but this time the shift-power trace and similar other ones having the same receiver and again with those having the same source. This process is repeated for all traces in the active CDP. (Joshua and Claerbout,1985)

2.3.8 Post stack time migration

The migration process used in this project is a post-stack time migration using explicit finite-difference that images dips up to 70 degrees dip, which is more than enough for this data. Pre-stack time migration was not used due to limited processing resources. In addition, there are no complex subsurface structures in the chosen area for this thesis.

This process goes through the following steps: Fourier transform data to frequency and transpose to horizon slices, generate gridded velocity from an interval velocity versus time functions and finally migrate extrapolation of frequency slices.

Chapter Three: EVALUATION OF 3C 3D SURVEY DESIGN OF P-P AND P-S BINNING

3.1 Introduction

A synthetic seismogram is usually used to correlate seismic and well data and it is generated by using sonic and density logs to derive acoustic impedance sections. From these data, we can compute reflection coefficients at each interface between contrasting velocities.

From equation 3.1, we know the other parameter needed is the wavelet:

$$S(t) = w(t) * r(t) \tag{3.1}$$

Where S is synthetic seismogram, $*$ is convolution, w is the wavelet and r is the reflectivity time series. The wavelet is the link between synthetic traces and the geology (reflection coefficients) that is being interpreted. In this case, we have V_p, V_s and density logs with tops picked on them indicating our area of interest. Our target is Duvernay Formation which is around 3400 m deep. We create an offset synthetic seismogram that gives a strong interpretable response at that depth level considering the following parameters and phenomena: wavelet, maximum useable offset, NMO stretch and distortions, amplitude/phase issues as approaching critical angle and maximum offset to depth ratio. In this chapter, we will determine the maximum usable offset for the 3C 3D dataset. Then we will implement that, with the optimum bin size, to evaluate survey design for both P-P and P-S data.

3.2 Synthetic data

To generate synthetic seismograms, CREWES SYNGRAM software was used. SYNGRAM creates primaries only synthetic seismograms for P-P and P-S reflections (Thurston, 1990). The synthetic seismograms are trace gathers for a horizontally layered earth and show the variation of amplitude with offset as well as the stacked response. The reflection amplitudes, and optional transmission losses, are calculated from the Zoeppritz equations (no approximation) and are therefore appropriate for plane-wave incidence (Richards and Aki, 1980). Traveltimes and incidence angles are calculated by ray tracing.

SYNGRAM requires the input of P-wave sonic (and S-wave sonic if available) and bulk density in addition to the wavelet. Some of the logs provided to SYNGRAM are shown in Figure 3.1. The layered earth model is provided to SYNGRAM in a consistent set of units. If an S-wave log is not available, then in order to create S-wave sonic log, the software assumes V_p/V_s to be a user-defined value (typically 2). However, the V_p/V_s ratio used here is 2.01 according to previous work by (Weir, 2018) in the general area of interest, and are summarized in table 3.1.

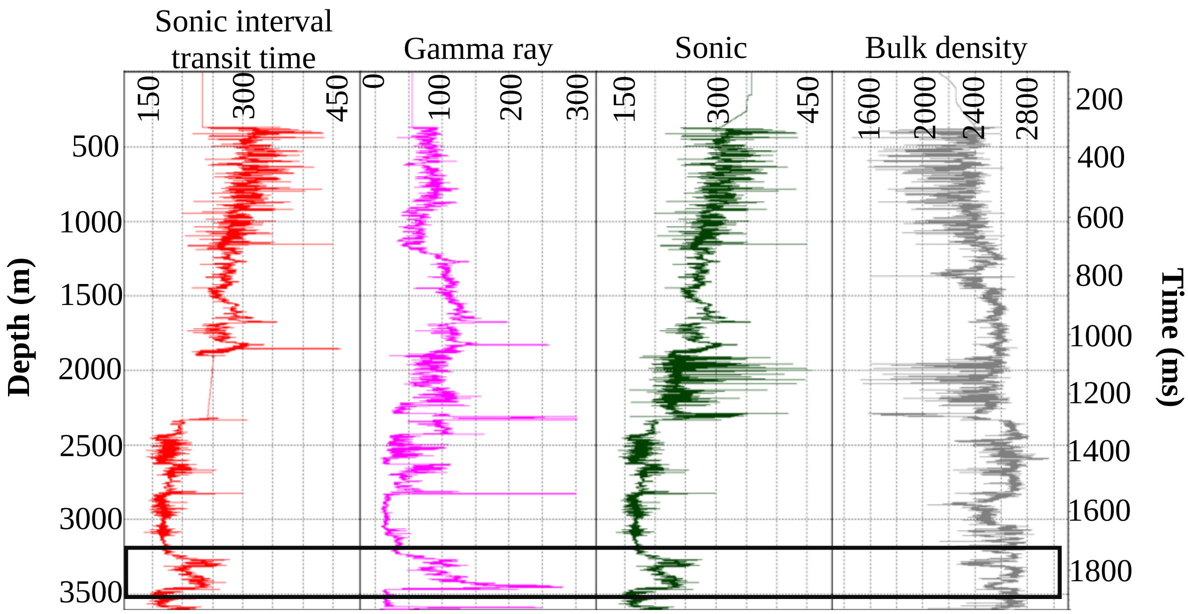

Figure 3.1: Well logs from left to right: sonic interval transit time, gamma ray, delta transit time and bulk density. The annotated part is the area of interest.

Table 3.1: Interval and surface-to-depth Vp/Vs ratios. The row in blue are the measured P-S times, the column in green are the measured P-P times. Vp/Vs at the depth of interest SWH is 2.01 (Weir et al., 2018)

V_P/V_S	2WS	Doe Creek	Wab.	Ireton	Swan Hills	Gill	~Prec	PP time (ms)
Colo	**2.15**	1.99	2.15	2.09	2.05	2.07	2.18	971
2WS	1.991	**2.09**	1.88	1.86	1.981	2.02	2.156	1253
Wab.	2.148	1.88	**2.03**	1.80	1.78	1.94	2.06	1766
Ireton	2.088	1.88	1.80	**2.03**	1.814	2.09	2.06	1933
SWH	2.050	1.981	1.87	1.814	**2.01**	2.411	2.18	2000
Gill.	2.073	2.017	1.93	2.09	2.411	**2.02**	2.02	2068
~Prec.	2.179	2.02	2.06	2.06	2.18	2.02	**2.02**	2151
PS time (ms)	1484	1950	2674	2909	2994	3110	3298	V_P/V_S

For the wavelet, SYNGRAM allows the user to create different types of wavelets. The wavelets used here are bandpass wavelets for P-P and P-S data with parameters shown in Figure

3.2. Both wavelets were designed based on the analysis of P-P and P-S from the field survey. The wavelets designed are shown in Figure 3.3.

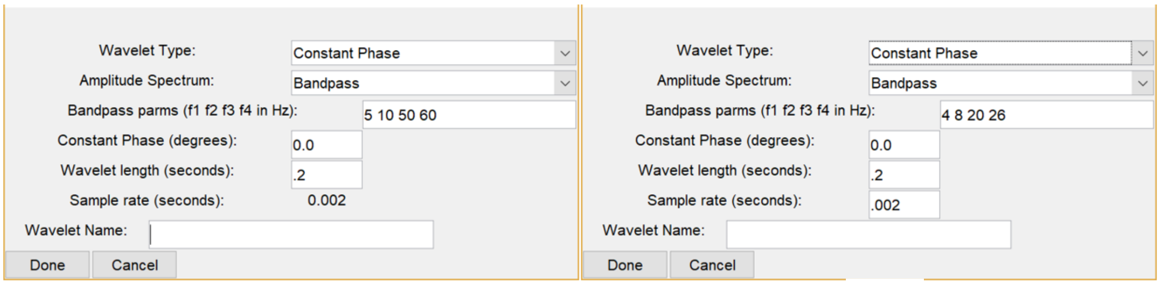

(a) (b)

Figure 3.2: (a) Parameters for P-P and (b) for P-S wavelets in SYNGRAM

Using both log data and constructing the appropriate wavelets, SYNGRAM convolves the time reflectivity series generated from the well logs with the wavelets to generate synthetic offset gathers and stacks for both P-P and P-S. The maximum available offset from the real data survey is approximately 6200 m. To include all of these offsets, the maximum offset-depth ratio is set to be 2 for SYNGRAM analysis. Initial P-P and P-S seismograms generated are shown in Figure 3.4. The interval of interest is between depths of 3350 to 3450 m, which is between Devonian Woodbend and Duvernay formations.

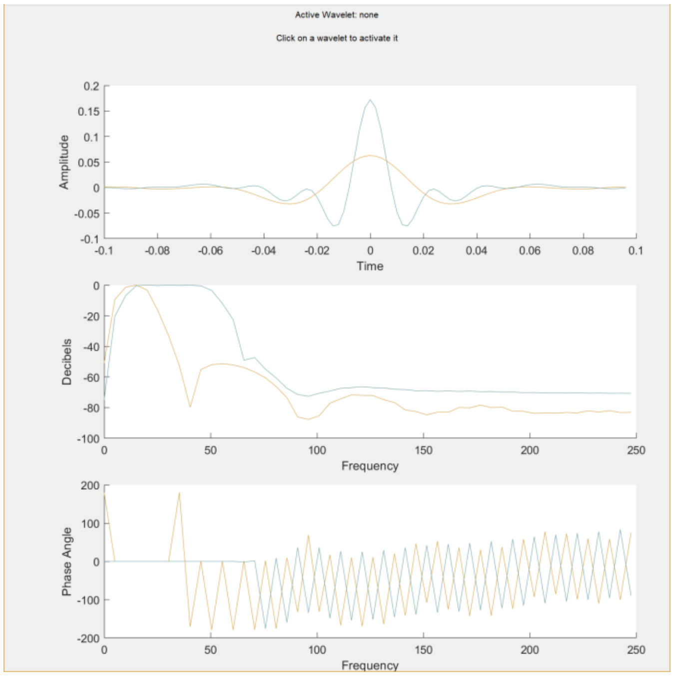

Figure 3.3: Constructing wavelets in SYNGRAM. Characteristics of P-P (green) and P-S (yellow) overlapped

3.3 Synthetic dataset analysis

Changing the maximum offset-depth ratio allows us to mute distorted traces at far offsets. So, the offset-depth ratio works as a mute function excluding uninterpretable traces. Ratios used in Figure 3.5 are 1.3 and 1.5 for P-P and P-S, respectively.

Analyzing both synthetic seismograms, stretch is observed in some traces at certain large offsets and depths. That will help us decide on the maximum useable offsets when we design our P-P and P-S surveys. Our target is at 3400 – 3430 m deep. Traces at that depth are distorted around 4500 m and 5500 m offsets so we muted beyond that offset at that depth, as shown in Figure 3.5 and Figure 3.6 which show the stack response of these gathers.

(a)

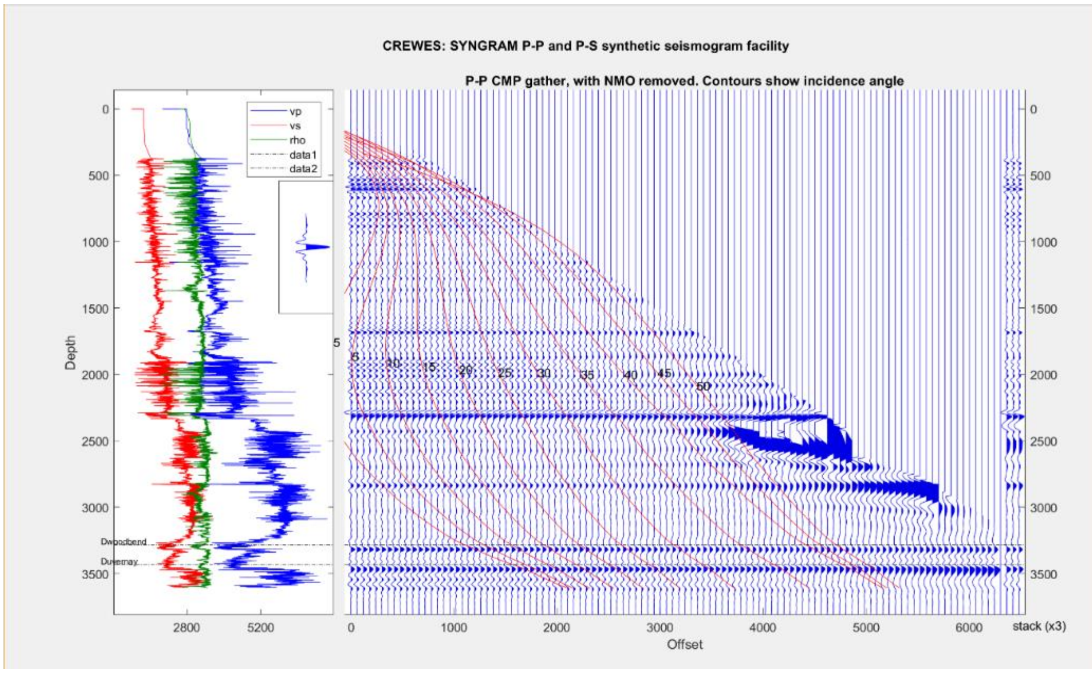

(b)

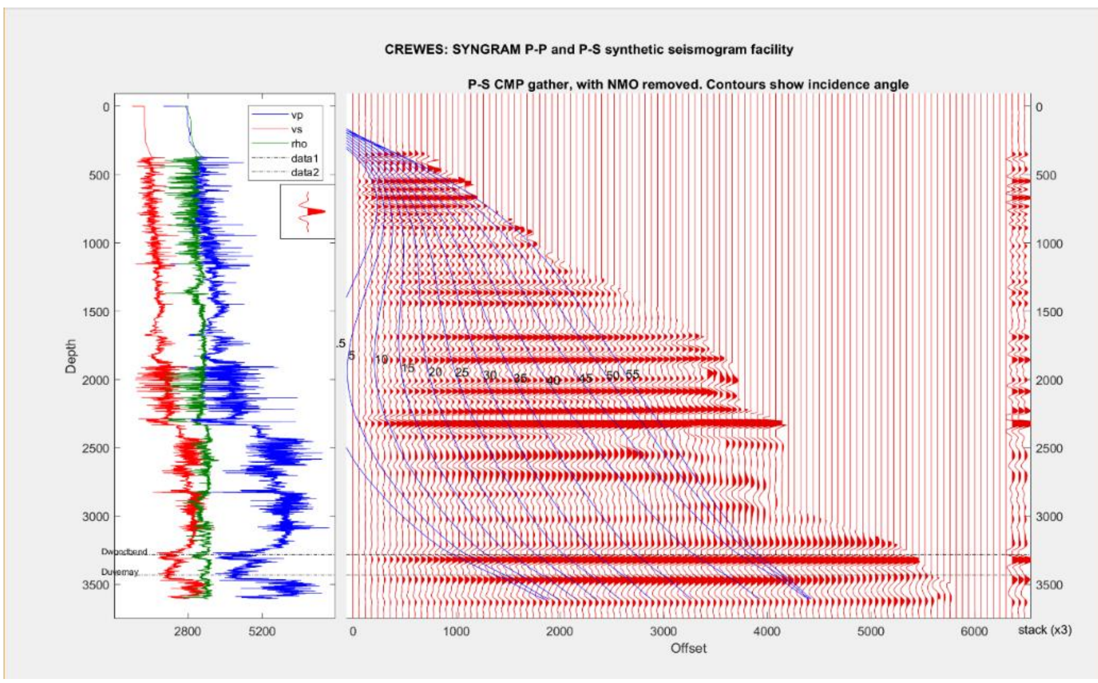

Figure 3.4: Generating Synthetic shot gathers in SYNGRAM. (a) Synthetic offset gathers for P-P and (b) for P-S. Vs log was generated based on the ratio $V_p/V_s = 2.01$ and offset/depth was chosen to be 2 (amplitudes were scaled in both seismograms)

(a)

(b)

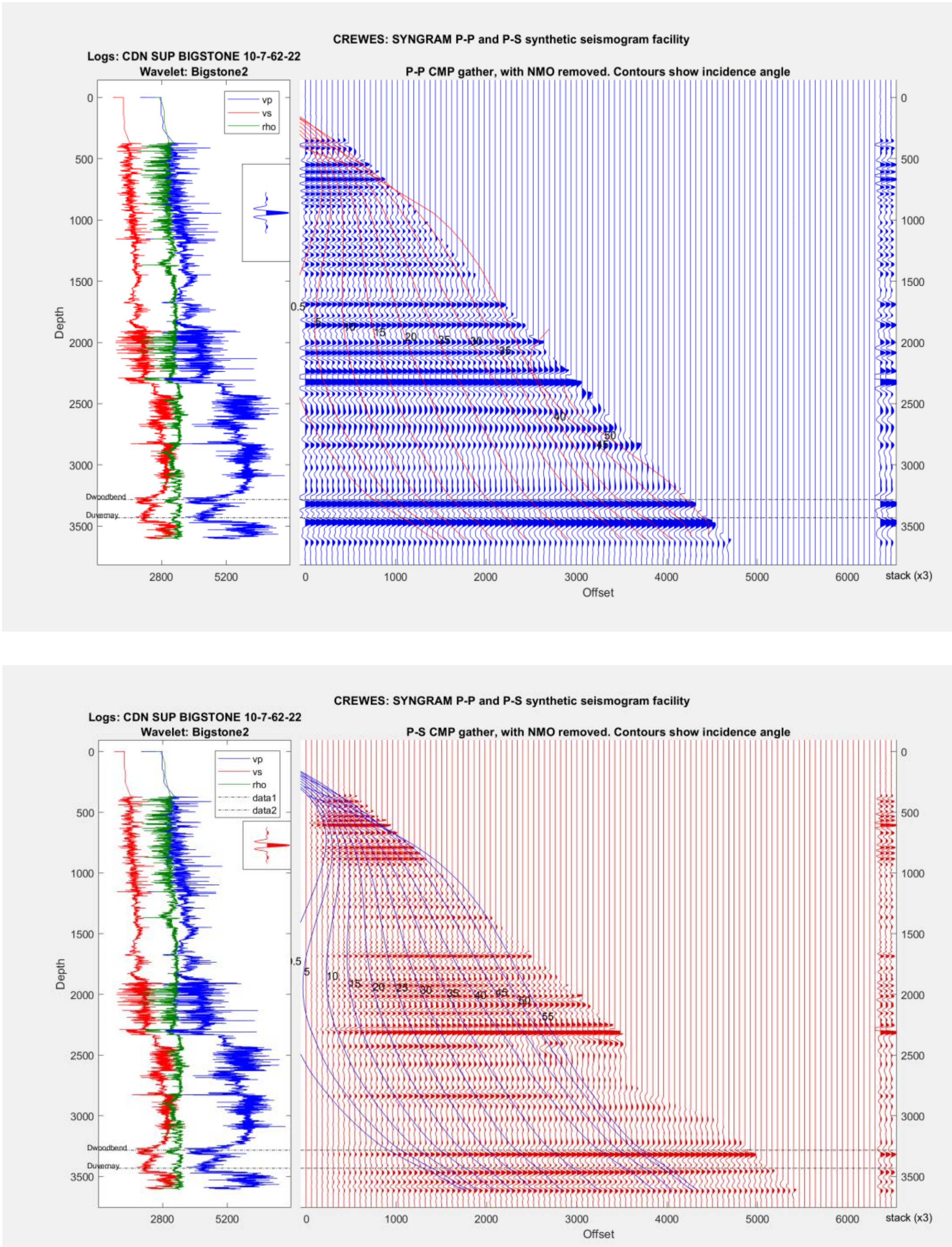

Figure 3.5: (a) P-P synthetic offset gathers after muting distorted traces and (b) P-S synthetic offset gathers after muting distorted traces. Maximum useable offsets for P-P and P-S are 4500 ms and 5500 m, respectively.

(a) (b)

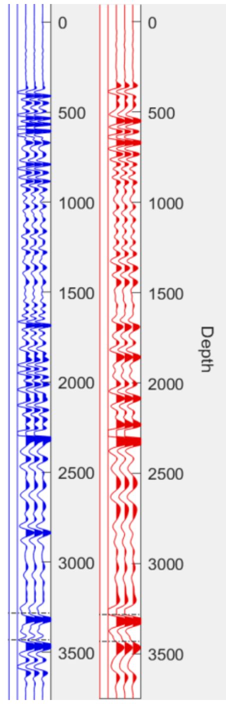

Figure 3.6: Stack response for both (a) P-P and (b) P-S synthetic data generated in SYNGRAM

3.4 PS Design analysis

PS Design software allows conventional CMP binning for P-P data and two types of P-S survey design; asymptotic and depth specific. In this part, we will compare and evaluate the fold and azimuth for P-P, P-S asymptotic and depth specific, with and without an optimum bin size.

3.4.1 P-P design

The source-receiver geometry in Figure 3.7a is designed to approximate the same acquisition parameters of the real data, as shown in Figure 3.7b. After designing the geometry as shown in Figure 3.8, calculating the bin size from the acquisition parameters (30 x 30 m) and estimating the maximum useable offset from the synthetic seismograms, we evaluate the fold, offset range, offset distribution and azimuth distribution maps, shown in Figure 3.9.

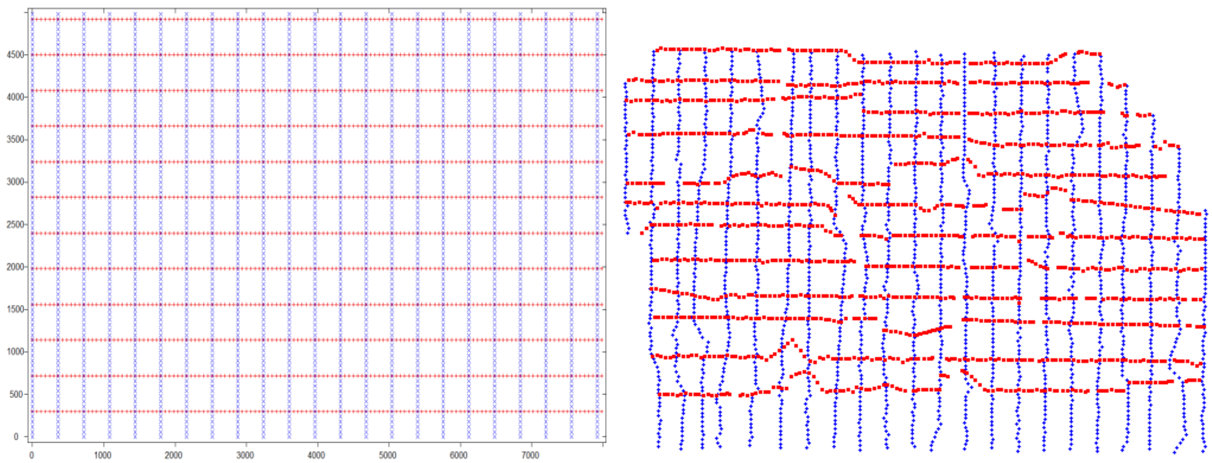

(a) (b)

Figure 3.7: (a) Source receiver geometry in PS Design and (b) the shot receiver geometry for the real data

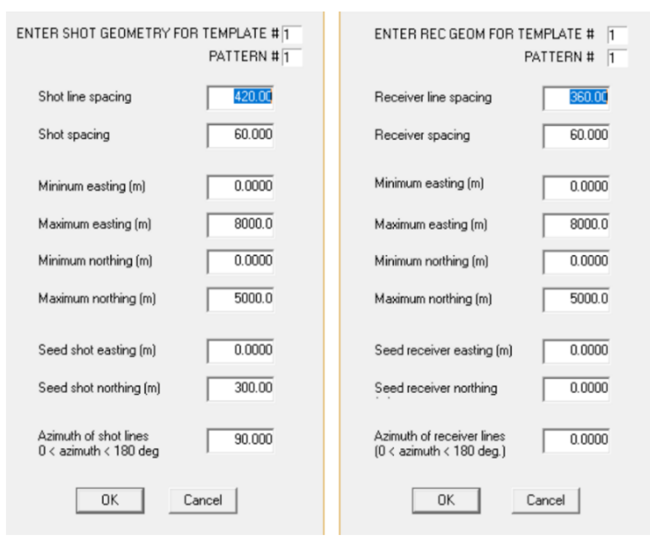

(a) (b)

Figure 3.8: (a) Shot and (b) receiver parameters used to design the geometry

(a)

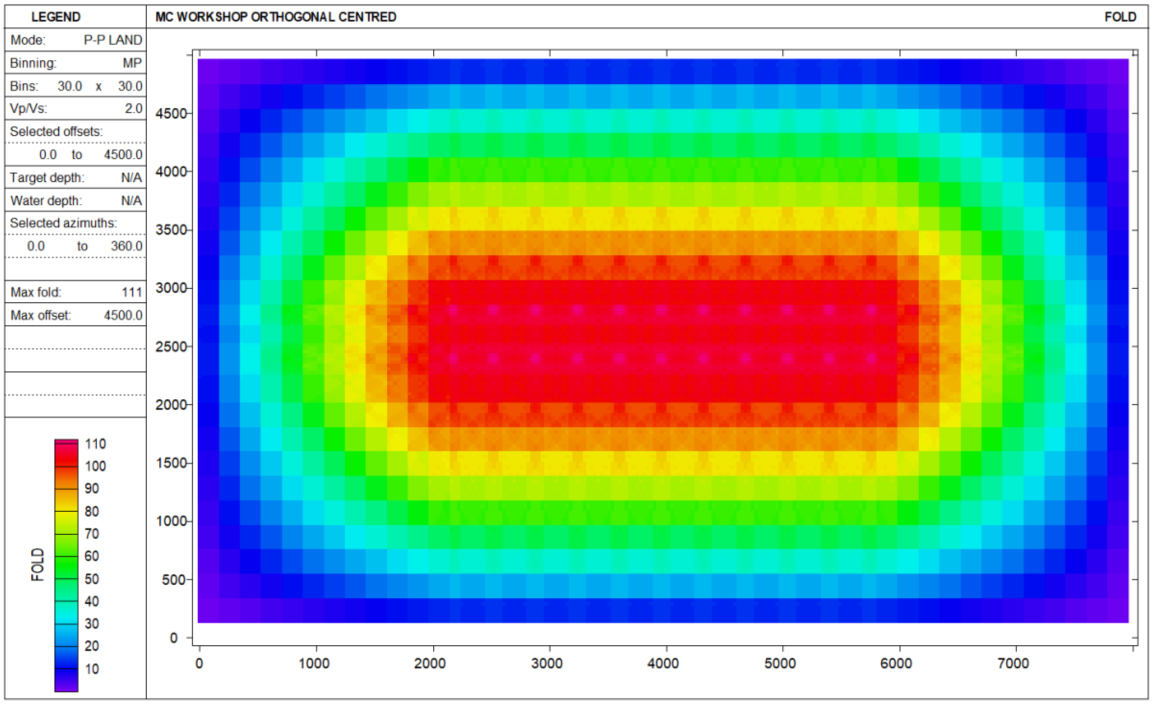
LEGEND
MC WORKSHOP ORTHOGONAL CENTRED
FOLD
Mode: P-P LAND
Binning: MP
Bins: 30.0 x 30.0
Vp/Vs: 2.0
Selected offsets:
0.0 to 4500.0
Target depth: N/A
Water depth: N/A
Selected azimuths:
0.0 to 360.0
Max fold: 111
Max offset: 4500.0
FOLD
110
100
90
80
70
60
50
40
30
20
10
4500
4000
3500
3000
2500
2000
1500
1000
500
0
0
1000
2000
3000
4000
5000
6000
7000

(b)

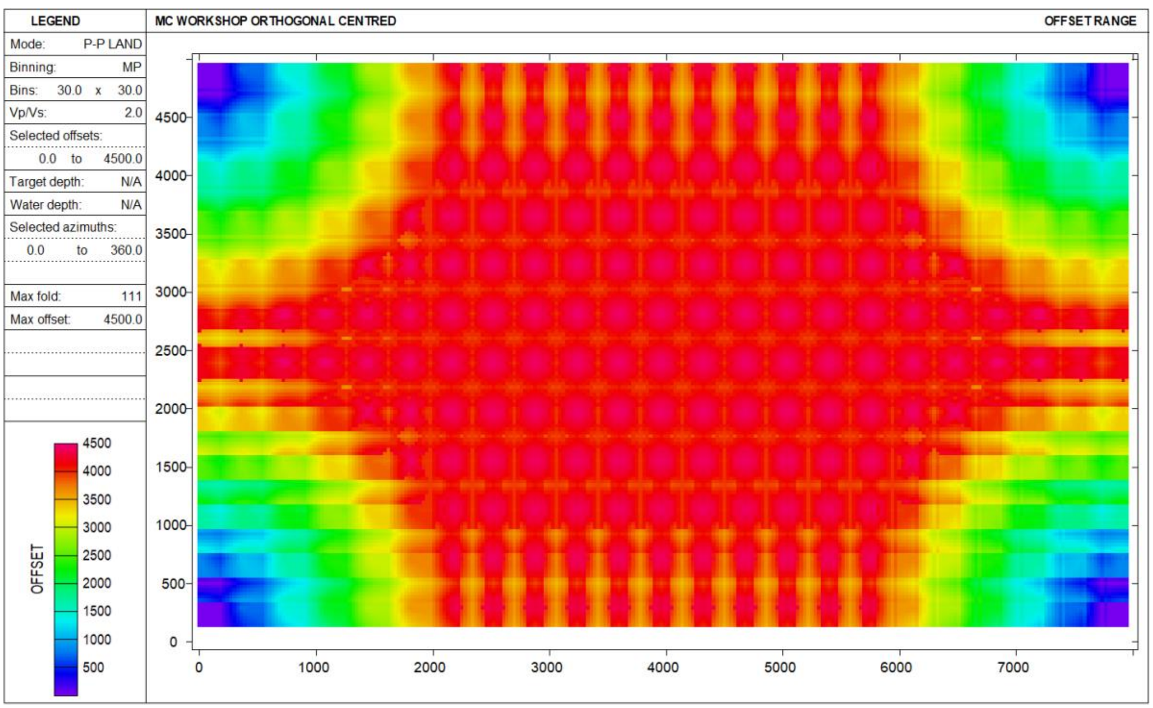
LEGEND
MC WORKSHOP ORTHOGONAL CENTRED
OFFSET RANGE
Mode: P-P LAND
Binning: MP
Bins: 30.0 x 30.0
Vp/Vs: 2.0
Selected offsets:
0.0 to 4500.0
Target depth: N/A
Water depth: N/A
Selected azimuths:
0.0 to 360.0
Max fold: 111
Max offset: 4500.0
OFFSET
4500
4000
3500
3000
2500
2000
1500
1000
500
4500
4000
3500
3000
2500
2000
1500
1000
500
0
0
1000
2000
3000
4000
5000
6000
7000

(c)

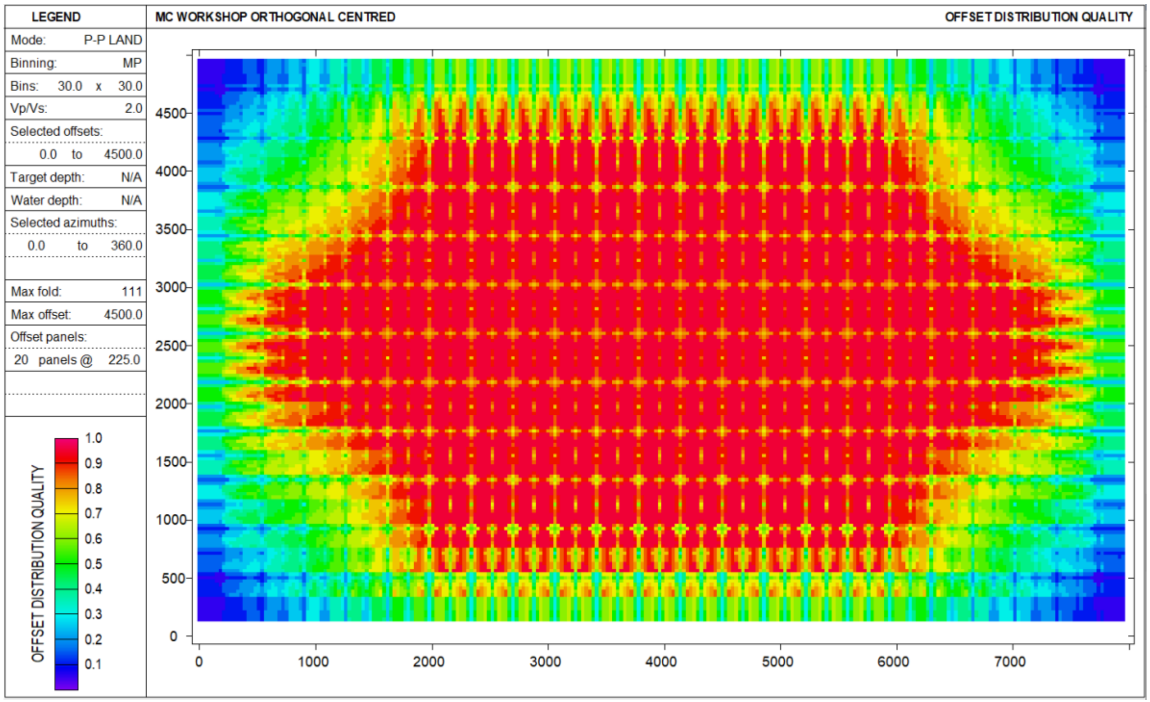

(d)

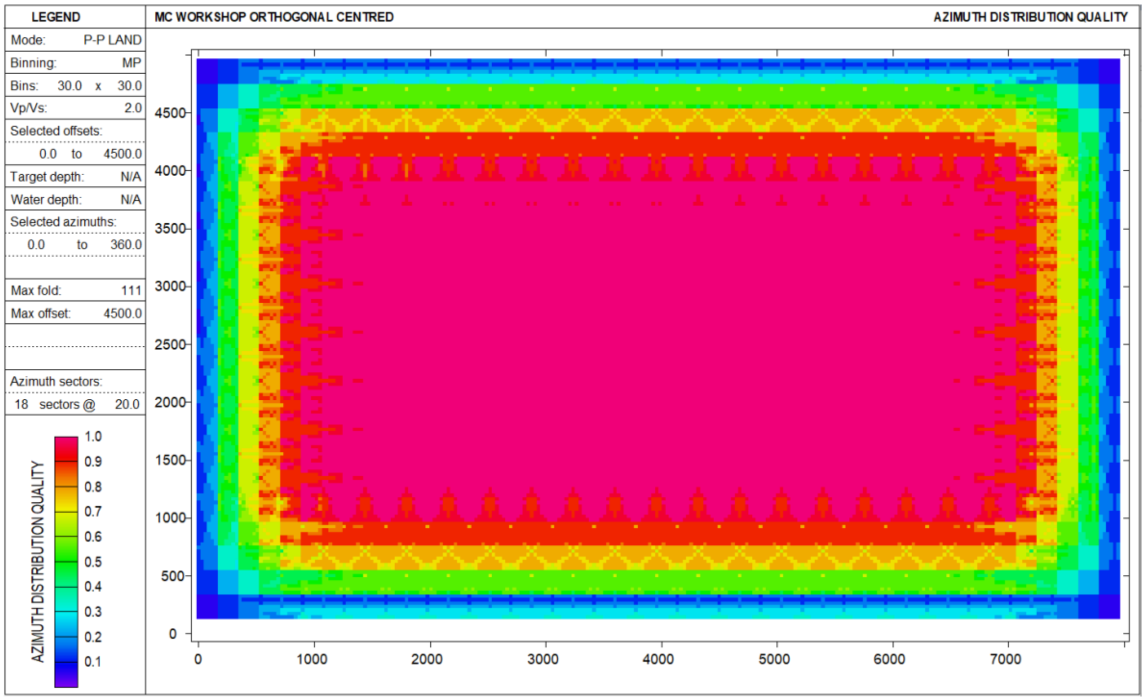

Figure 3.9: P-P maps: (a) fold, (b) offset range, (c) offset distribution and (d) azimuth distribution

The maps in Figure 3.9, show a good distribution of attributes for the high-fold parts of the whole survey. That is expected as the survey is orthogonal, and the grid is binned based on CMP conventional gridding. Further analysis is done by zooming to the middle of the survey, as in Figure 3.10, and evaluating the azimuth vs fold and offset vs fold for a single bin as an example.

(a)

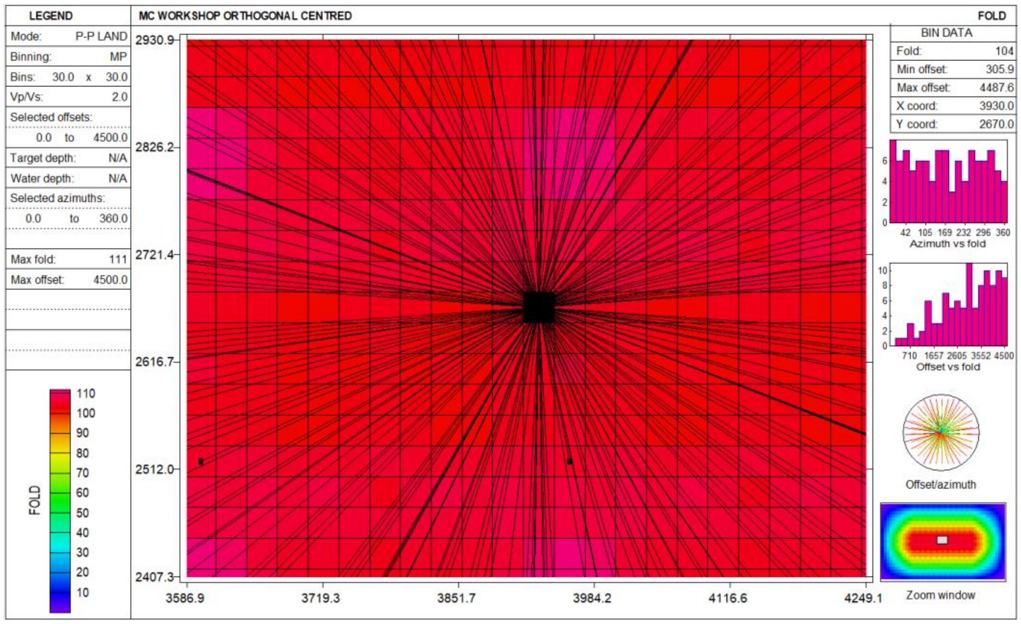

(b)

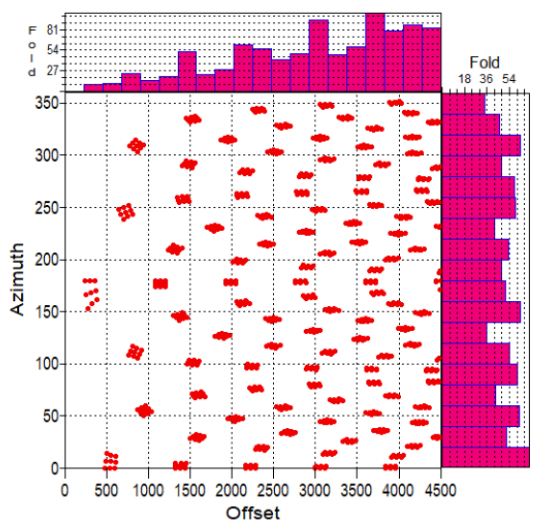

Figure 3.10: (a) Azimuth vs fold is quite consistent for a single bin in the middle of the survey. More traces from far offsets are contributing to a bin in the middle of the survey. (b) A uniform distribution between azimuth and offset

3.4.2 P-S design (Asymptotic)

P-S Design offers two types of survey design for P-S data. The first one is the P-S asymptotic and the second one is P-S depth specific. In this part, we will do the same steps as in P-P design but for P-S asymptotic survey, using the same binning. However, we changed the offset parameters this time to 5500 m based on the analysis completed in SYNGRAM. In addition, $V_p/V_s = 2.0$ is provided to the software to calculate the conversion point (V_p/V_s at the depth of interest is 2.01, but P-S Design accepts only one significant figure). It calculates conversion points according to equation 3.2:

$$Xp = \frac{X}{1 + Vs/Vp} \tag{3.2}$$

Where Xp is the offset from the source to the conversion point, X is the total source-to-receiver offset, and Vs/Vp is the shear-to-compressional wave velocity ratio in the area. This method is not depth variant. Therefore, it requires only a simple calculation for each shot-receiver for the conversion point to be placed in the asymptotic location in the subsurface.

In the next step, I am going to show the effect of the asymptotic binning for P-S wave and how re-binning with ACP helps to solve the problems arise with that.

Observing the attributes for this P-S design as we did in the previous one, we notice an increase in the fold shown in Figure 3.11a. However, irregularities are clearly shown in the middle of the survey (the area of nominal fold) and they are observed for all attributes.

(a)

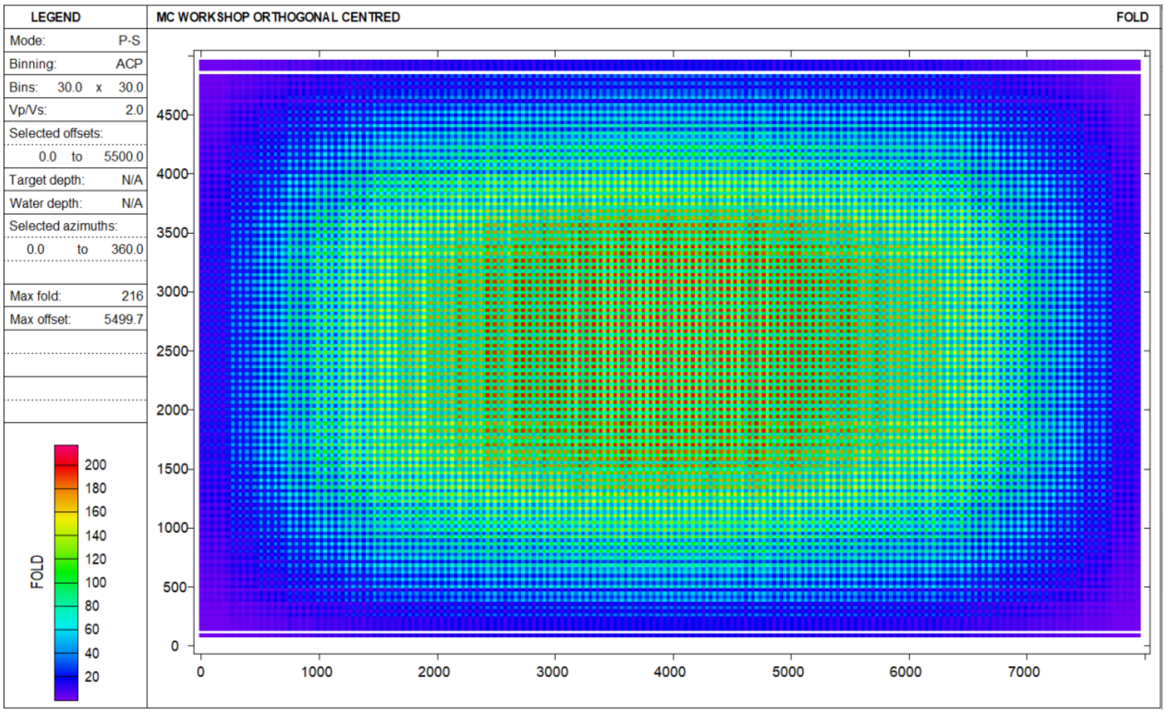

LEGEND
MC WORKSHOP ORTHOGONAL CENTRED
FOLD
Mode: P-S
Binning: ACP
Bins: 30.0 x 30.0
Vp/Vs: 2.0
Selected offsets:
0.0 to 5500.0
Target depth: N/A
Water depth: N/A
Selected azimuths:
0.0 to 360.0
Max fold: 216
Max offset: 5499.7
FOLD
200
180
160
140
120
100
80
60
40
20
4500
4000
3500
3000
2500
2000
1500
1000
500
0
1000
2000
3000
4000
5000
6000
7000

(b)

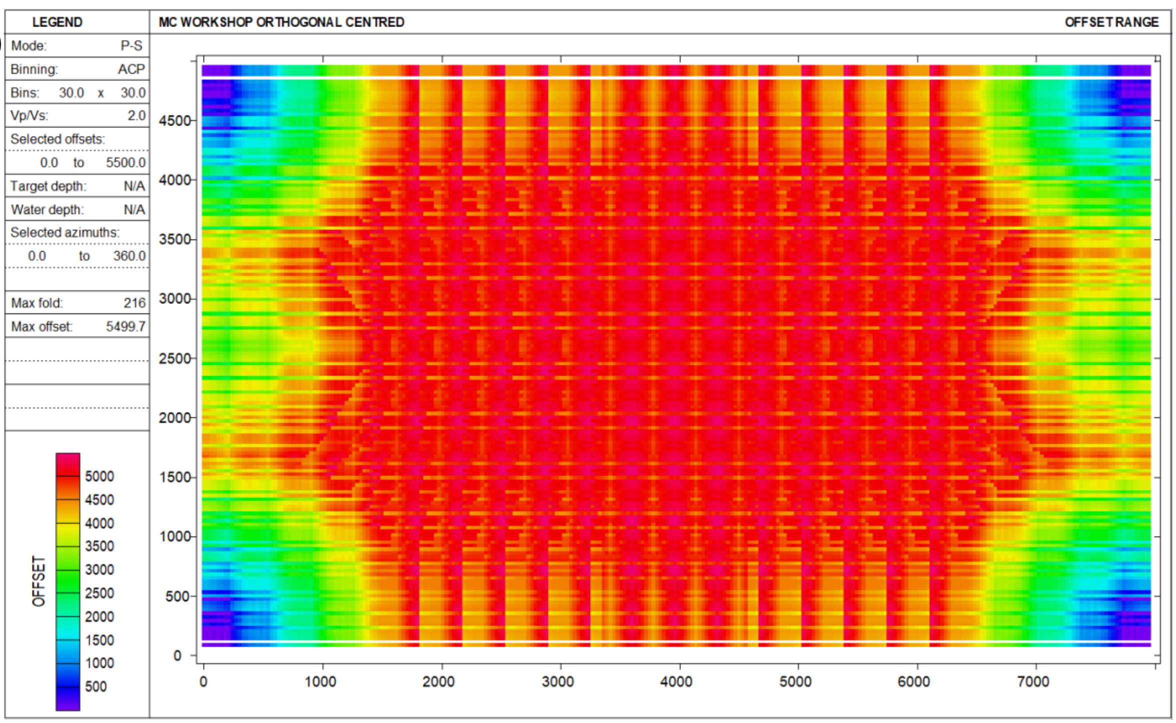

LEGEND
MC WORKSHOP ORTHOGONAL CENTRED
OFFSET RANGE
Mode: P-S
Binning: ACP
Bins: 30.0 x 30.0
Vp/Vs: 2.0
Selected offsets:
0.0 to 5500.0
Target depth: N/A
Water depth: N/A
Selected azimuths:
0.0 to 360.0
Max fold: 216
Max offset: 5499.7
OFFSET
5000
4500
4000
3500
3000
2500
2000
1500
1000
500
4500
4000
3500
3000
2500
2000
1500
1000
500
0
1000
2000
3000
4000
5000
6000
7000

(c)

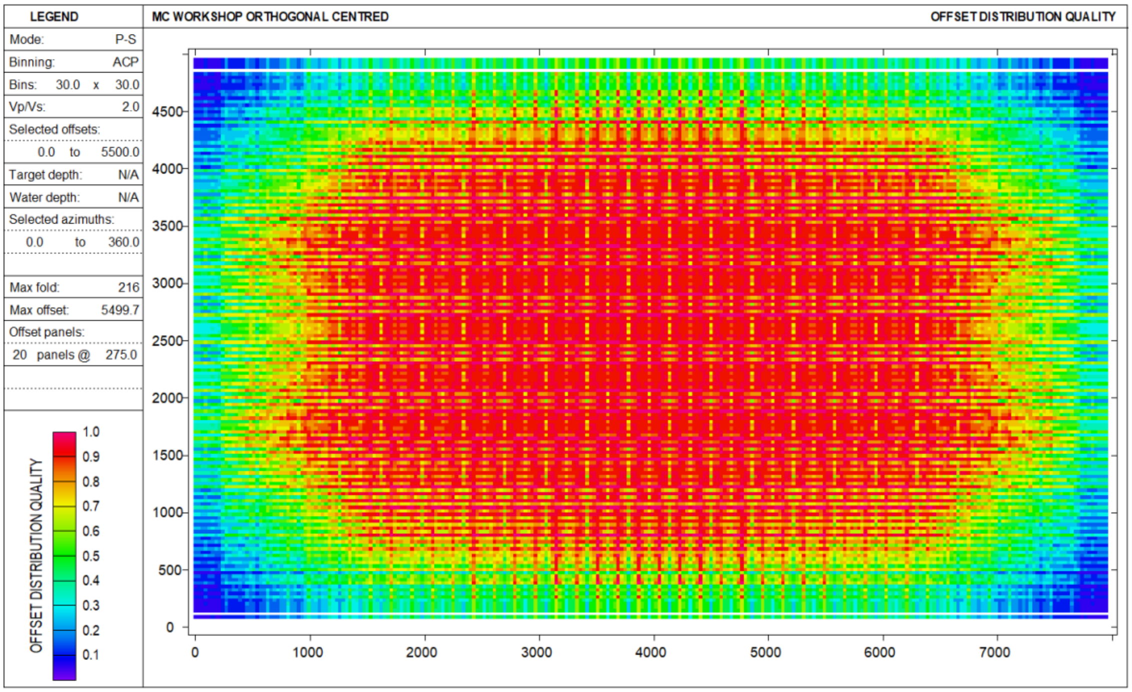

(d)

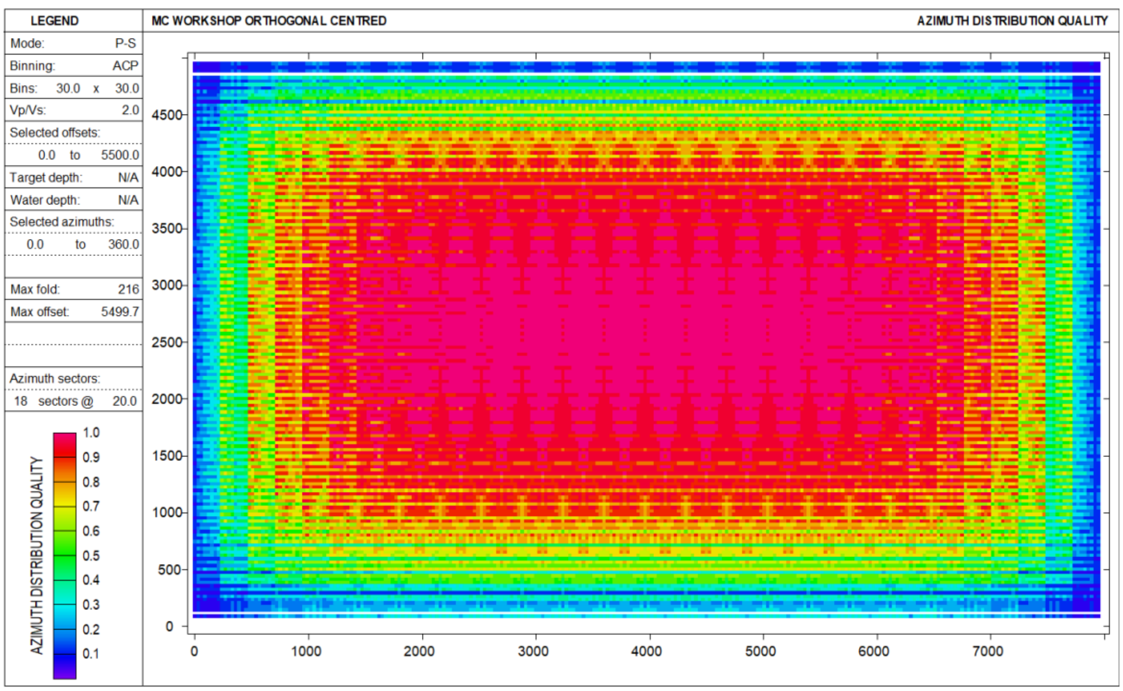

Figure 3.11: P-S asymptotic maps: (a) fold, (b) offset range, (c) offset distribution and (d) azimuth distribution

The irregularities in the fold could be better observed in the illumination plot in Figure 3.12. Illumination plot is fold mapped to neighboring bins in the case when reflection points are not bin-centered. For other attributes, we evaluated the azimuth vs fold and offset vs fold plots in Figure 3.13.

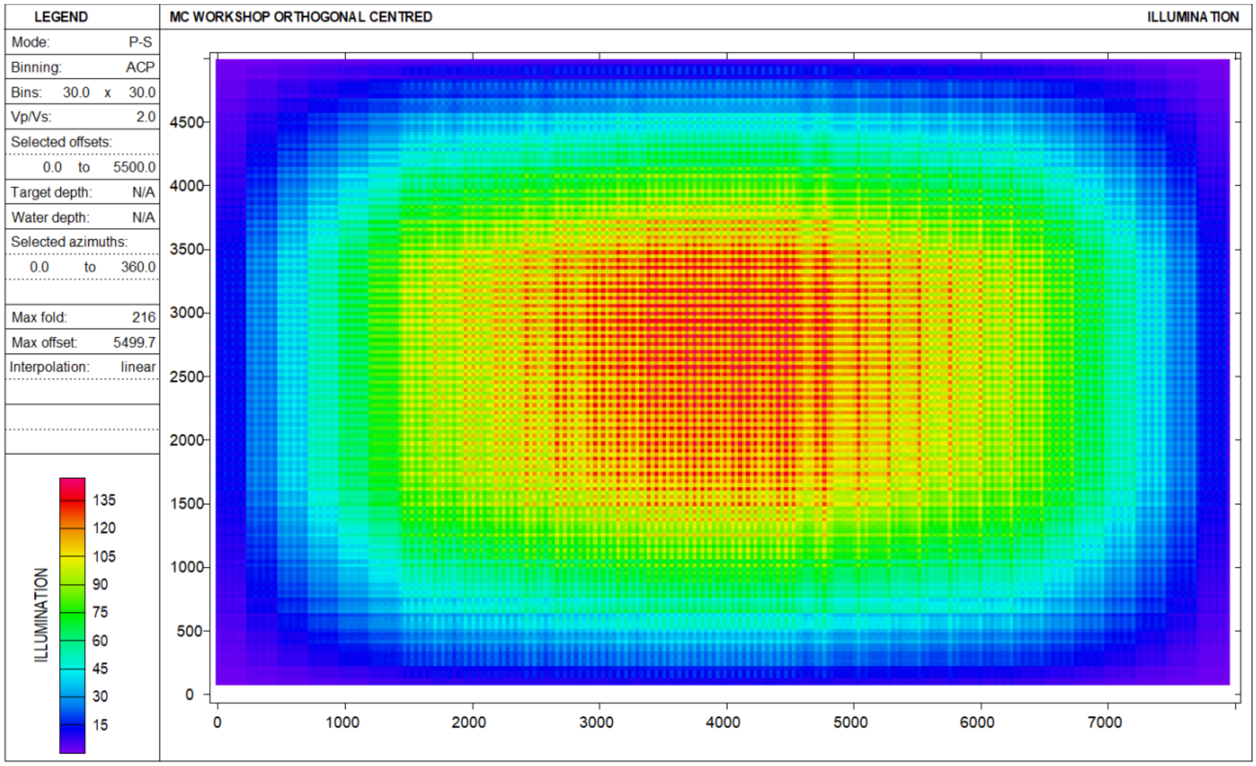

Figure 3.12: P-S asymptotic survey illumination map. Irregularities in the fold is clearly shown in the middle of the survey

One way to fix the issue of irregularities in P-S surveys is to change the geometry from orthogonal to slanted shot lines. However, that is not an option in this case as the real survey is already conducted as orthogonal. But, we can re-bin the survey to optimum bin size using equation 3.3 (Lawton, 1993):

$$\Delta Xc = \Delta r/(1 + \frac{Vs}{Vp}) \tag{3.3}$$

Where, ΔXc is ACP spacing and Δr is the offset between two adjacent receivers.

(a)

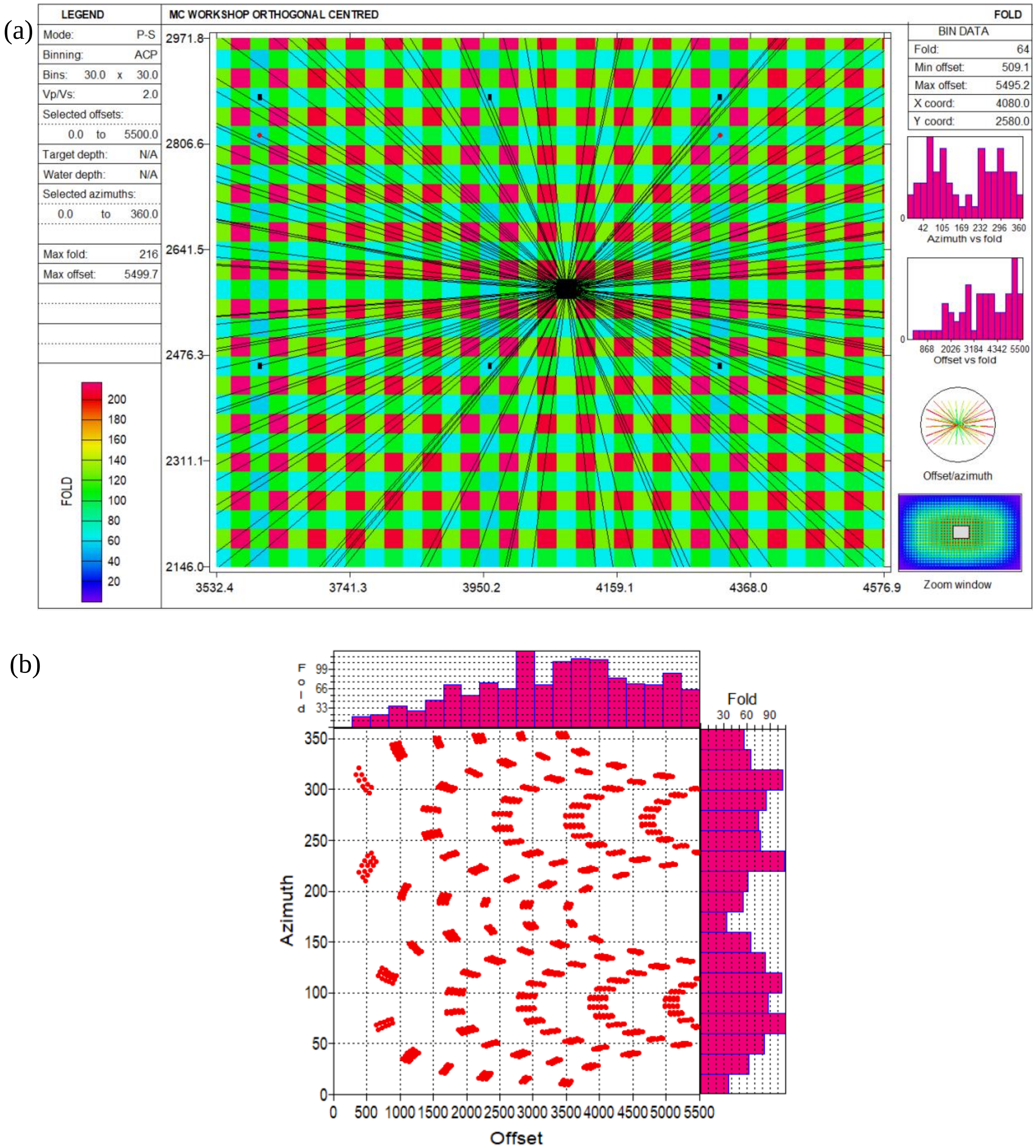

Figure 3.13: (a) From the zoomed in fold map, fold varies between neighboring bins. Also, a lot of bins have many traces coming from far offsets only as a result of coarse line spacing. (b) A less uniform distribution between azimuth and offset compared to the P-P survey design

(a)

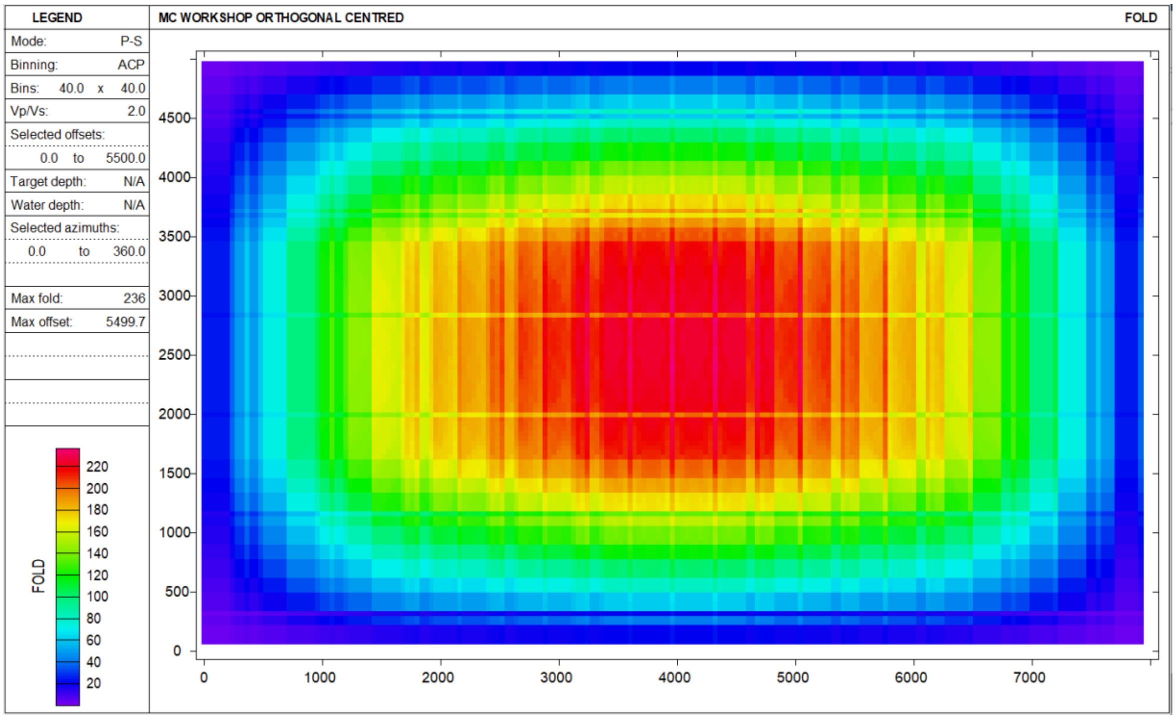
LEGEND
MC WORKSHOP ORTHOGONAL CENTRED
FOLD
Mode: P-S
Binning: ACP
Bins: 40.0 x 40.0
Vp/Vs: 2.0
Selected offsets:
0.0 to 5500.0
Target depth: N/A
Water depth: N/A
Selected azimuths:
0.0 to 360.0
Max fold: 236
Max offset: 5499.7
FOLD
220
200
180
160
140
120
100
80
60
40
20
4500
4000
3500
3000
2500
2000
1500
1000
500
0
0
1000
2000
3000
4000
5000
6000
7000

(b)

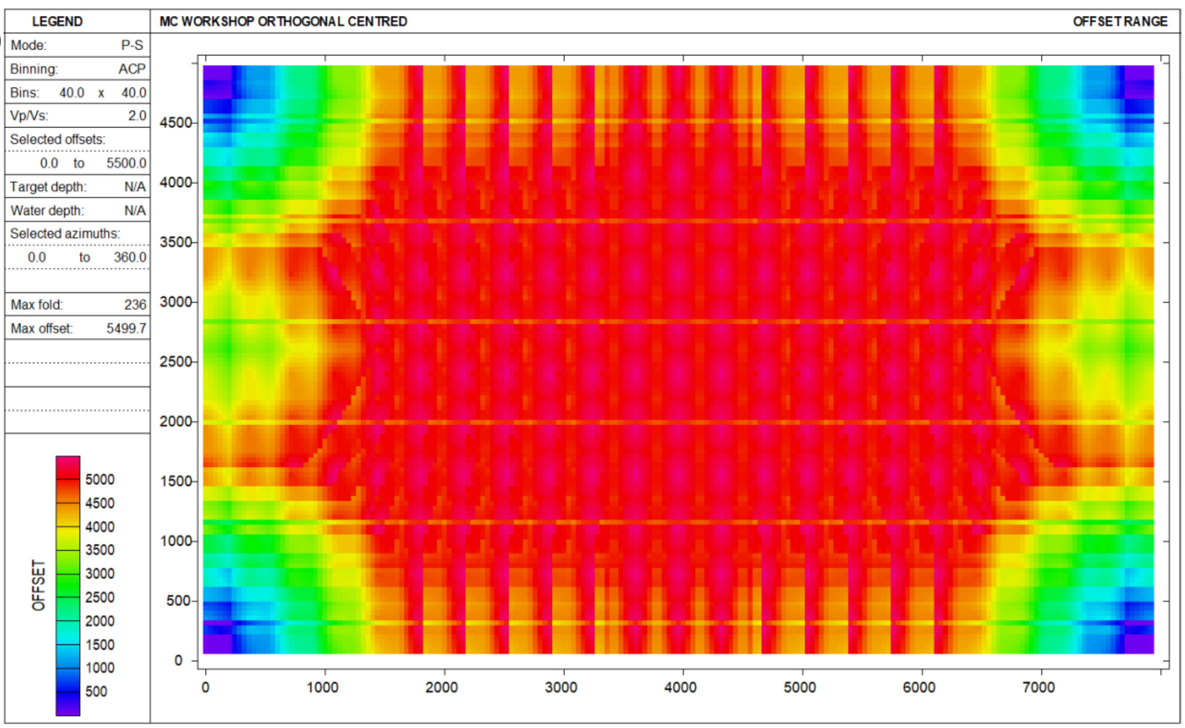
LEGEND
MC WORKSHOP ORTHOGONAL CENTRED
OFFSET RANGE
Mode: P-S
Binning: ACP
Bins: 40.0 x 40.0
Vp/Vs: 2.0
Selected offsets:
0.0 to 5500.0
Target depth: N/A
Water depth: N/A
Selected azimuths:
0.0 to 360.0
Max fold: 236
Max offset: 5499.7
OFFSET
5000
4500
4000
3500
3000
2500
2000
1500
1000
500
4500
4000
3500
3000
2500
2000
1500
1000
500
0
0
1000
2000
3000
4000
5000
6000
7000

(c)

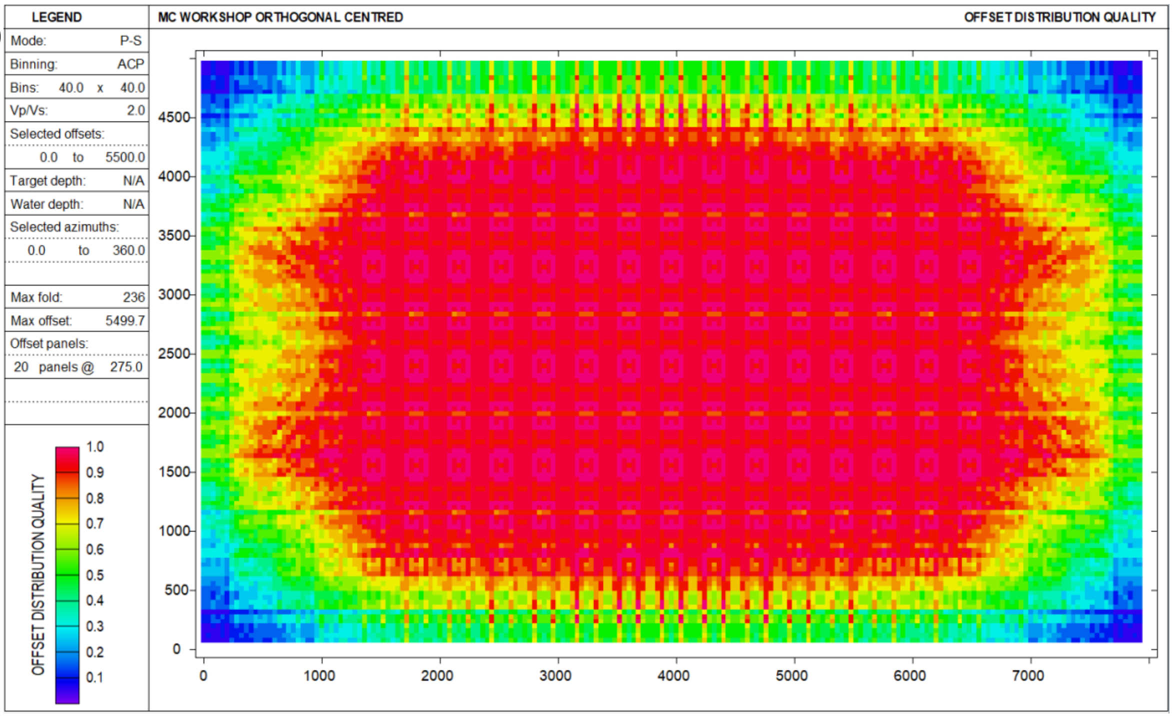

(d)

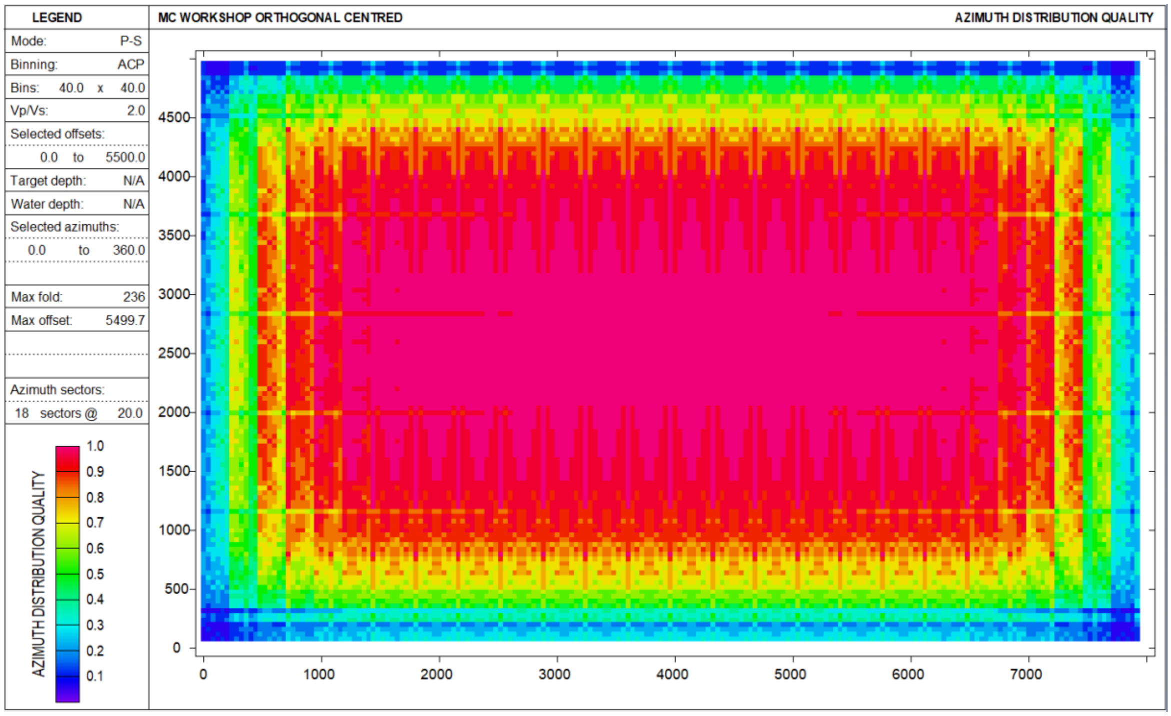

Figure 3.14: P-S asymptotic maps after re-binning: (a) fold, (b) offset range, (c) offset distribution and (d) azimuth distribution

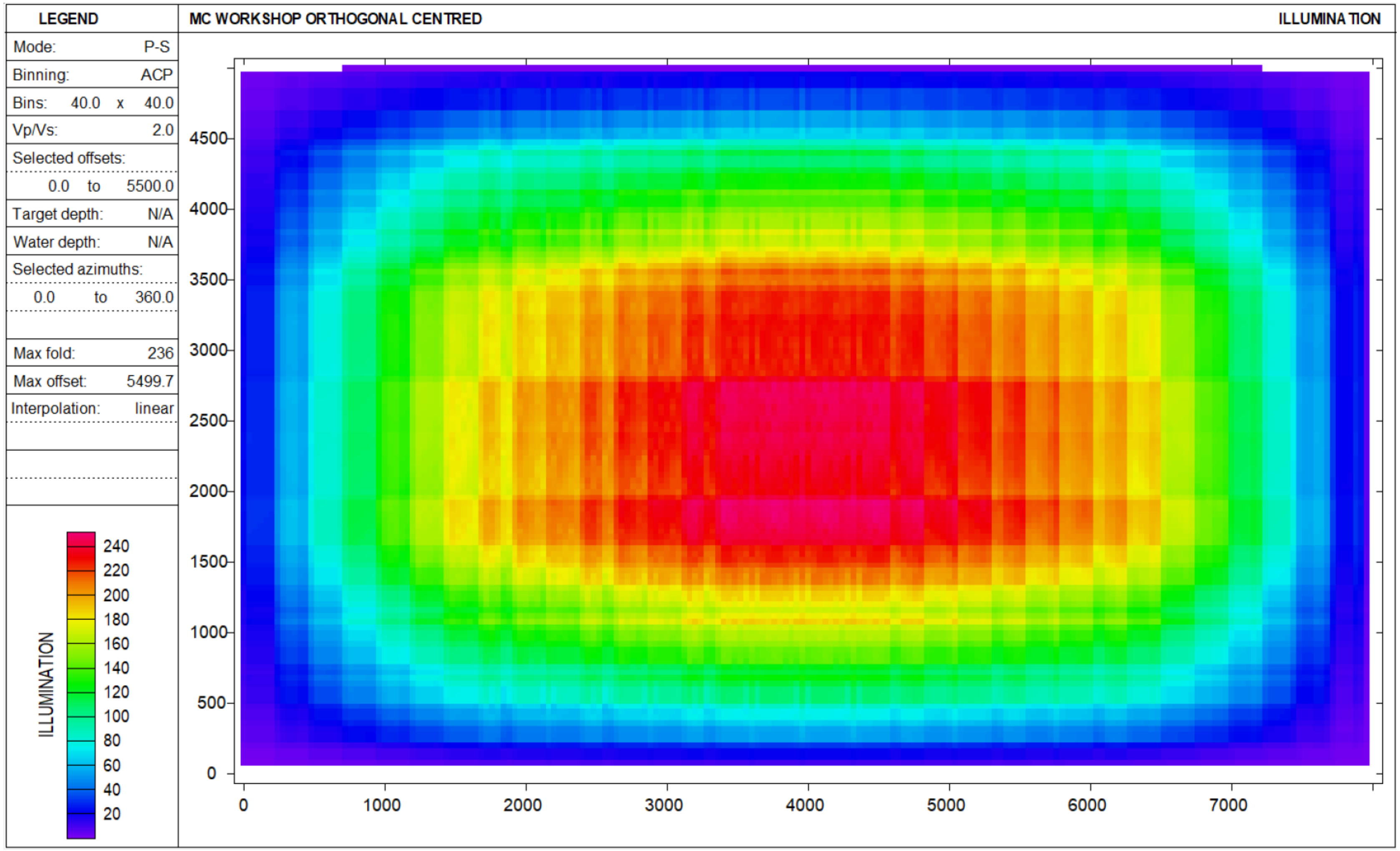

Figure 3.15: P-S asymptotic survey illumination map after re-binning. Irregularities in the fold have decreased in the middle of the survey

(a)

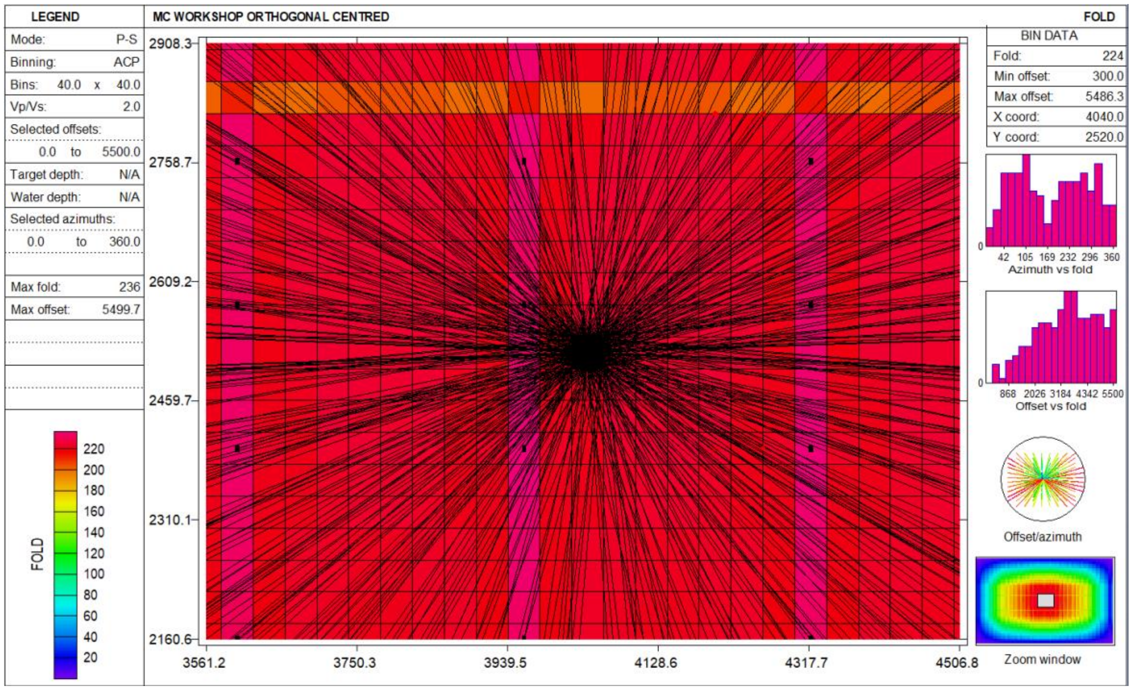

(b)

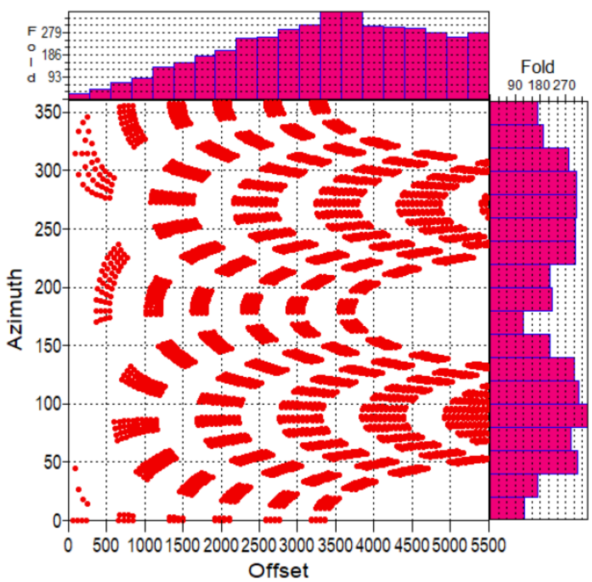

Figure 3.16: (a) From the zoomed in fold map, fold looks more consistent between neighboring bins than it was before the re-binning. More traces from near offsets are contributing to a bin in the middle of the survey, which helps with fold regularity. (b) beside the increase of the fold, we have better azimuth distribution compared to before the re-binning

3.4.3 P-S design (depth-specific)

In this method, we used PS Design to calculate attributes at a certain depth using conversion point instead of the asymptote. The conversion point at a certain depth is calculated by solving the fourth-degree polynomial equation 3.4 (Tessmer and Behle, 1988):

$$D^4 + (Z_c^2 - x^2)D^2 - xkZ_c^2 D + \frac{x^2}{2}\left(\frac{x^2}{2} + Z_c^2\right) = 0 \qquad (3.4)$$

Where Z_c is layer thickness, x is source-receiver offset and k is defined by equation 3.5:

$$k = \left(1 + {}^{V_S}/_{V_P}\right) / \left(1 - {}^{V_S}/_{V_P}\right) \qquad (3.5)$$

This method helps us know the vertical resolution in our depth of interest by evaluating the fold map at that depth in addition to other attributes. The depth of interest is between the Devonian Woodbend (3282.7 m) and Duvernay formations (3431.6 m). We selected a depth of 3431 m for this evaluation as a depth of interest.

First, we will evaluate the attributes with the conventional CMP bin size (30x30 m). Then, we will re-bin the grid and compare the two. The maps in Figures 3.18 and 3.19 show the attributes of this method before re-binning.

(a)

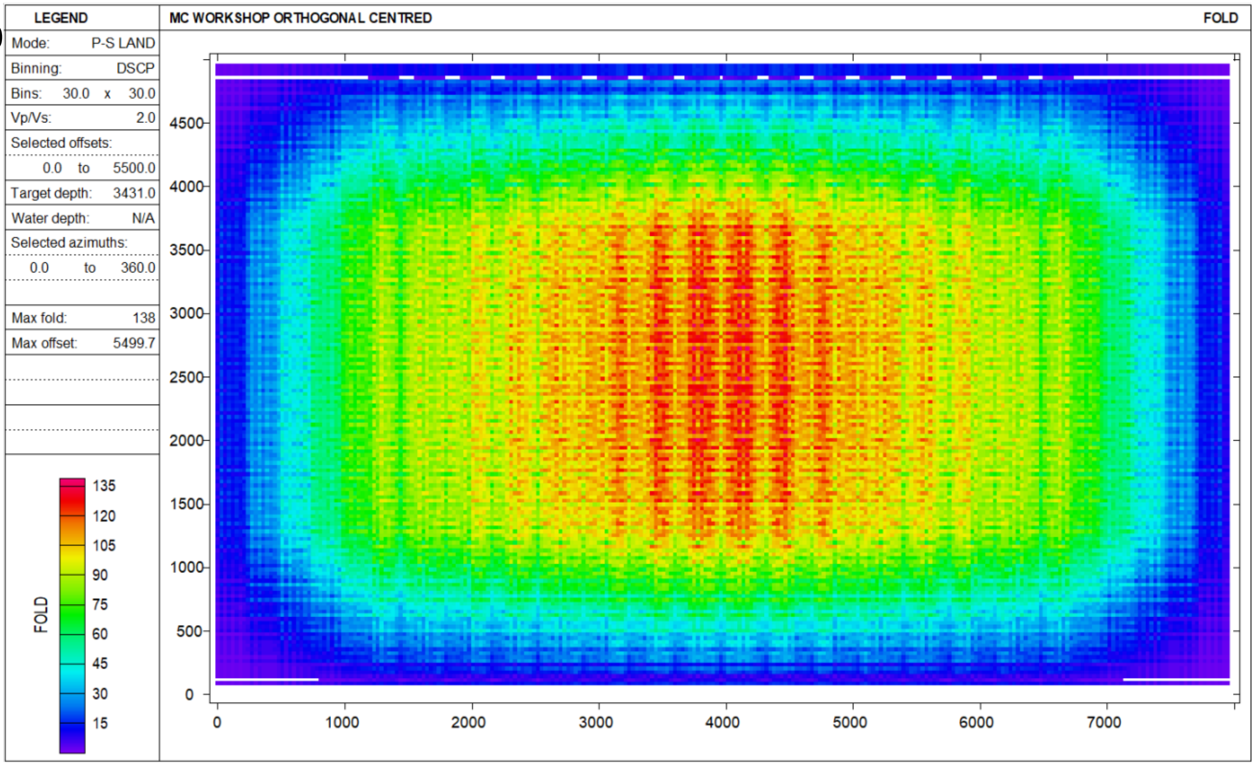
LEGEND
MC WORKSHOP ORTHOGONAL CENTRED
FOLD
Mode: P-S LAND
Binning: DSCP
Bins: 30.0 x 30.0
Vp/Vs: 2.0
Selected offsets:
0.0 to 5500.0
Target depth: 3431.0
Water depth: N/A
Selected azimuths:
0.0 to 360.0
Max fold: 138
Max offset: 5499.7
FOLD
135
120
105
90
75
60
45
30
15
4500
4000
3500
3000
2500
2000
1500
1000
500
0
0
1000
2000
3000
4000
5000
6000
7000

(b)

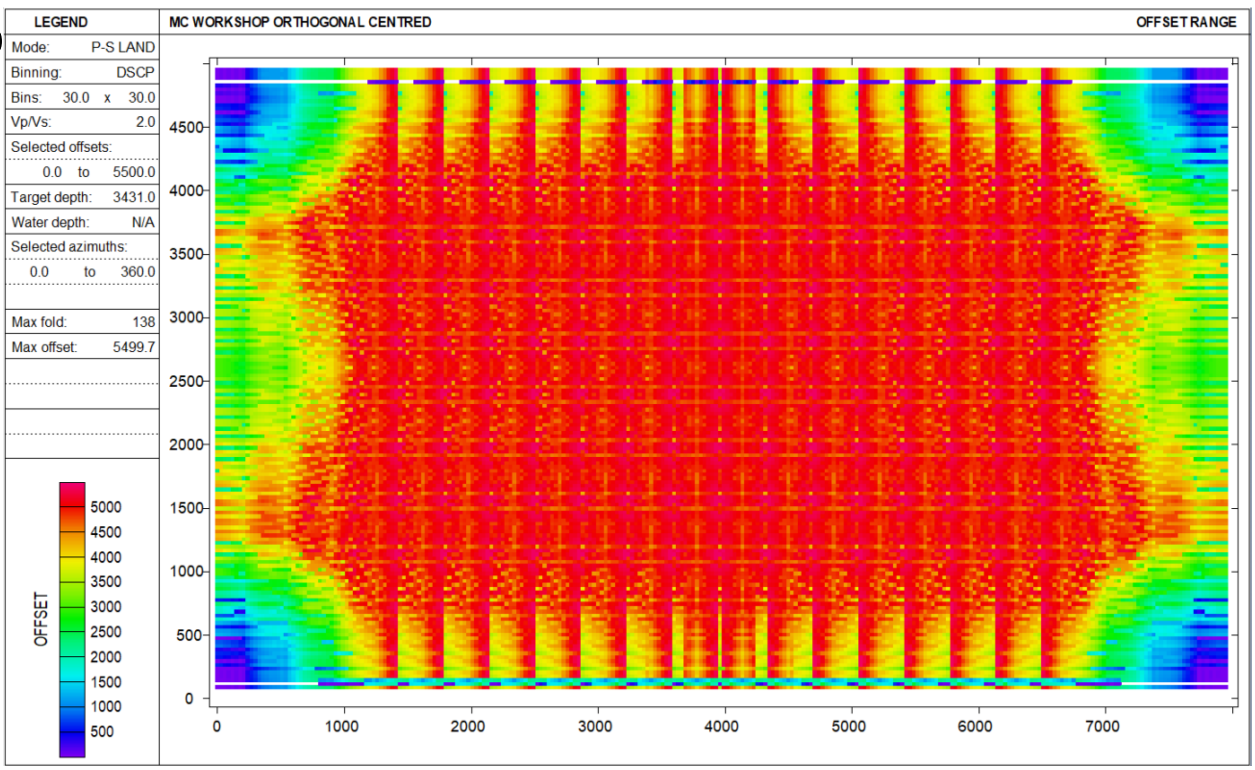
LEGEND
MC WORKSHOP ORTHOGONAL CENTRED
OFFSET RANGE
Mode: P-S LAND
Binning: DSCP
Bins: 30.0 x 30.0
Vp/Vs: 2.0
Selected offsets:
0.0 to 5500.0
Target depth: 3431.0
Water depth: N/A
Selected azimuths:
0.0 to 360.0
Max fold: 138
Max offset: 5499.7
OFFSET
5000
4500
4000
3500
3000
2500
2000
1500
1000
500
4500
4000
3500
3000
2500
2000
1500
1000
500
0
0
1000
2000
3000
4000
5000
6000
7000

(c)
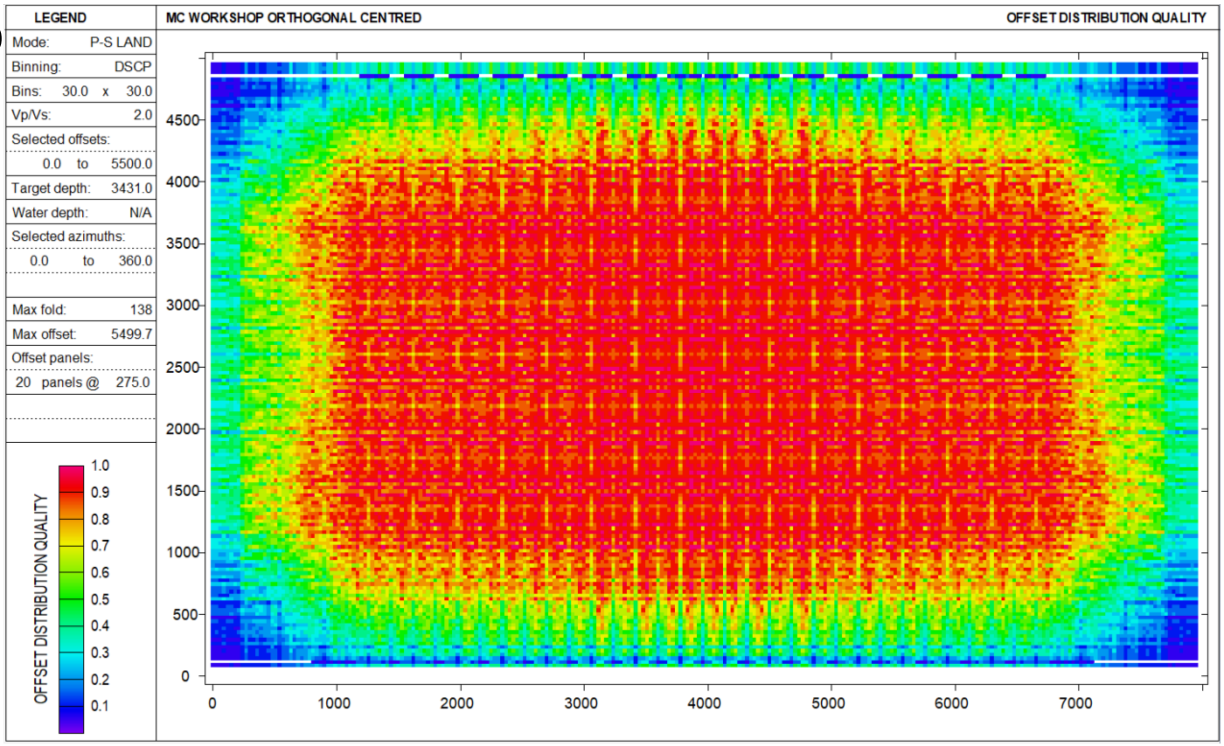

(d)
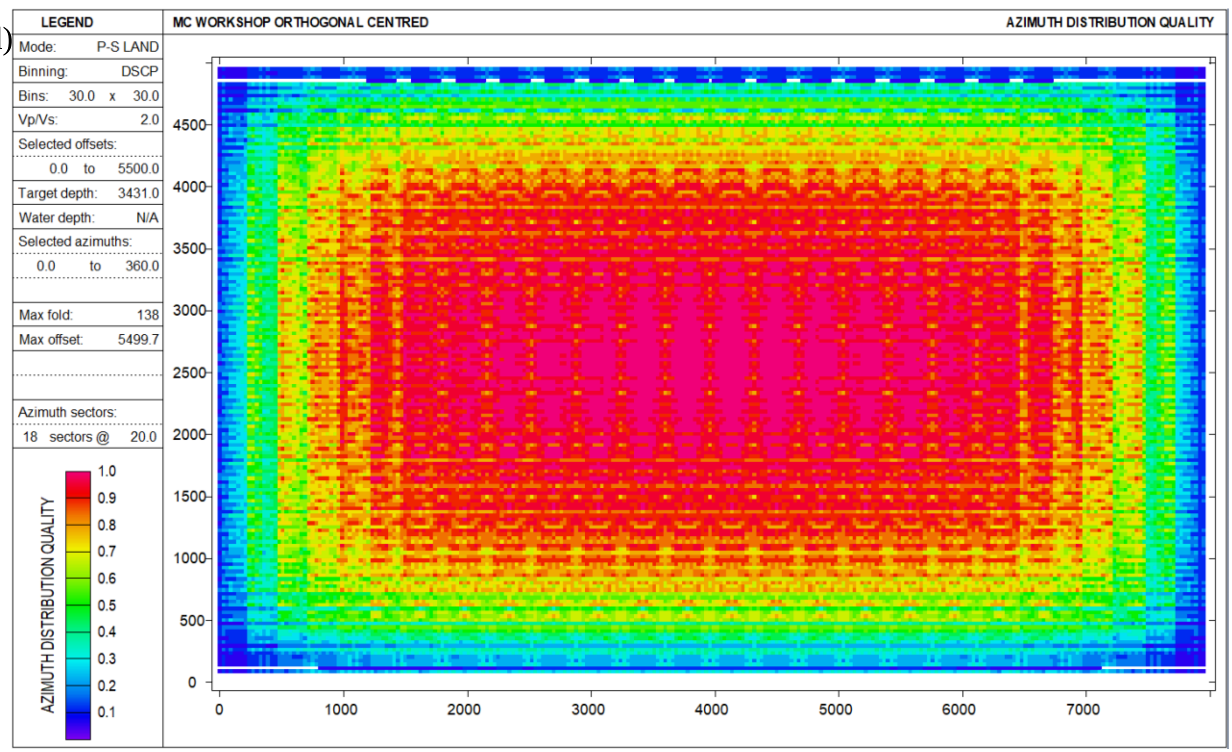

Figure 3.18: P-S depth-specific maps: (a) fold, (b) offset range, (c) offset distribution and (d) azimuth distribution

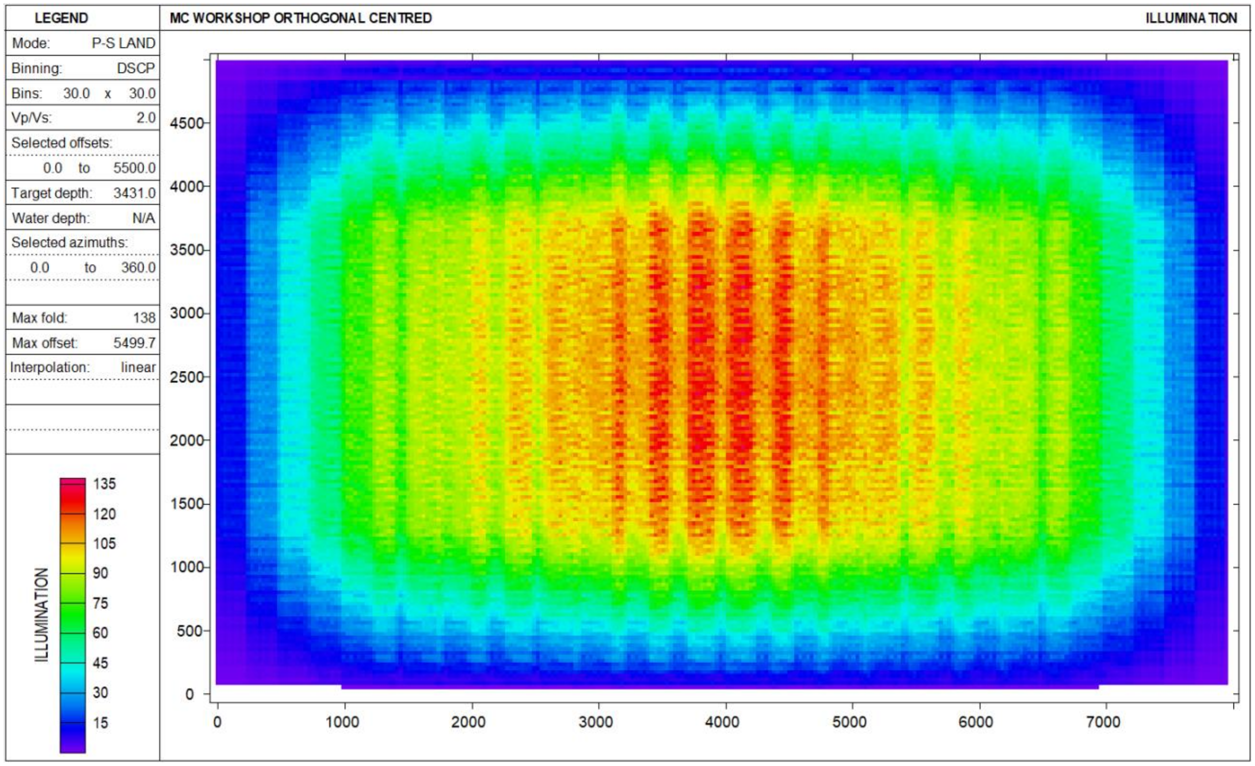

Figure 3.19: P-S depth-specific survey illumination map. Irregularities are reduced compared with the asymptotic illumination before the re-binning

Similar to the P-S asymptotic survey, grid is re-binned with the optimum bin size (40x40 m). The resulted maps are shown in Figures 3.21 and 3.22.

(a)

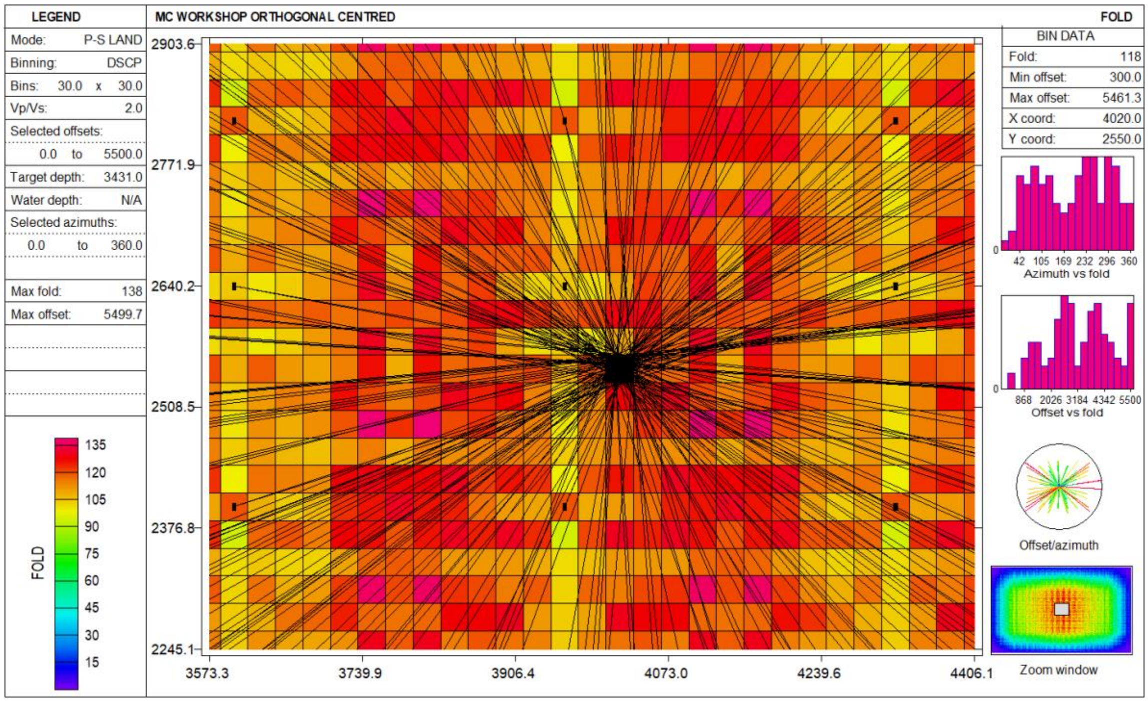

(b)

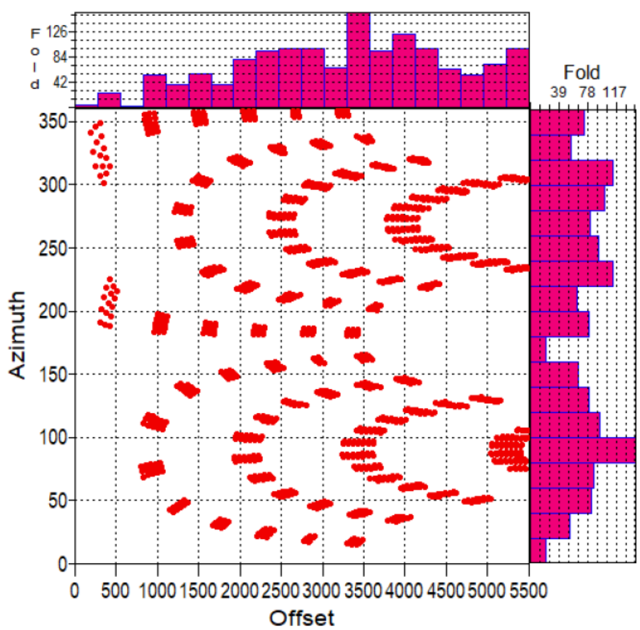

Figure 3.20: (a) Zoomed in fold map, fold varies between neighboring bins. The variation is not as significant as the asymptotic survey before re-binning. (b) Similar distribution between azimuth and offset compared to the P-P survey design

(a)
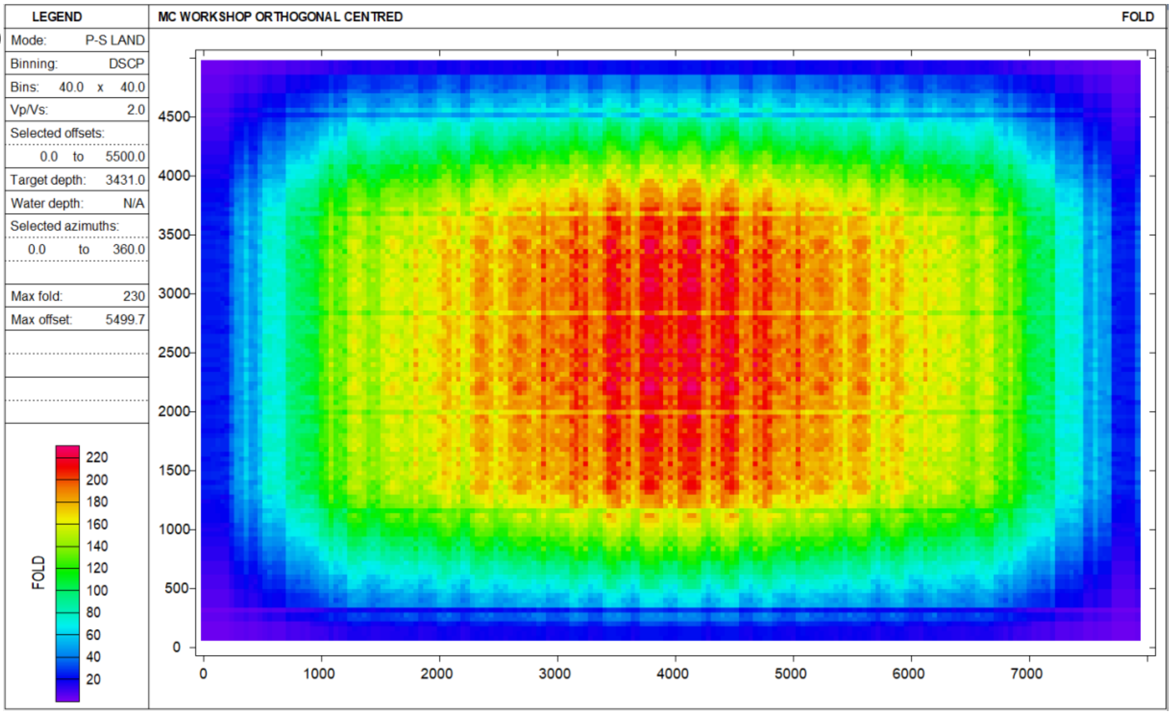
LEGEND
MC WORKSHOP ORTHOGONAL CENTRED
FOLD
Mode: P-S LAND
Binning: DSCP
Bins: 40.0 x 40.0
Vp/Vs: 2.0
Selected offsets:
0.0 to 5500.0
Target depth: 3431.0
Water depth: N/A
Selected azimuths:
0.0 to 360.0
Max fold: 230
Max offset: 5499.7
FOLD
220 200 180 160 140 120 100 80 60 40 20
4500 4000 3500 3000 2500 2000 1500 1000 500 0
0 1000 2000 3000 4000 5000 6000 7000

(b)
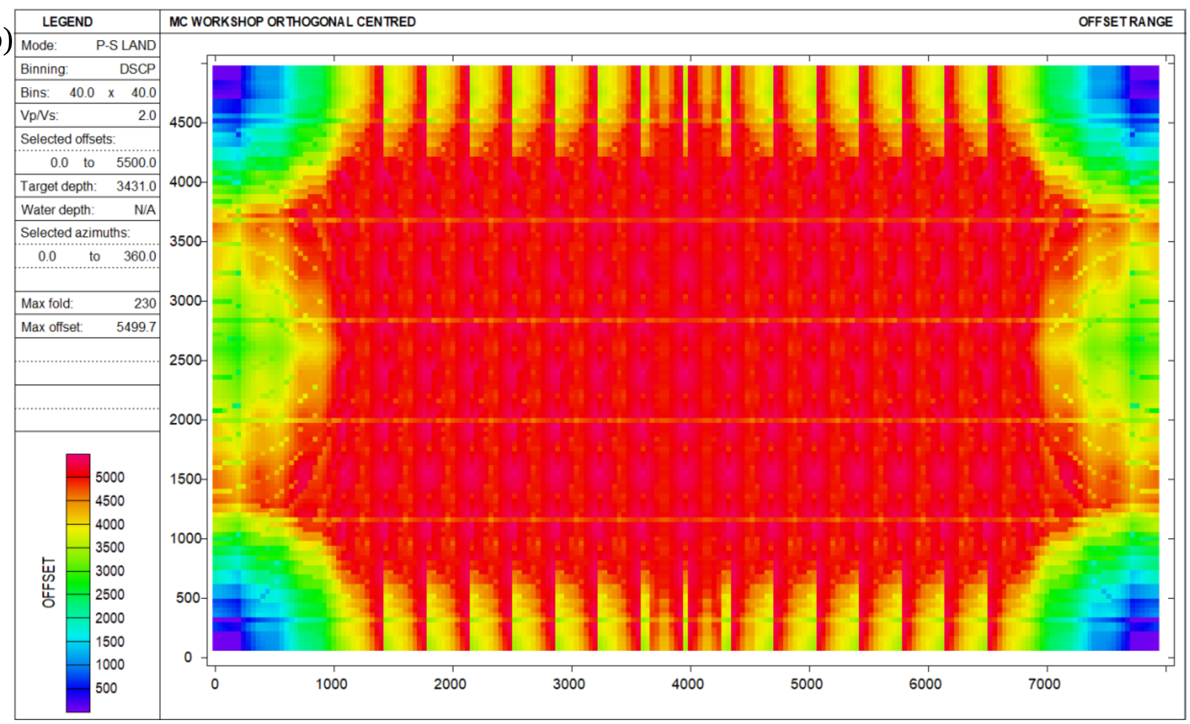
LEGEND
MC WORKSHOP ORTHOGONAL CENTRED
OFFSET RANGE
Mode: P-S LAND
Binning: DSCP
Bins: 40.0 x 40.0
Vp/Vs: 2.0
Selected offsets:
0.0 to 5500.0
Target depth: 3431.0
Water depth: N/A
Selected azimuths:
0.0 to 360.0
Max fold: 230
Max offset: 5499.7
OFFSET
5000 4500 4000 3500 3000 2500 2000 1500 1000 500
4500 4000 3500 3000 2500 2000 1500 1000 500 0
0 1000 2000 3000 4000 5000 6000 7000

(c)

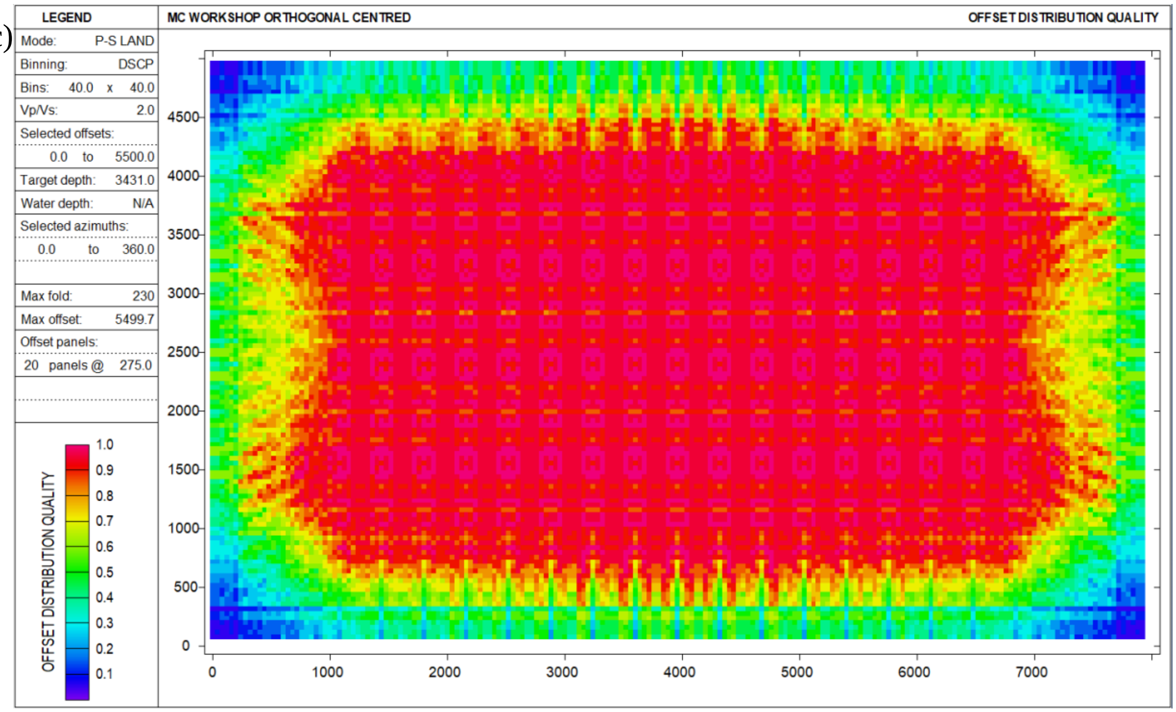

(d)

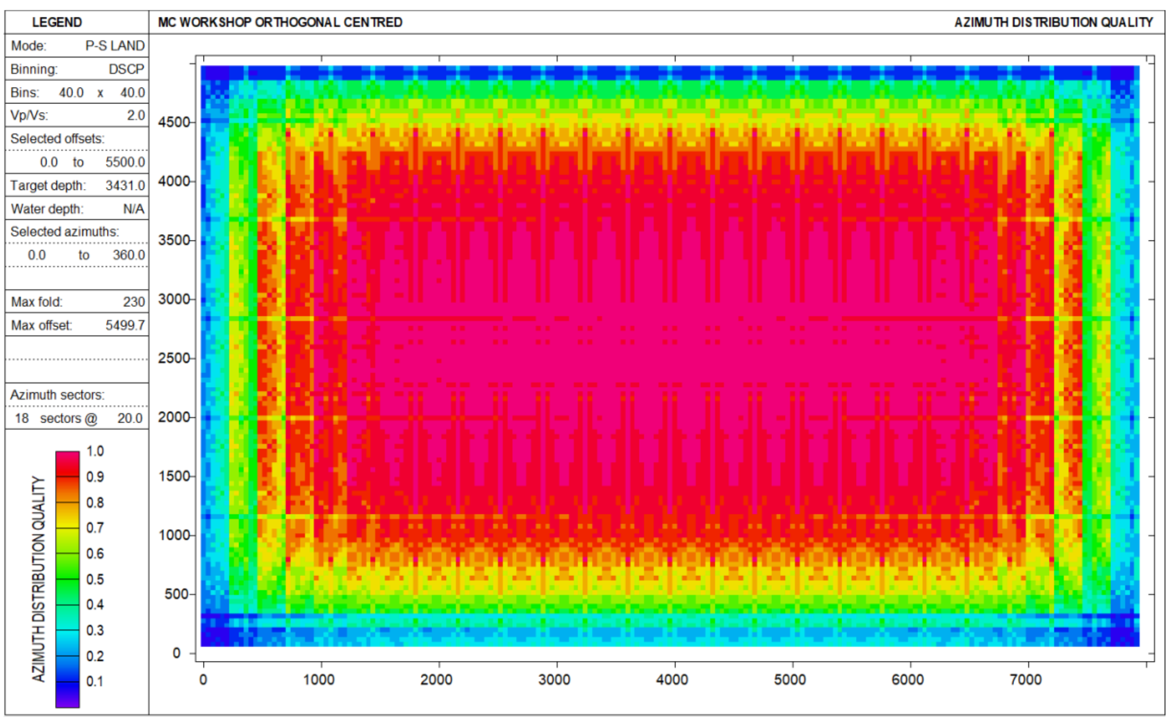

Figure 3.21: P-S depth-specific maps after re-binning: (a) fold, (b) offset range, (c) offset distribution and (d) azimuth distribution (bottom right)

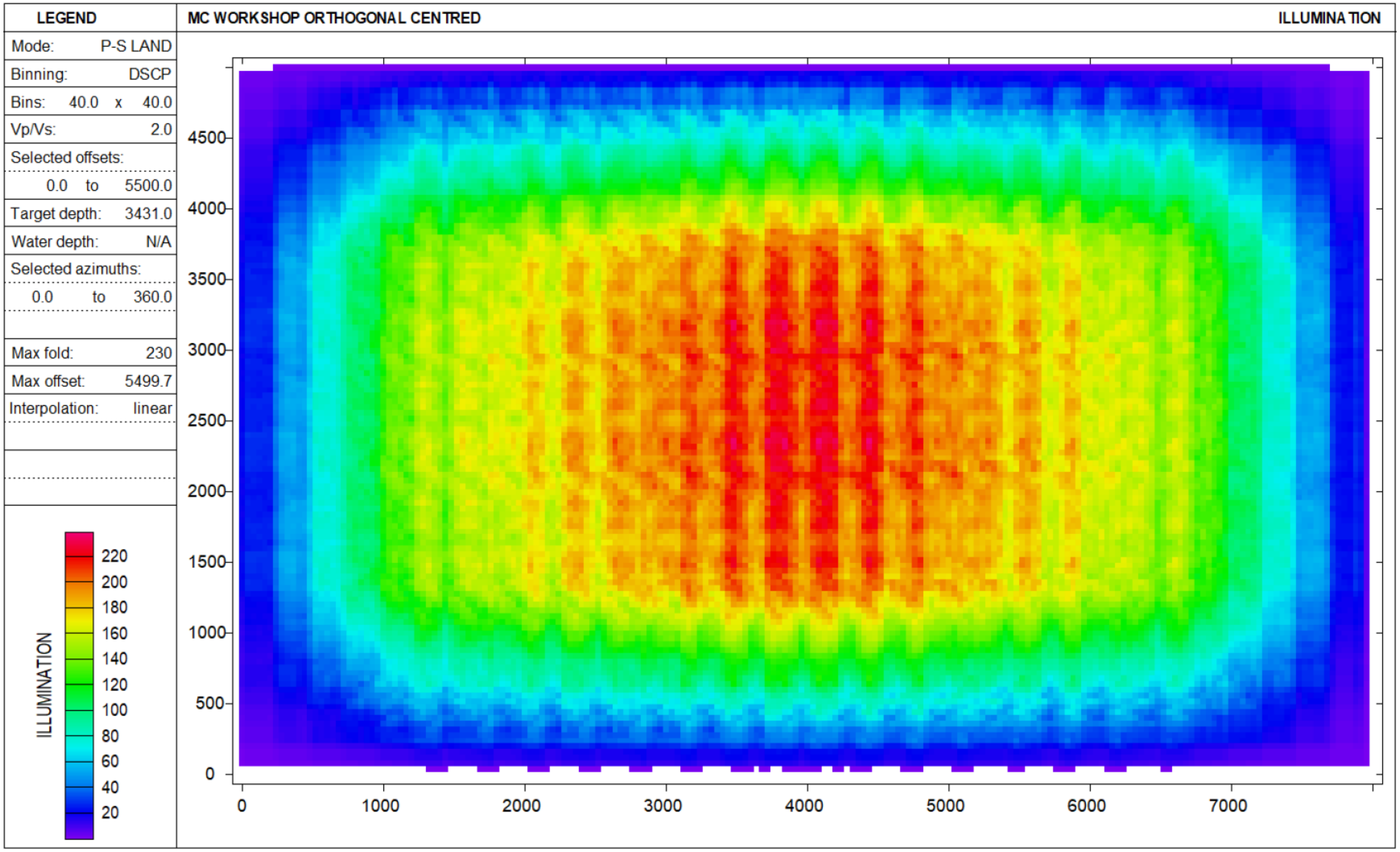

Figure 3.22: P-S depth-specific survey illumination map after re-binning. Irregularities in the fold are decreased in the middle of the survey. However, there is a zig zag pattern that was not there before re-binning

(a)

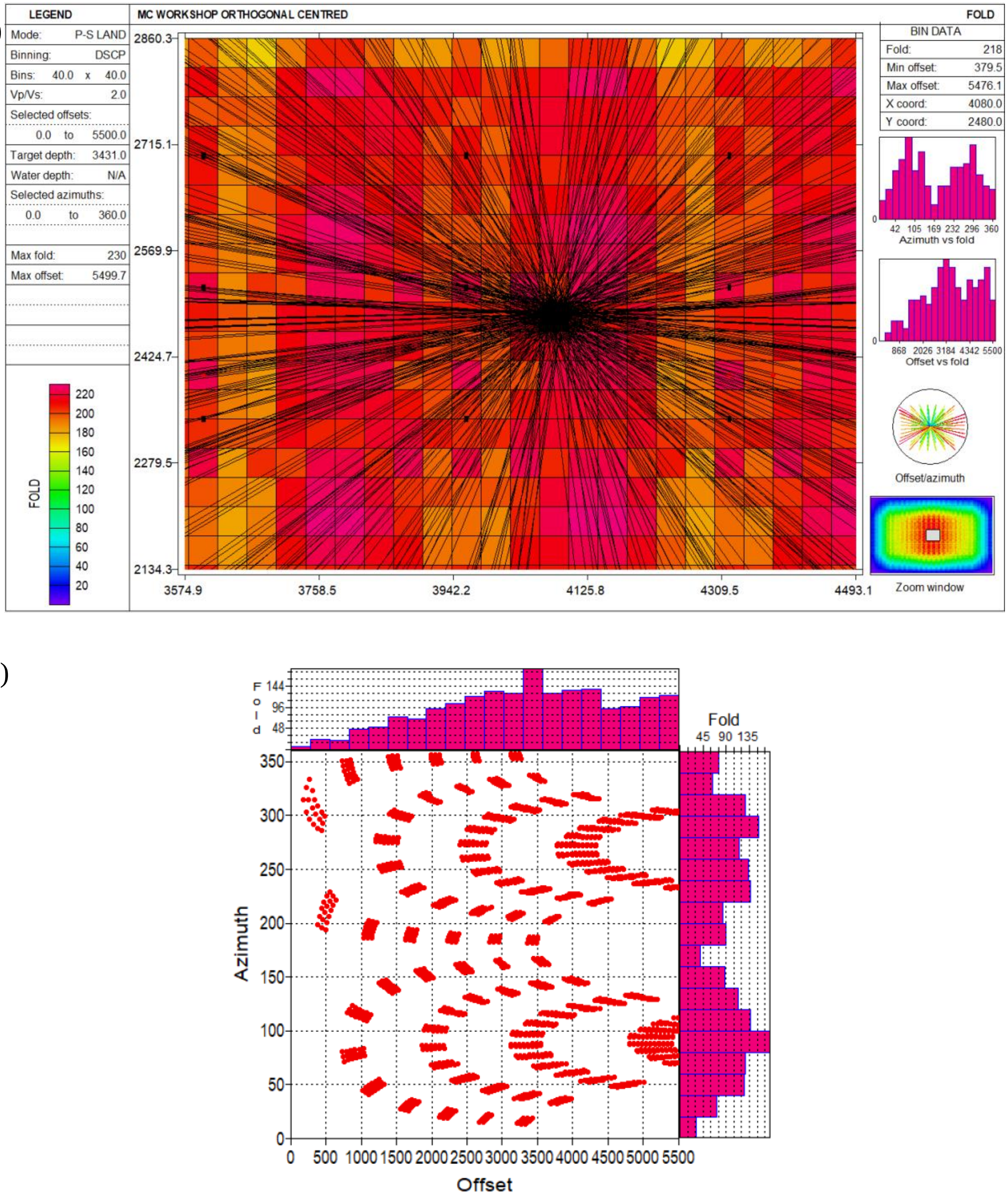

(b)

Figure 3.23: (a) Zoomed in fold map; fold looks more consistent between neighboring bins than it was before the re-binning. (b) More traces from far offsets are contributing to a bin in the middle of the survey, which helps with fold regularity

3.5 Discussion

P-P survey designs are binned using the conventional CMP binning. That is why the fold map and other attribute maps do not have any irregularities. In this case, the bin size was 30 x30m and the maximum offset, determined from the synthetic seismograms to be 4500 m for P-P and 5500 m for P-S. The nominal fold is 111 and it is regular through the nominal fold area in the middle of the survey.

For P-S asymptotic survey, V_p/V_s was provided to calculate the conversion points. The fold increased as expected. However, it was not regular along the nominal fold area. It is due to the change of conversion point locations with depth that the asymptotic method does not properly account for. One method to solve the issue of irregularities is to re-bin the grid to the optimum bin size. The optimum bin size for this survey parameters is calculated to be 40 x 40 m. After re-binning, fold increased as the larger bins will include more traces. Moreover, the re-binning helped to smooth the irregularities in all attributes consistently, as confirmed in the illumination map.

For the P-S depth-specific survey, similar procedures to the P-S asymptotic are followed, except that, the depth of interest is provided to evaluate the same attributes but at specific depth using Tessmer and Behle (1988) fourth-degree polynomial equation. More regular fold distribution is expected compared to the P-S asymptotic survey and the fold map shows better regularity than the P-S asymptotic fold before re-binning. That is because conversion points get closer to each other with depth. After re-binning, same thing happened as in P-S asymptotic survey, namely, the fold increased. Furthermore, the illumination map shows better regularity as indicated by the color bar although we see a small zig zag pattern in the map.

The question is, do the improvements on attribute maps after re-binning to optimum bin size lead to the improvement of subsurface imaging? Intuitively we can assume that the better azimuthal and offset distribution lead to influence the target illumination. Including more azimuths and offsets will provide an improved illumination of the subsurface. Moreover, we expect a higher signal-to-noise ratio and better lateral resolution after re-binning. Lastly, continuous and regular fold is required to have robust post-stack amplitude mapping and AVO analysis.

Chapter Four: **PROCESSING 3C3D BIGSTONE P-P DATA**

4.1 Introduction

The processing of the vertical component followed a conventional workflow from geometry to migration. However, processing the P-S data includes extra steps or different way of handling the data in other steps, as discussed in chapter 2 and detailed in chapter 5. In this chapter, we will go through the processing workflow steps for the P-P data.

4.2 Processing Workflow

Table 4.1: Processing workflow for the P-P data

1	Geometry	8	First Pass of Velocity Analysis
2	CMP Binning	9	First Pass Residual Statics
3	Elevation and Static Correction	10	Second Pass of Velocity Analysis
4	Gain Recovery	11	Second Pass Residual Statics
5	Surface Consistent Amplitude Scaling	12	NMO
6	Seismic Noise Attenuation	13	Stack
7	Surface Consistent Deconvolution	14	Post-Stack Time Migration

4.3 Processing workflow steps

4.3.1 Geometry

Data was already separated in three datasets; the vertical, H1 and H2 as shown in Figure 4.1. Therefore, shot and receiver coordinates were read from the headers and stored in the geometry database in ProMax. We calculated the CMP grid and then geometry was loaded into the three datasets. Figure 4.2 shows source-receiver geometry and fold maps.

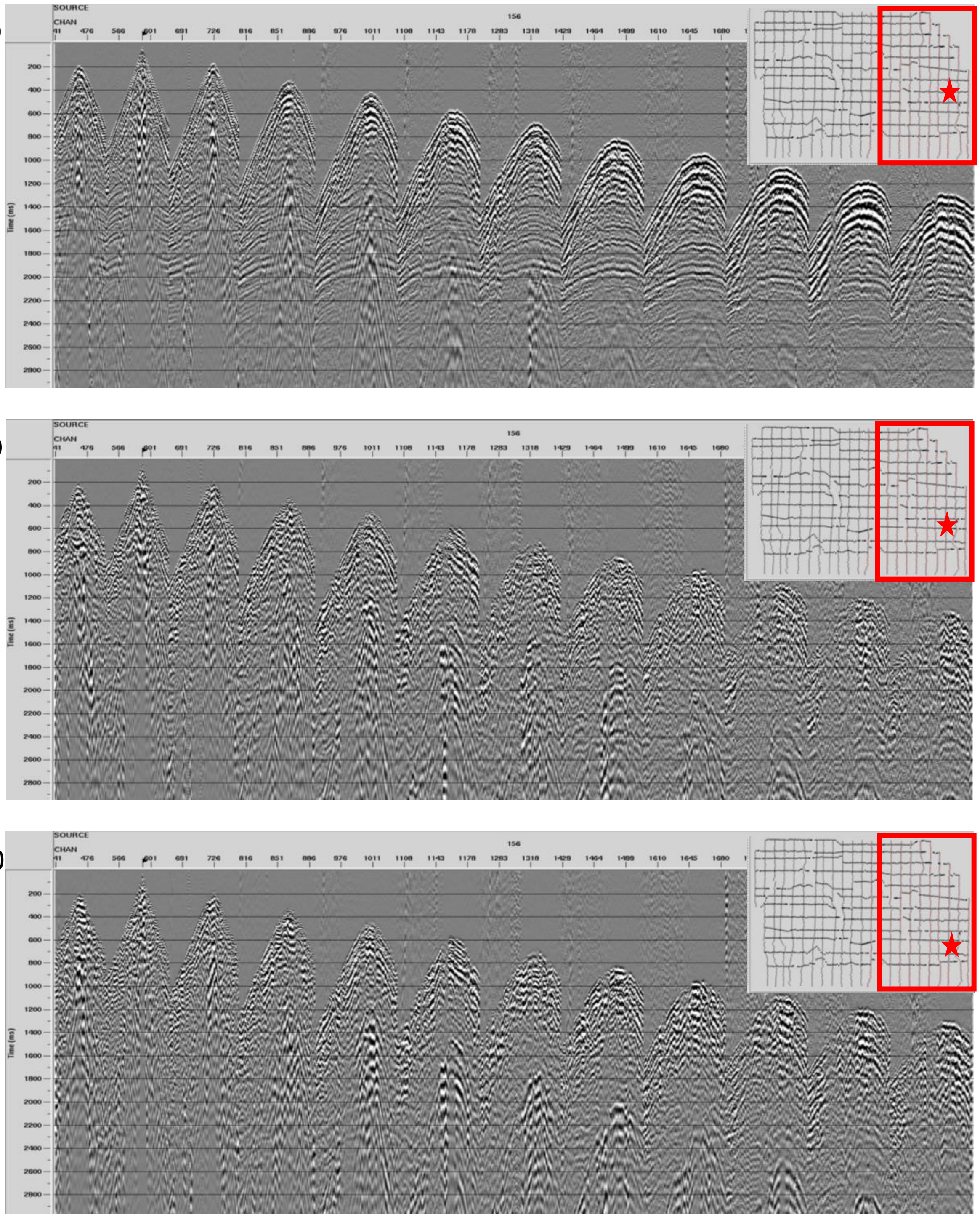
(a)
(b)
(c)

Figure 4.1: (a) Raw shot gather data for the vertical component, (b) H1 and (c) H2. First break and the shallow area is clearer in the vertical component than the H1 and H2 ones. Surface wave energy is more identifiable on the H1 and H2 records than the vertical component

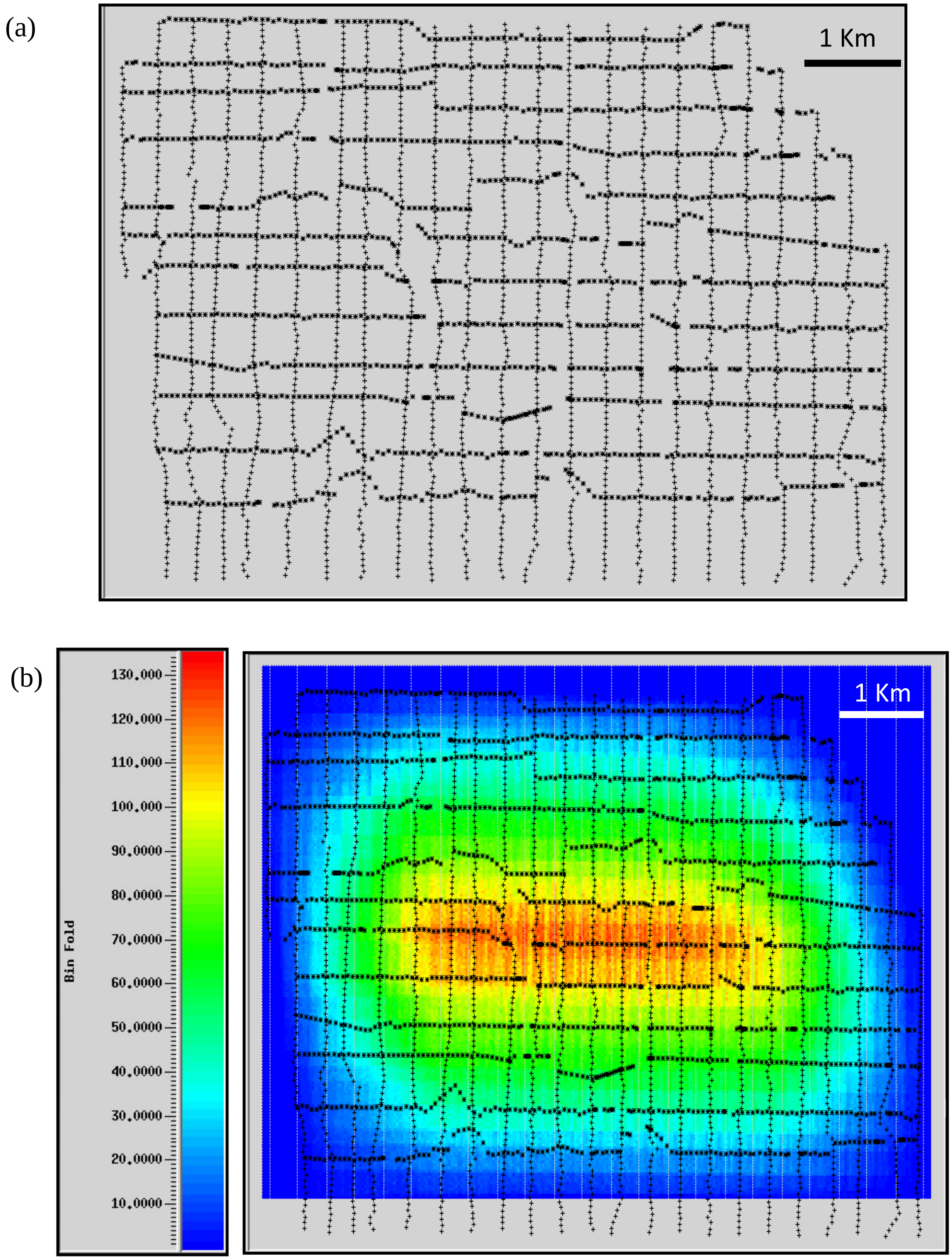

Figure 4.2: (a) Source-receiver geometry map in ProMAX. Shots are E-W and receivers are N-S. (b) Fold map using CMP grid overlaid on the source-receiver geometry map, the nominal fold is 145. The fold distribution looks similar the fold of P-P design in chapter 2

4.3.2 Binning

For the vertical component, the binning was completed using the common midpoint grid.

4.3.3 Elevation Statics

The replacement velocity was decided by taking the average velocity value of a range of first breaks as in Figure 4.3. And the final datum elevation is chosen based on the elevation map of the survey area as shown in Figure 4.4.

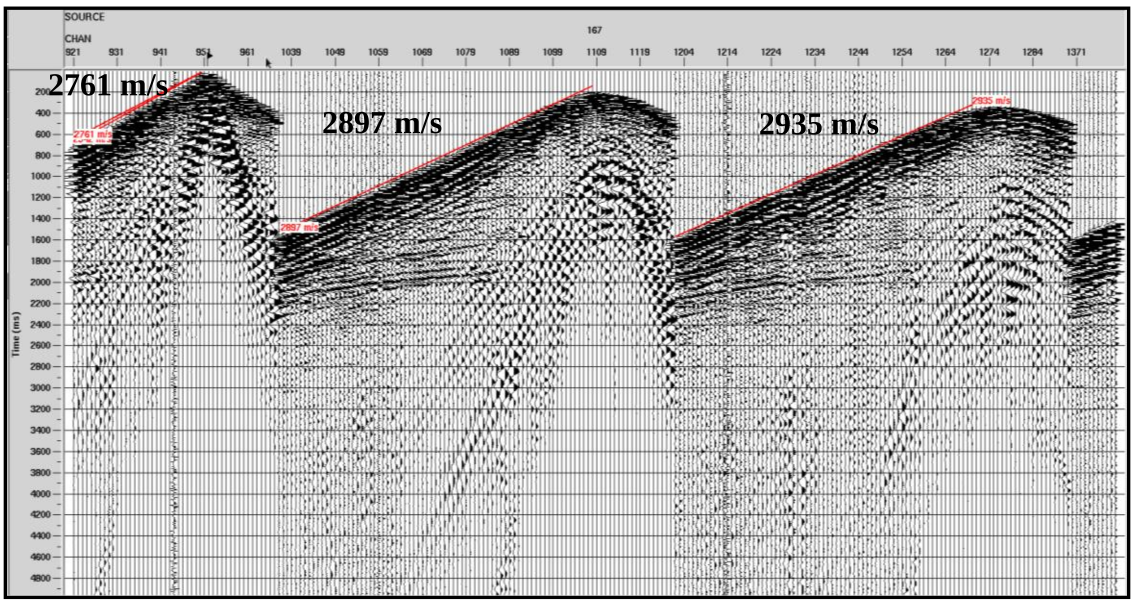

Figure 4.3: Velocities of random first breaks. The replacement velocity is chosen to be 2800 m/s

4.3.4 Static Correction

The near surface model (long wavelength and short wavelength statics) was obtained from the refraction tomography using the first break picks. Because the vertical component data is not noisy and the first breaks are easy to indicate, auto pick was run to pick the first breaks as shown in Figure 4.5. QC and minor edits were made to some of the noisier shots. Finally, first break picks were reliable through the whole survey.

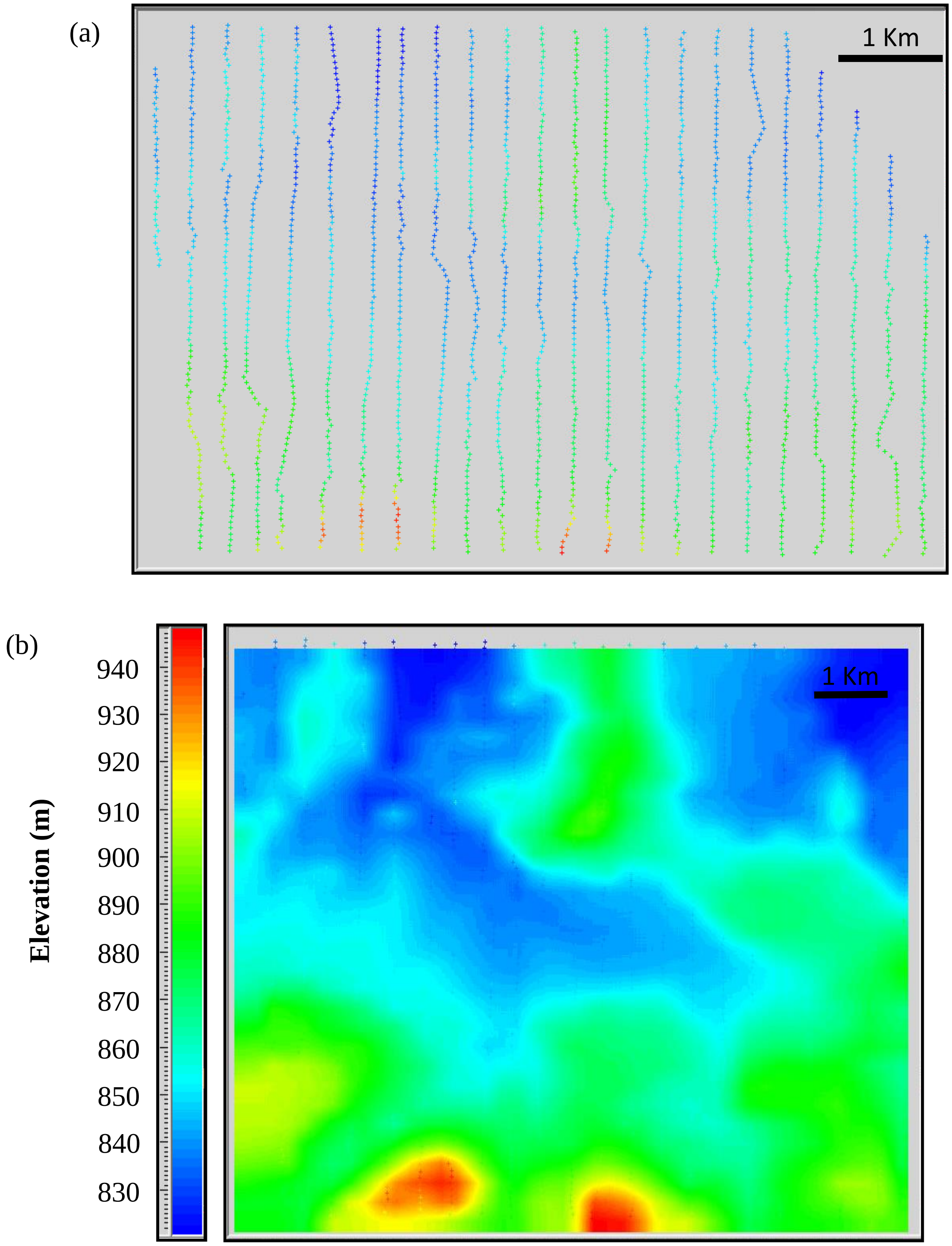

Figure 4.4: (a) Receiver elevation map. (b) Interpolated elevation map. The highest elevation in the area is 947.6 m

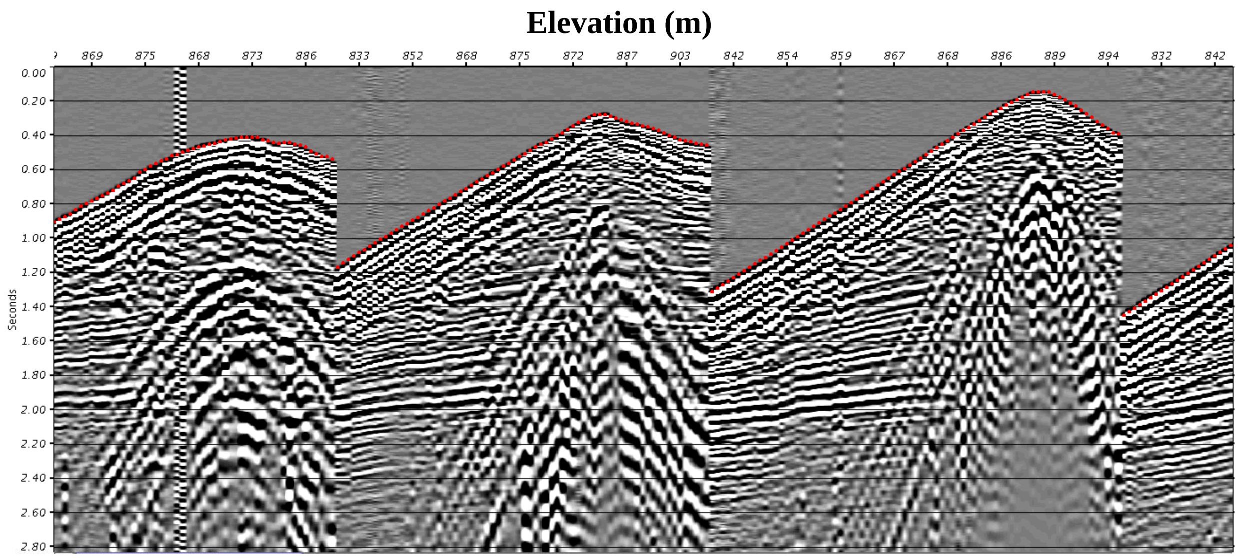

Figure 4.5: The auto-picked first break traveltimes for the vertical component

The auto-picked first arrival traveltimes are an input to create an initial velocity-depth model. Figure 4.6 shows the traveltimes for a single shot for QC. The traveltimes for every shot are plotted to shot-offset distance to build initial model as shown in Figure 4.7. These steps were repeated for the rest of the shots. The initial velocity model is the input for the final velocity model. The number of iterations used was 10, and Figure 4.8 shows the RMS misfit for every iteration.

The final velocity model computed using the initial one is shown in Figure 4.9. the black lines represent the floating and final datums. This velocity model is the one used to calculate the 3D static solution for the whole survey as shown in Figure 4.10.

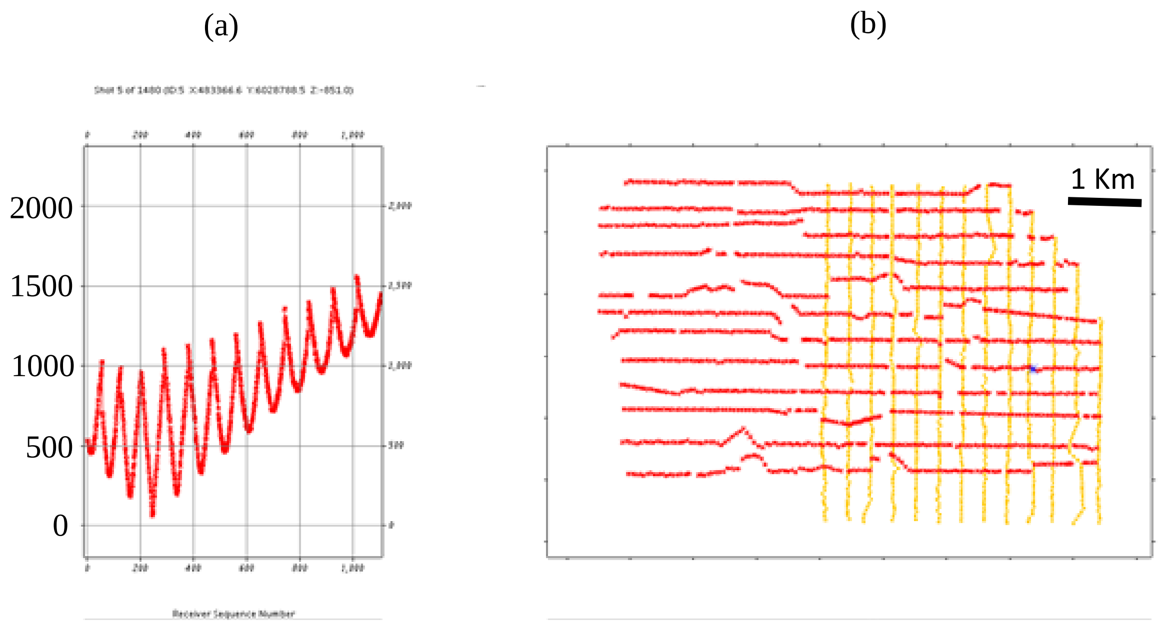

Figure 4.6: (a) The plot of first break for all the receivers related to (b) the shot in blue in the geometry map on the right

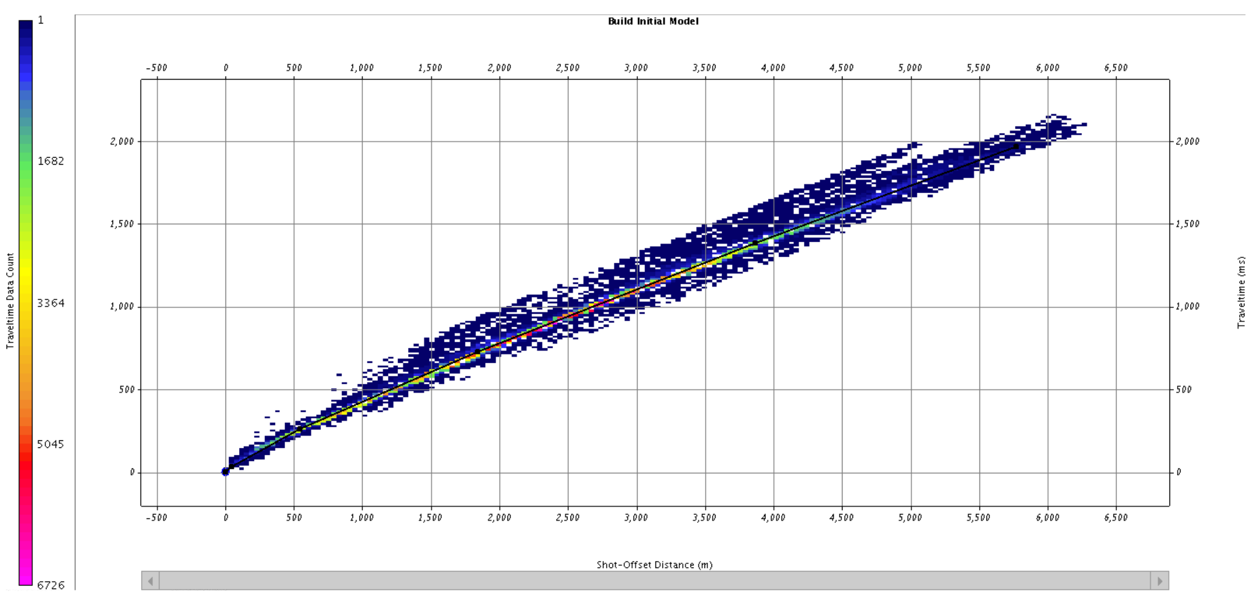

Figure 4.7: Building an initial velocity model based on the first break traveltimes

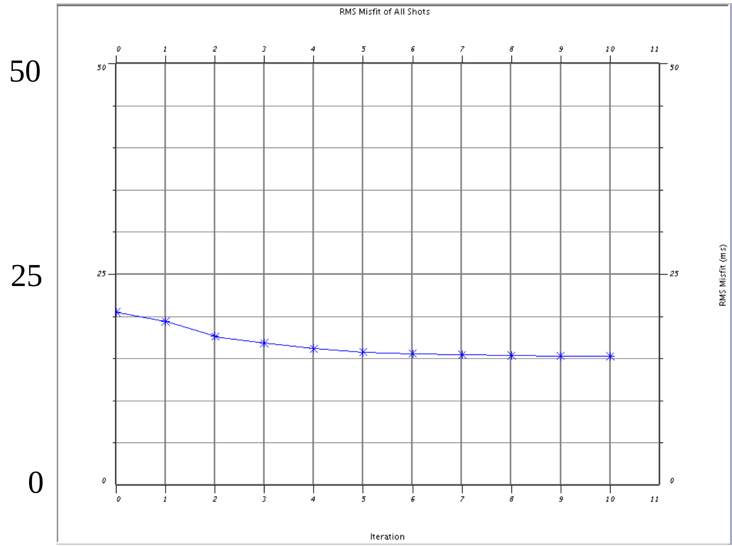

Figure 4.8: Total RMS misfit of observed traveltimes from seismic data and predicted traveltimes calculated from forward modeling. Software iterates until the discrepancy between both observed and calculated traveltimes, measured as the RMS error in inversion, has been reduced to a sufficiently small value comparable to the reciprocal errors

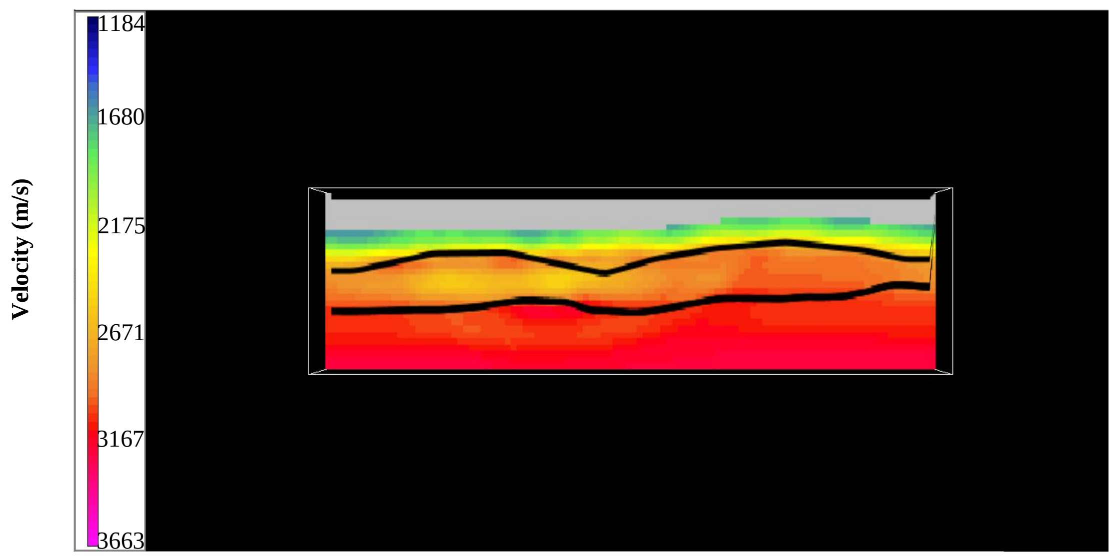

Figure 4.9: The final velocity model used to calculate the static solution for the survey. The upper black line is the calculated floating datum, the bottom one is the calculated intermediate datum

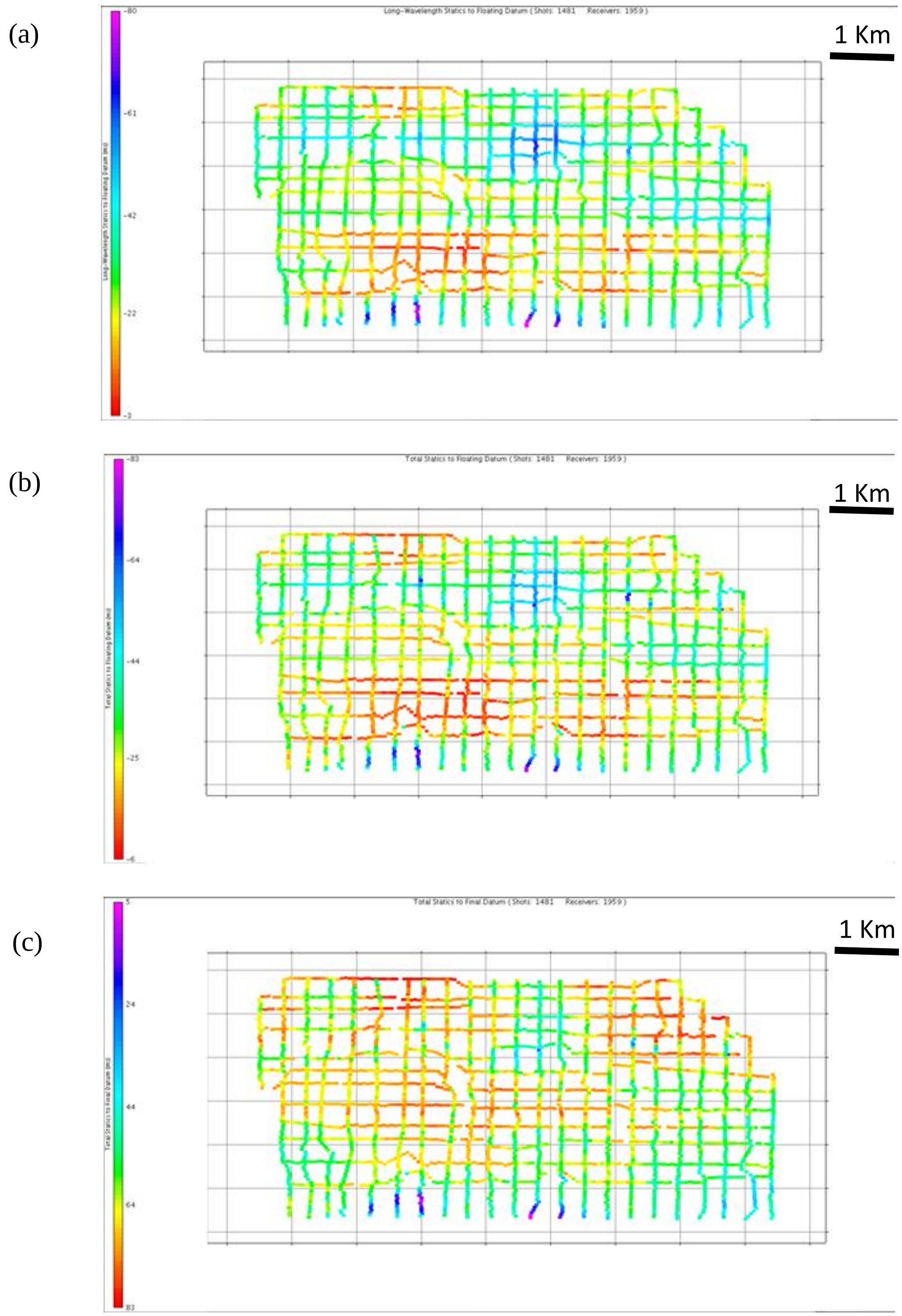

Figure 4.10: (a) Static solutions for long-wavelength statics to floating datum, (b) total statics to floating datum and (c) total statics to final datum

4.3.5 Gain recovery and surface consistent amplitude scaling

The amplitude recovery scheme applied was the spherical divergence correction, which is the amplitude loss due to the spreading of the spherical wavefront proportionately to $1/r^2$. Where r is the radius of the wavefront.

Following this is amplitude scaling, in which the factors that contribute to the trace amplitude are estimated statistically. Factors such as strength of the shot, coupling of the receivers, offset of traces, performance of the amplifier channel, etc. The traces from a particularly weak shot will tend to show lower amplitudes than normal shots. However, all traces recorded at a certain ground station can be higher amplitude because of better than average geophone coupling at that surface location.

For this data, the four components: shot, receiver, offset and CDP are decomposed in that order. But only shot a receiver terms were applied because offset and CDP are not surface consistent domains. Figure 4.11 shows the results after spherical divergence correction and the surface consistent amplitude scaling.

(a)

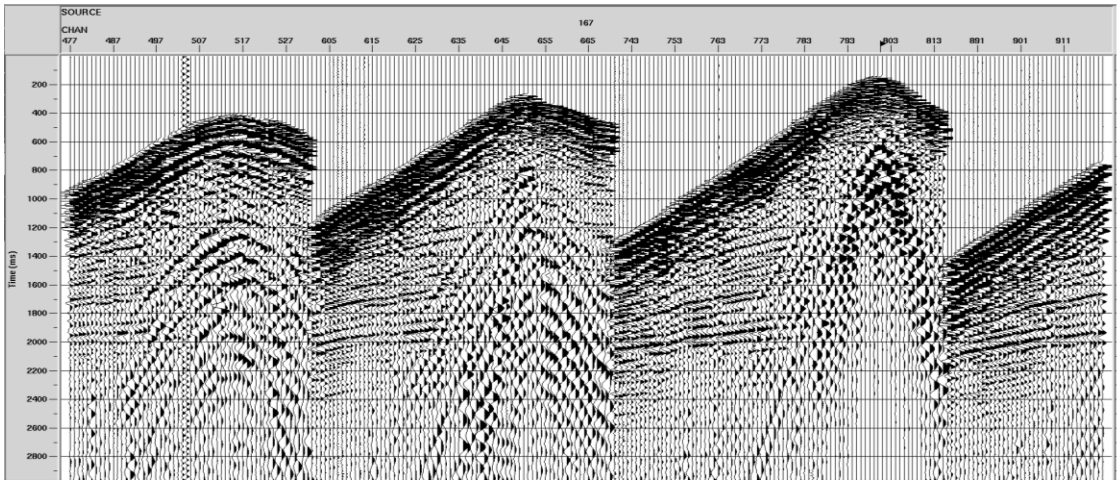

(b)

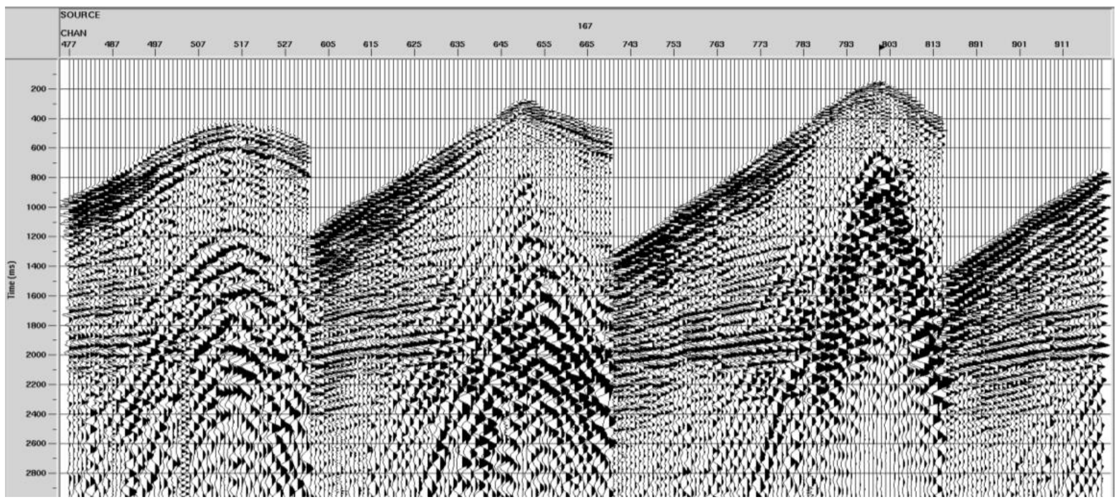

Figure 4.11: (a) Shot gather before applying spherical divergence correction and SCAC, and (b) after applying them. The amplitude of the deeper part of the section are balanced after compensating for spherical divergence and transmission losses.

4.3.6 Seismic noise attenuation

The first step in our noise attenuation workflow is surface wave noise attenuation. In order to accomplish this, the parameters needed are the apparent velocity of the noise wave to attenuate, high frequency selected and trace spacing. The apparent velocity was obtained by measuring the slope of the wave we are trying to remove at the shot domain. Figure 4.12 shows the velocity of the surface wave desired to be removed and this event has a frequency of 20 Hz.

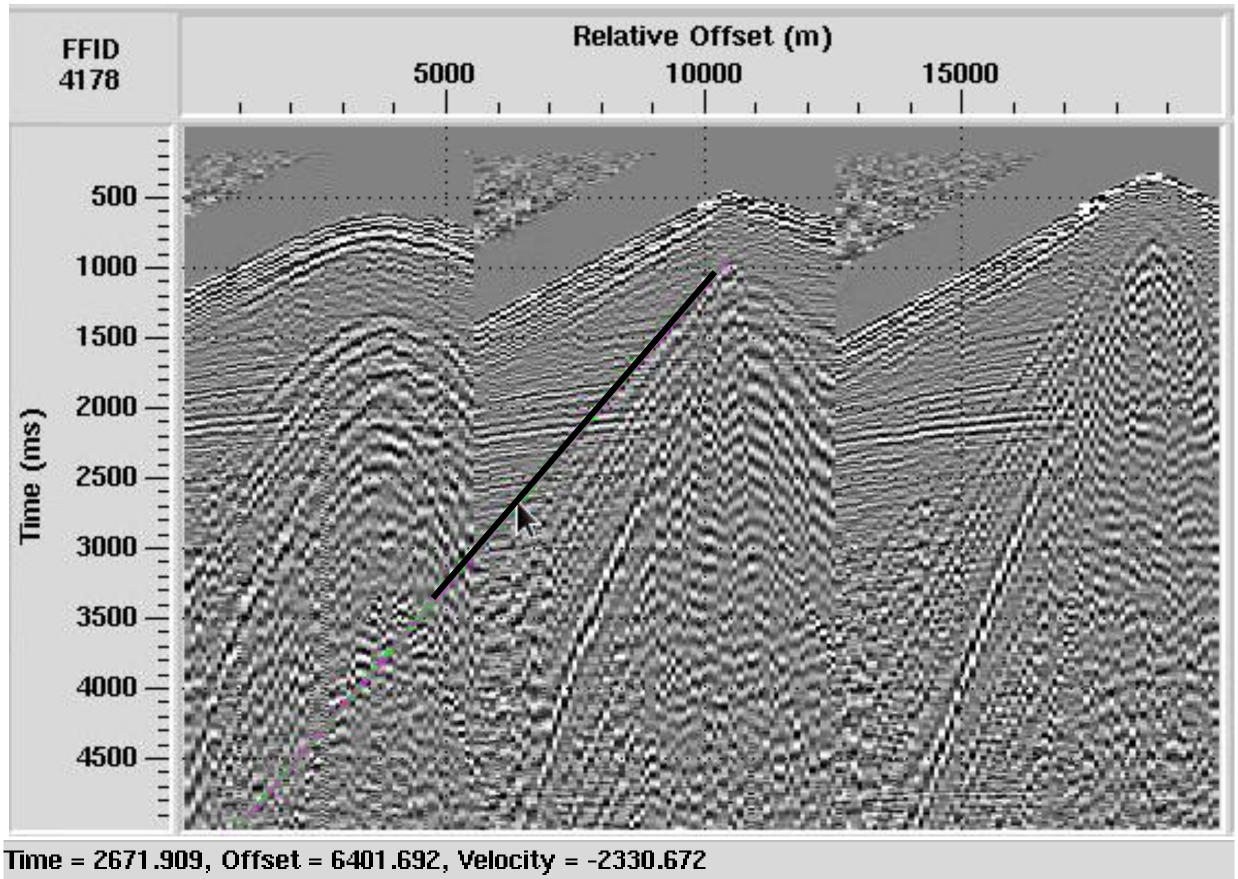

Figure 4.12: Surface wave apparent velocity is measured on an example shot gather. The apparent velocity for this example is approximately 2330 m/s

Finally, the trace spacing is obtained by calculating the average trace spacing for each panel from the offset values in the trace headers. Figure 4.13 shows the difference of a shot gather before and after attenuating the surface wave energy.

(a)

(b)

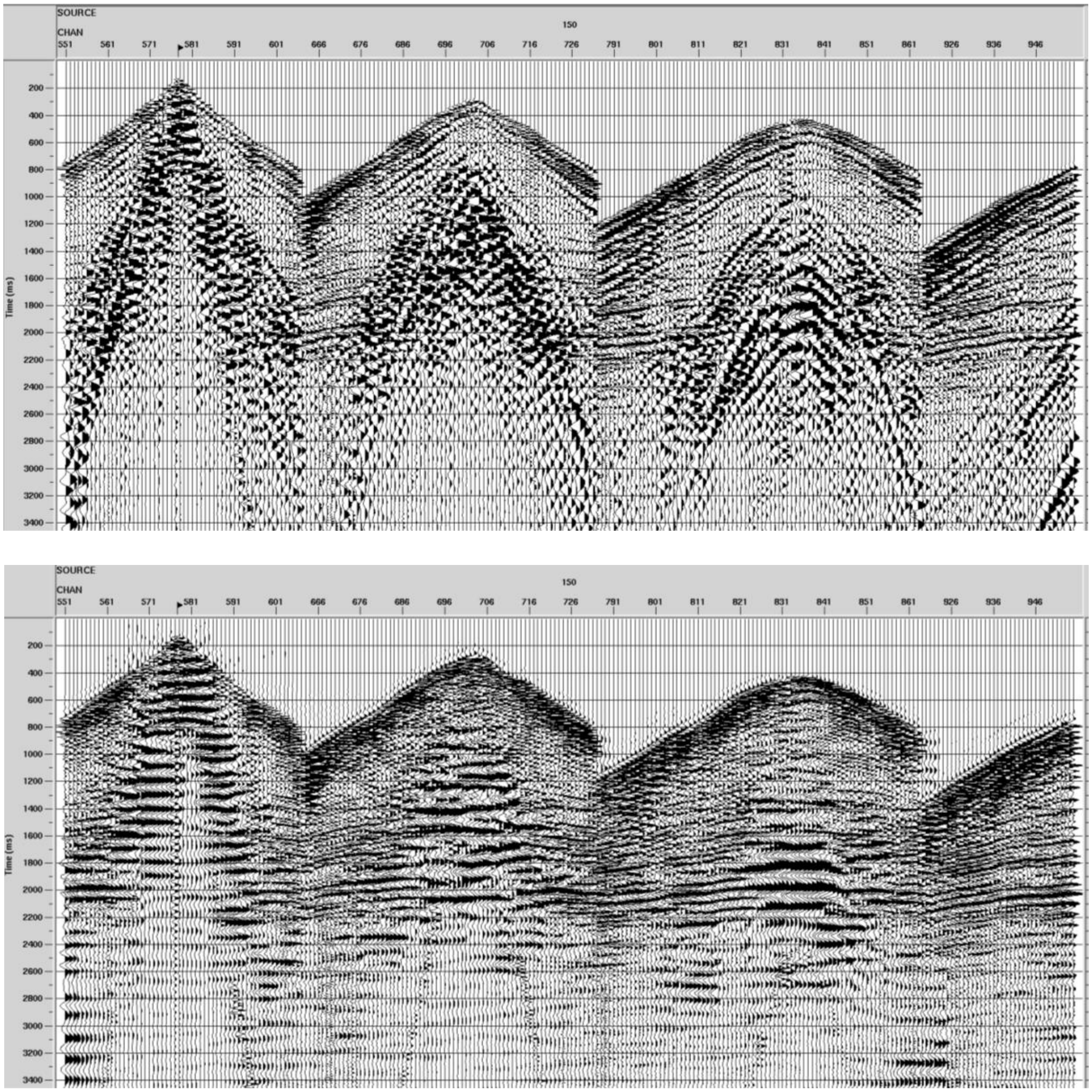

Figure 4.13: (a) Shot gather before removing the surface wave and (b) after removing it. Everything within the velocity range (-2300 – 2300 m/s) is attenuated

Next, I applied coherent noise attenuation. For this process, we need the frequency-velocity pairs that envelop the coherent noise we are trying to remove. These pairs could be obtained by looking at the data at the f-x domain as shown in Figure 4.14. Moreover, regular trace spacing was assumed. Trace spacing used was 25m.

(a) (b)

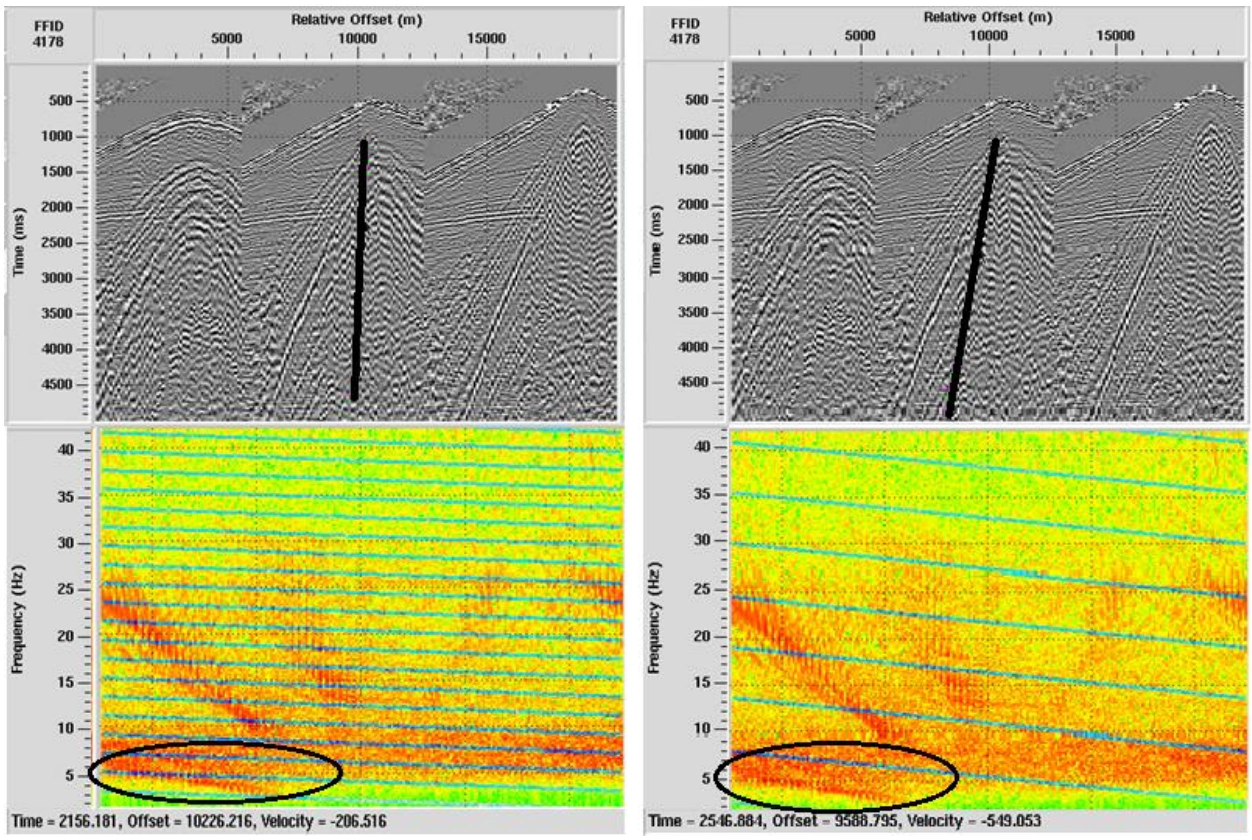

(c) (d)

Figure 4.14: (a) and (b) are shot gathers. (c) and (d) are the f-x domain display of the shot gathers in (a) and (b). This tool allows us to see the possible frequencies (blue lines in the f-x domain) that pair with velocity measured in the shot gathers in (a) and (b). The circled area represents the coherent noise we want to remove. From the shot gather (a) and the f-x domain (c), we get the first frequency- velocity pair: 2-200. The other pair we get it from the other shot gather (b) and f-x domain (d): 6-540. These two pairs envelop the noise wanted to be removed.

Figure 4.15 shows an example of shot gather before and after applying the coherent noise attenuation, and the noise removed from the section.

(a)

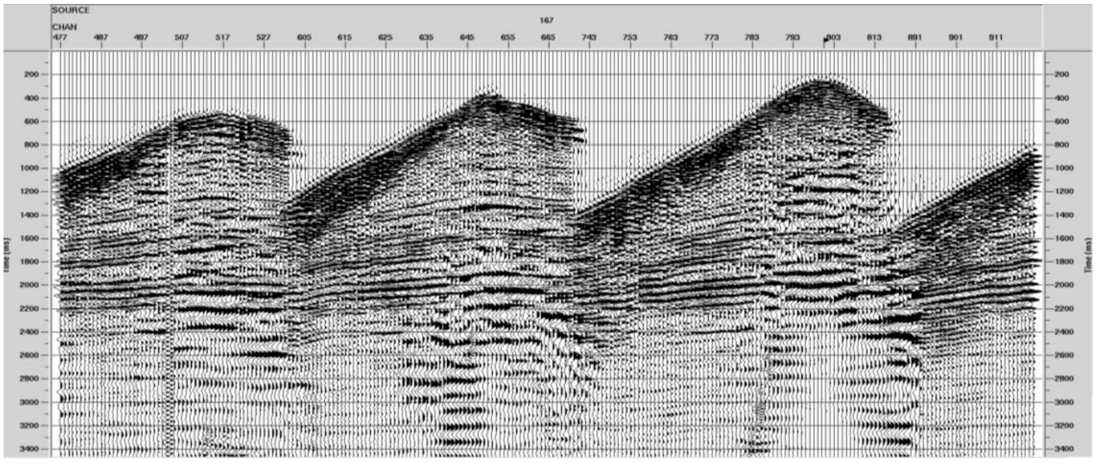

(b)

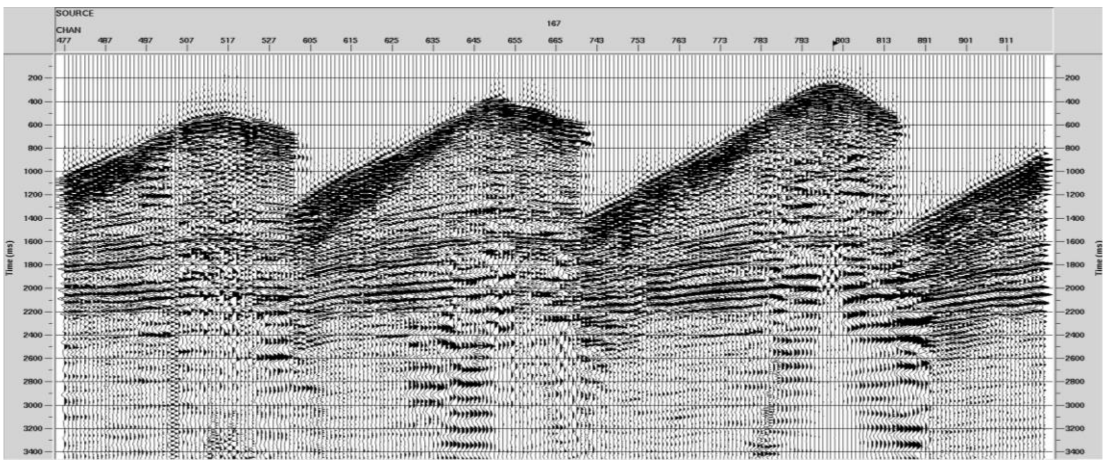

(c)

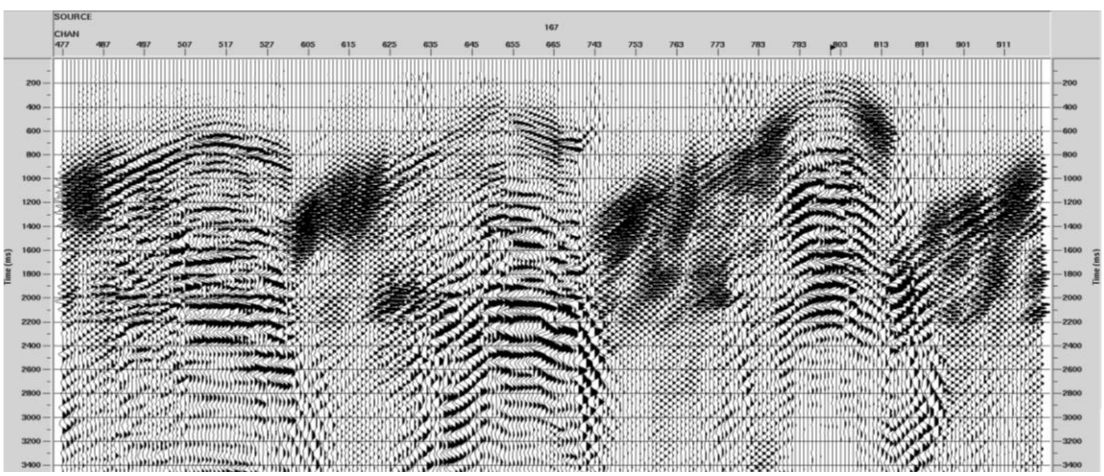

Figure 4.15: (a) Before CNA, (b) after CNA and (c) the noise removed

The final step in noise attenuation was to remove the low frequency noise in the middle and deep sections. This was easily achieved by applying a bandpass filter. The type of filter used is Ormsby bandpass, and the values were: 8 - 12.5 - 350 - 400 Hz. These values match with the frequency content of the data. Figure 4.16 shows the effect of applying the bandpass filter.

(a)

(b)

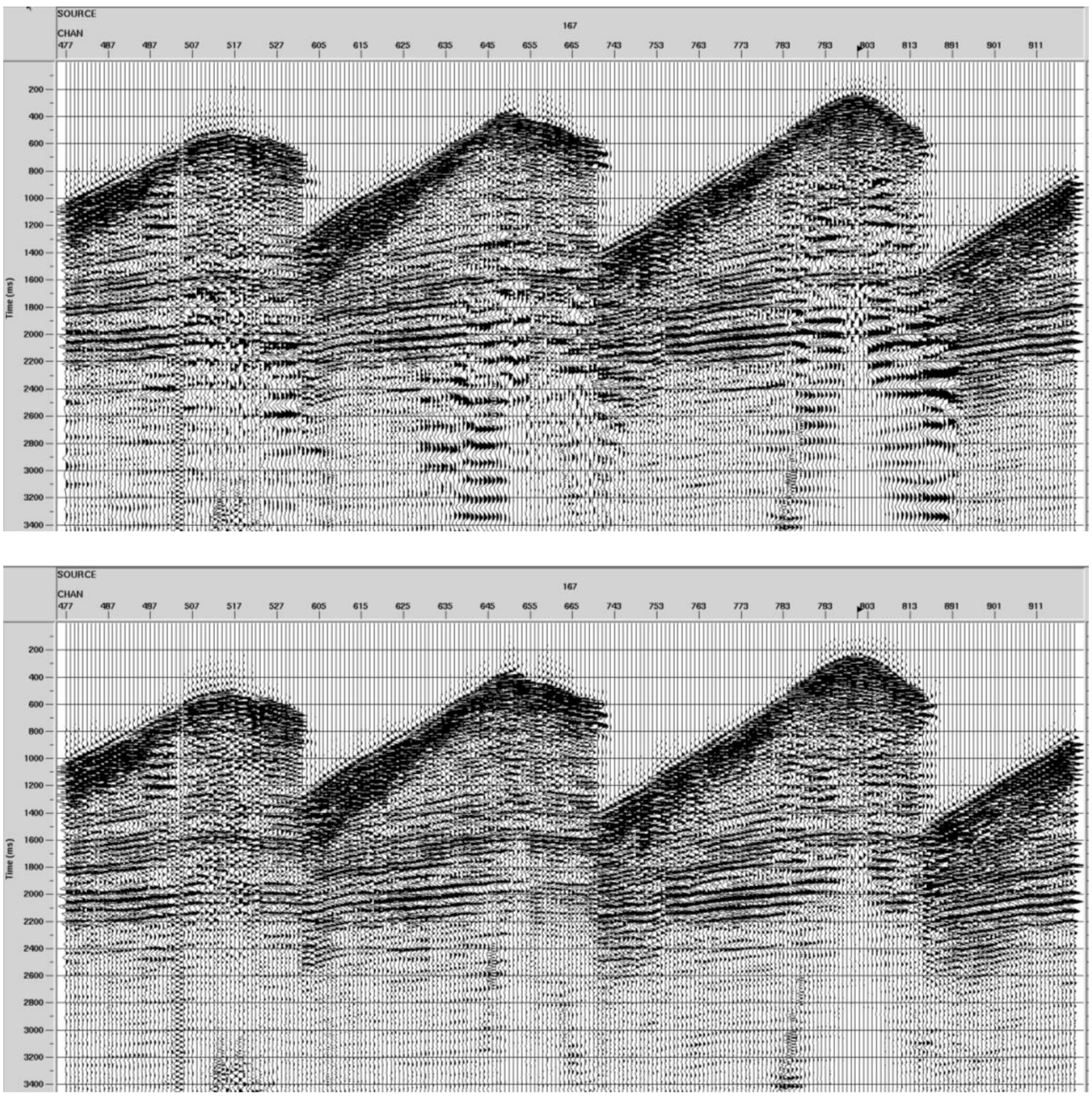

Figure 4.16: (a) Before applying bandpass filter and (b) after applying it. Data looks more coherent after removing the low frequency data.

Events start to appear after applying seismic noise attenuation as shown in one of the stacks in the inline direction in Figure 4.17.

(a)

(b)

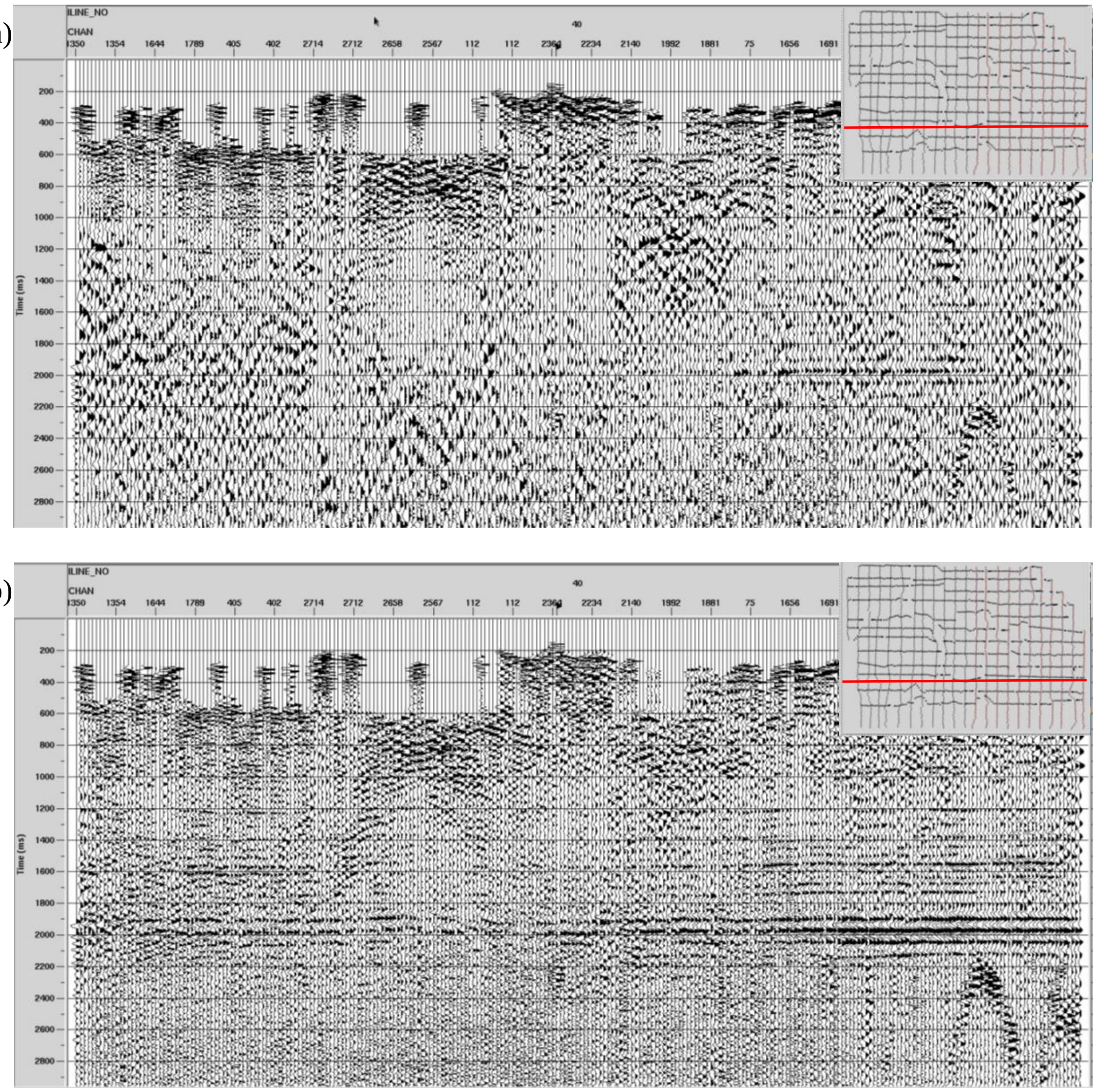

Figure 4.17: (a) Seismic stack in the inline direction (W-E) before applying noise attenuation workflow, and (b) after applying noise attenuation workflow

4.3.7 Surface consistent deconvolution

Predictive deconvolution removes the effects of multiples by using the later portions of the autocorrelation. This method predicts the arrival of a multiple event from the knowledge of earlier events.

The parameters needed for this step are the deconvolution operator length and white noise level. Different deconvolution operator lengths were tested: 50 ms, 90 ms and 120 ms, and different white noise level were tested as well: 0.1%, 0.5% and 1%. Since the effect of the above parameters was hard to observe in both gathers and amplitude spectra, the default parameters were used for deconvolution operator length (120 ms) and white noise level (0.1%). Figure 4.18 and 4.19 show the effect of the minimum phase predictive deconvolution in a shot gather and amplitude spectra, respectively.

(a)

(b)

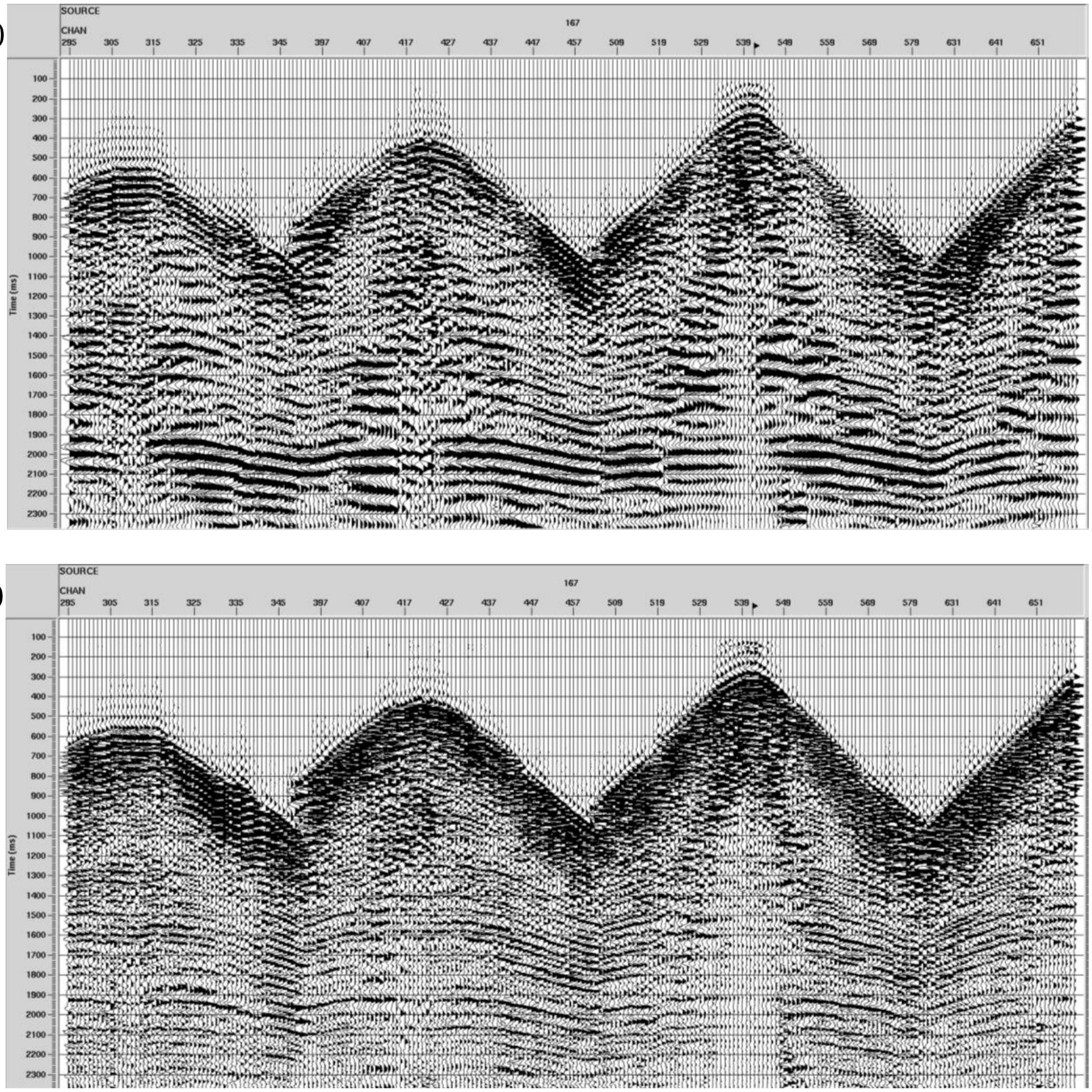

Figure 4.18: (a) Shot gather after noise attenuation and (b) after applying deconvolution.

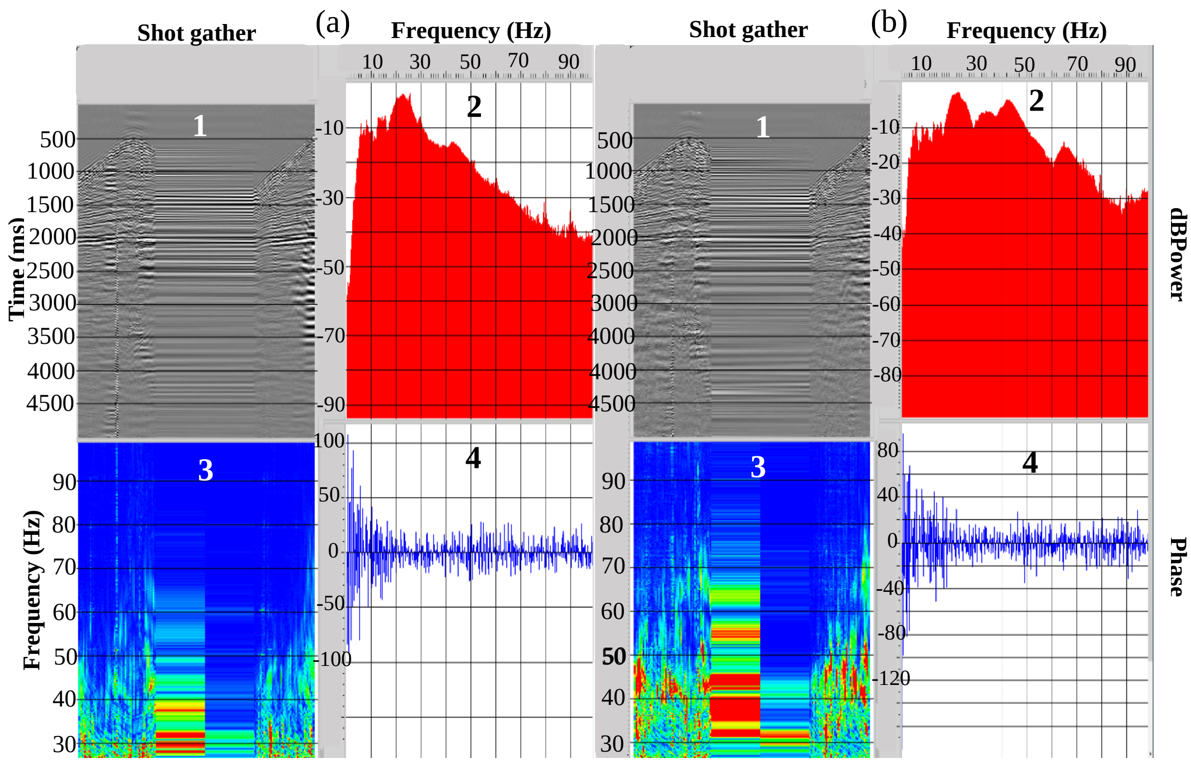

Figure 4.19: (a1) and (b1) are shot gathers. (a2) and (b2) are the amplitude spectra. (a3) and (b3) are the frequency vs offset plots. (a4) and (b4) are the phase vs frequency plots. (a) Spectral analysis of one shot gather before applying deconvolution and (b) after applying it. The spectrum is flatter across the bandwidth of the data

4.3.7 First pass of velocity analysis

Before picking NMO velocities, CDP supergathers were created for velocity analysis. Three CDPs were combined in the inline direction, and 5 CDPs in the crossline direction as shown in Figure 4.20. the first pass of velocity analysis was carried out using conventional semblance, supergathers, and percentage velocity stacked panels. The method involved adjusting the RMS velocity until primary events on the supergather were flattened as guided by the semblance plot. Event energy maximization was reviewed using the stack panels and the interval velocities were checked for geologic plausibility. An example of ProMax interactive velocity analysis display is shown in Figure 4.21. Velocities were analyzed on a ½ km by ½ km grid.

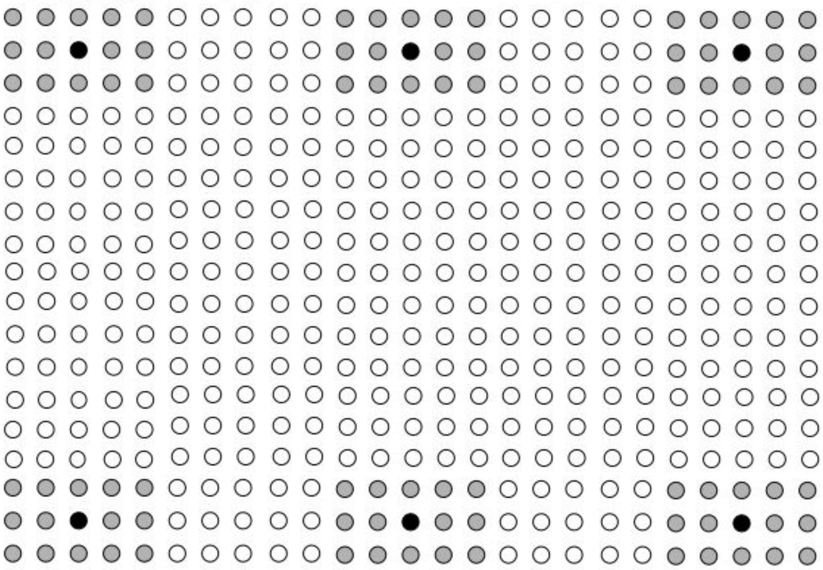

Figure 4.20: 3D supergather used before the velocity analysis. Inline increment is 10. Crossline increment is 15

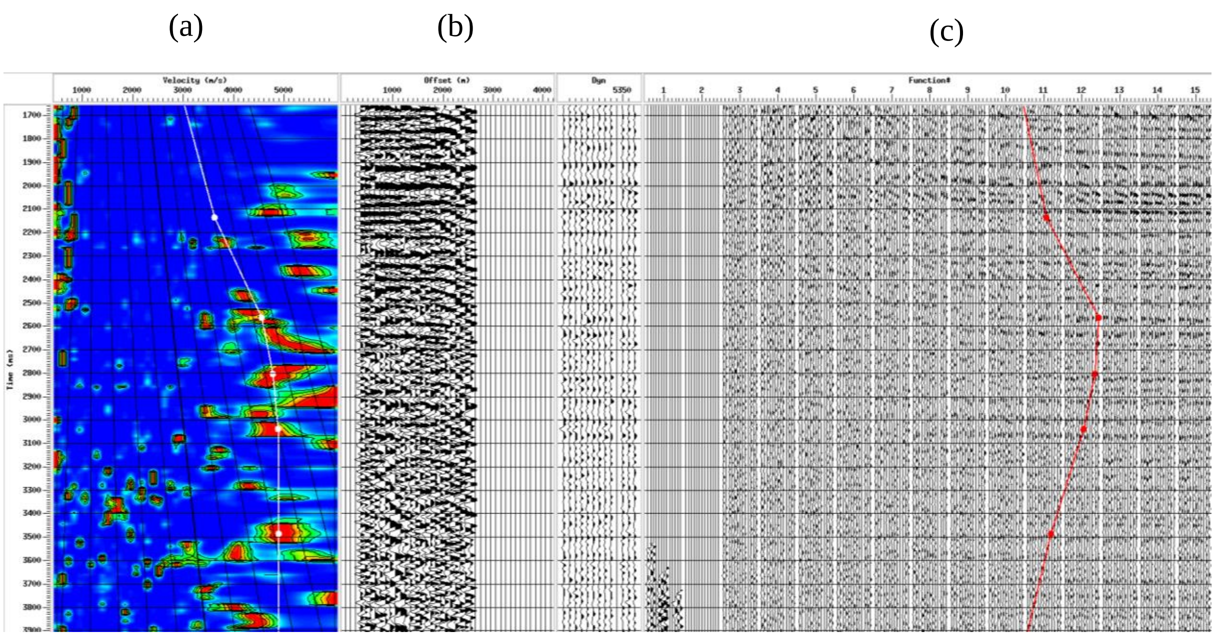

Figure 4.21: Example of velocity analysis in Promax interactive velocity analysis tool. (a) Semblance window, (b) supergather and (c) stack panels.

4.3.9 First pass of residual statics

Certain steps needed to be completed before calculating and applying the residual statics. Firstly, data should be sorted into CDPs and NMO is applied. In addition, a bandpass filter of 8 - 12.5 - 40 - 50 Hz was applied to clean the data. Next, one or two horizons should be picked to be used in the residual static calculation. Finally, the residual statics were applied.

Velocities from the previous step was used to correct for the normal moveout. And for the horizon picking, two were picked to avoid biasing. These two horizons are shown in Figure 4.22.

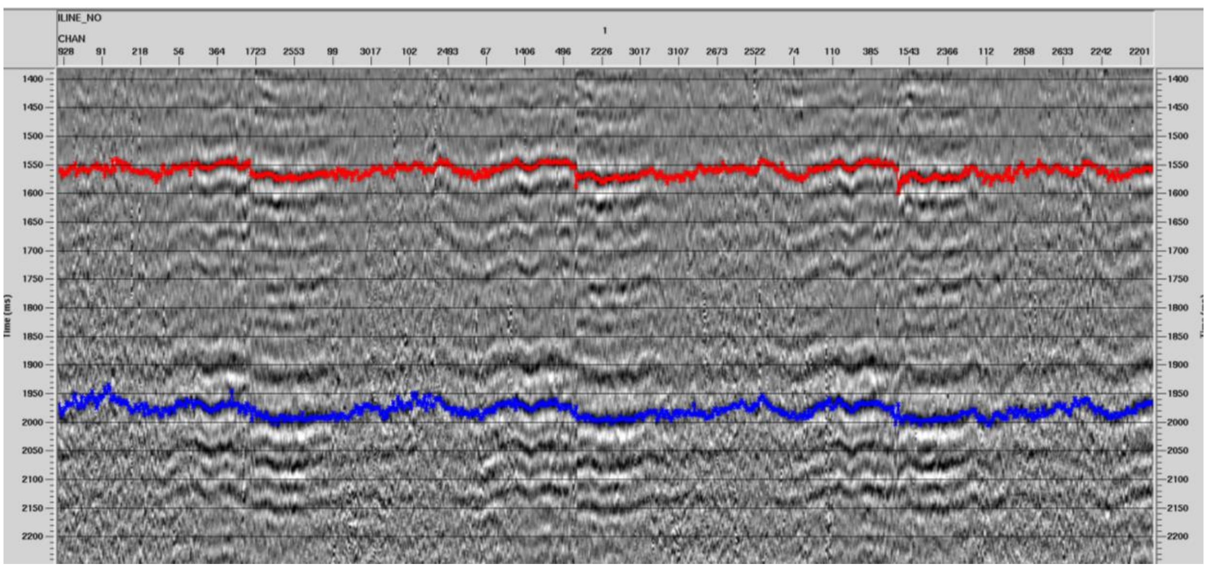

Figure 4.22: Two autocorrelation horizons are picked for the residual statics to avoid biasing

The aperture used for the horizon picking was 11 CDP traces since there are no steeply dipping events, and traces were summed along the horizon to form the model trace for correlation. The time gate width was 100 ms which is about twice the maximum residual statics expected. Both horizons do not extend across the entire dataset. There are small areas in which horizons were not picked due to the difficulty of interpretation, so these CDPs were not included in a horizon for residual statics calculations.

The residual static solution in areas of overlapping windows were averaged and a 10 trace overlap was used to provide a smooth transition between static solutions.

The input for the residual static calculations are the NMO corrected CDP gathers, and the autostatics horizons were used as well. For the maximum static allowed per iteration, values started out low in order to keep the solution from immediately diverging. The maximum number of iterations was 10. Figure 4.23 shows an inline example of the result of applying the residual statics.

(a)
(b)

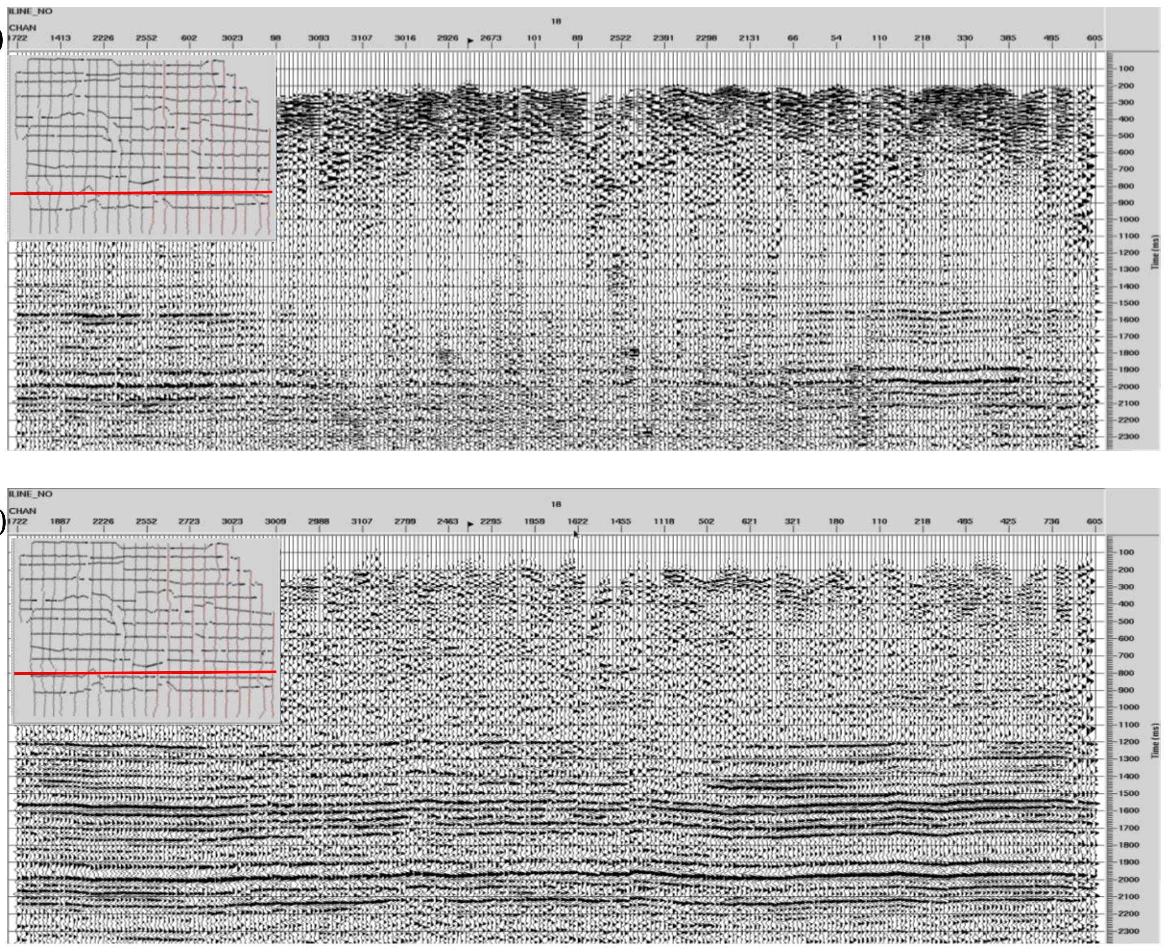

Figure 4.23: Inline example shows the effect of first pass of residual statics. (a) Before applying residual statics, (b) after applying residual statics

4.3.10 Second pass of velocity analysis and residual statics

Velocity analysis was repeated after application of the residual static correction as the static solution improved the alignment of reflection energy, enabling better estimation of the stacking velocities. The velocity field is shown in Figure 4.24.

Also, a second pass of residual statics was calculated using the refined stacking velocity field. Minor improvement of seismic events was achieved as velocities picked in the first pass were accurately estimated. Figure 4.25 shows a comparison between before the second pass of velocity analysis and residual statics and after it, in the crossline direction.

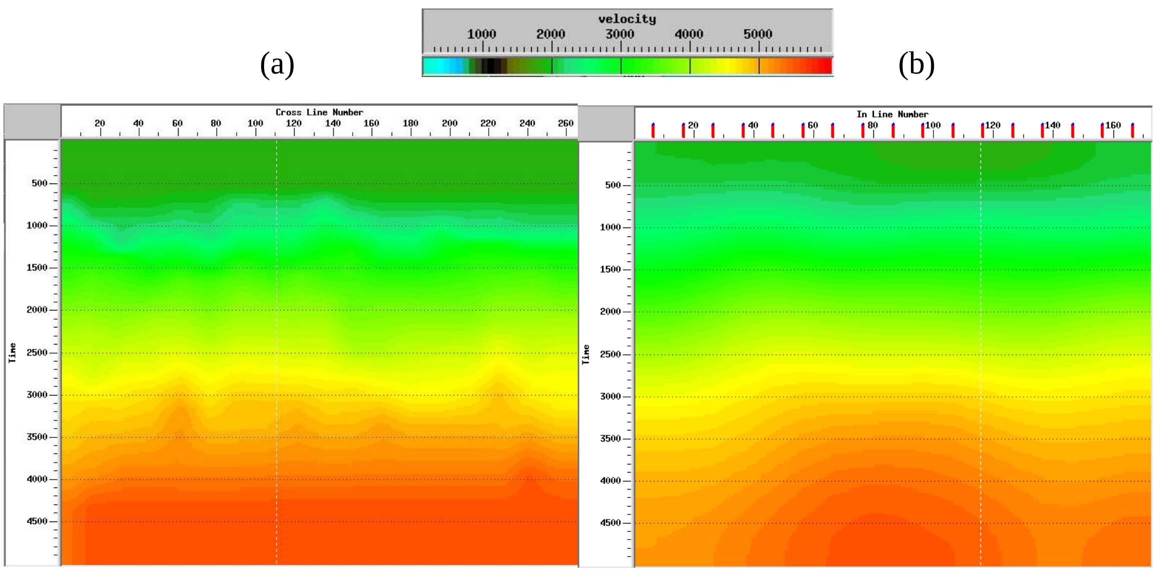

Figure 4.24: Velocity model after completing the second pass of velocity analysis. (a) velocity field in the inline direction and (b) the velocity field in the crossline direction. Both lines pass through the middle of the survey.

4.3.11 Post-stack time migration

Before migrating the stacked data, F-X deconvolution was applied to remove some of the random noise. F-X deconvolution applies a Fourier transform to each trace in the stacked data and applies a prediction filter in distance for each frequency in a specified range. The parameters used for F-X deconvolution are 10 traces for the horizontal window length, 5 for the number of filter samples and the filter frequency starts at 1 Hz and ends at 250 Hz. The result would be a stack with less random noise than the input data. Figure 4.26 shows the effect of F-X deconvolution on the stacked data.

(a)

(b)

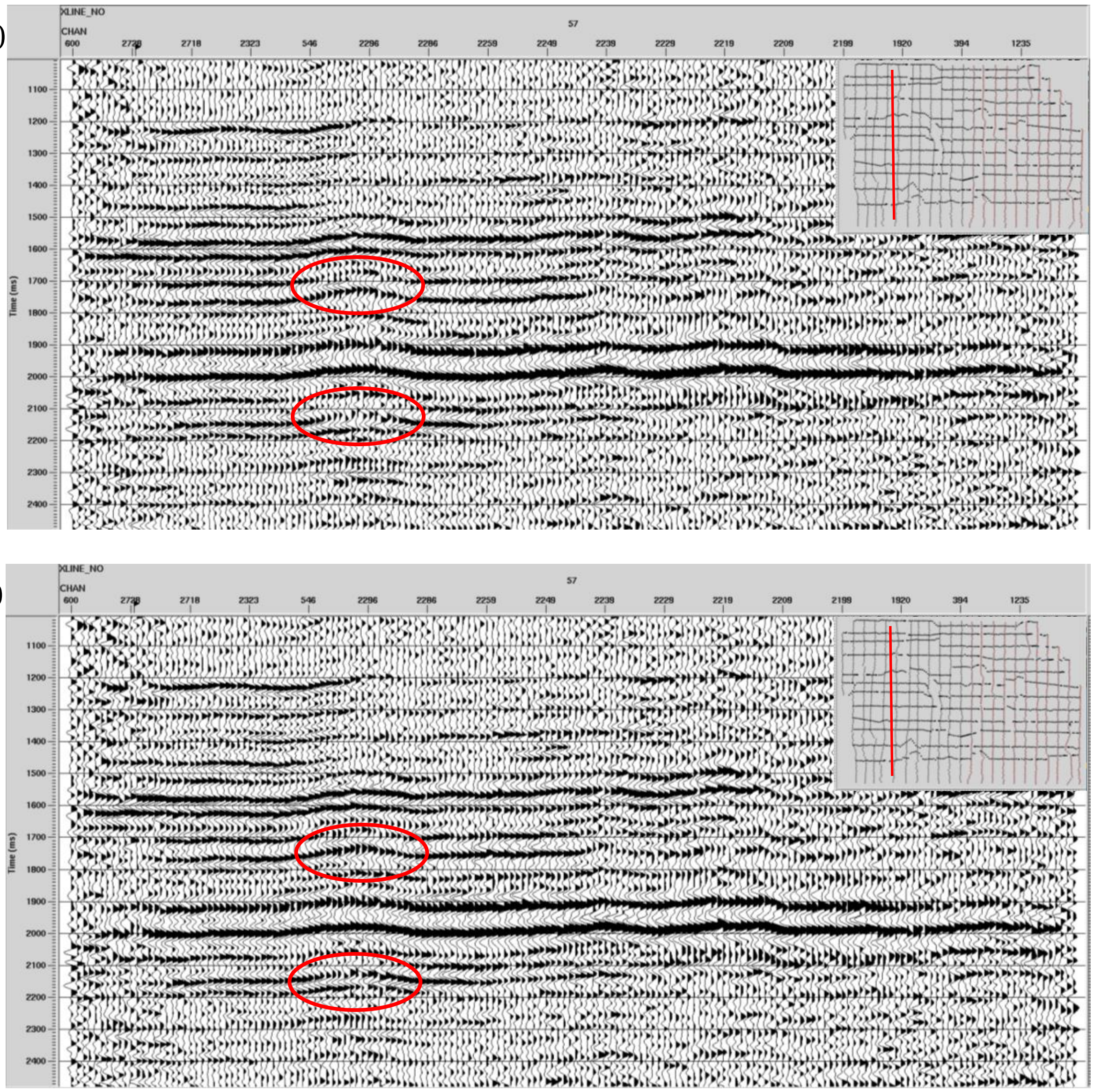

Figure 4.25: Comparison between the first and second pass of velocity analysis and residual statics in the crossline direction.

In order to migrate, data should be padded in both inline and crossline directions to account for the migration aperture and allow traces to be relocated to their correct locations. The padded dead traces produce a full 3D cube of stacked traces. This cube is needed to perform the migration.

(a)

(b)

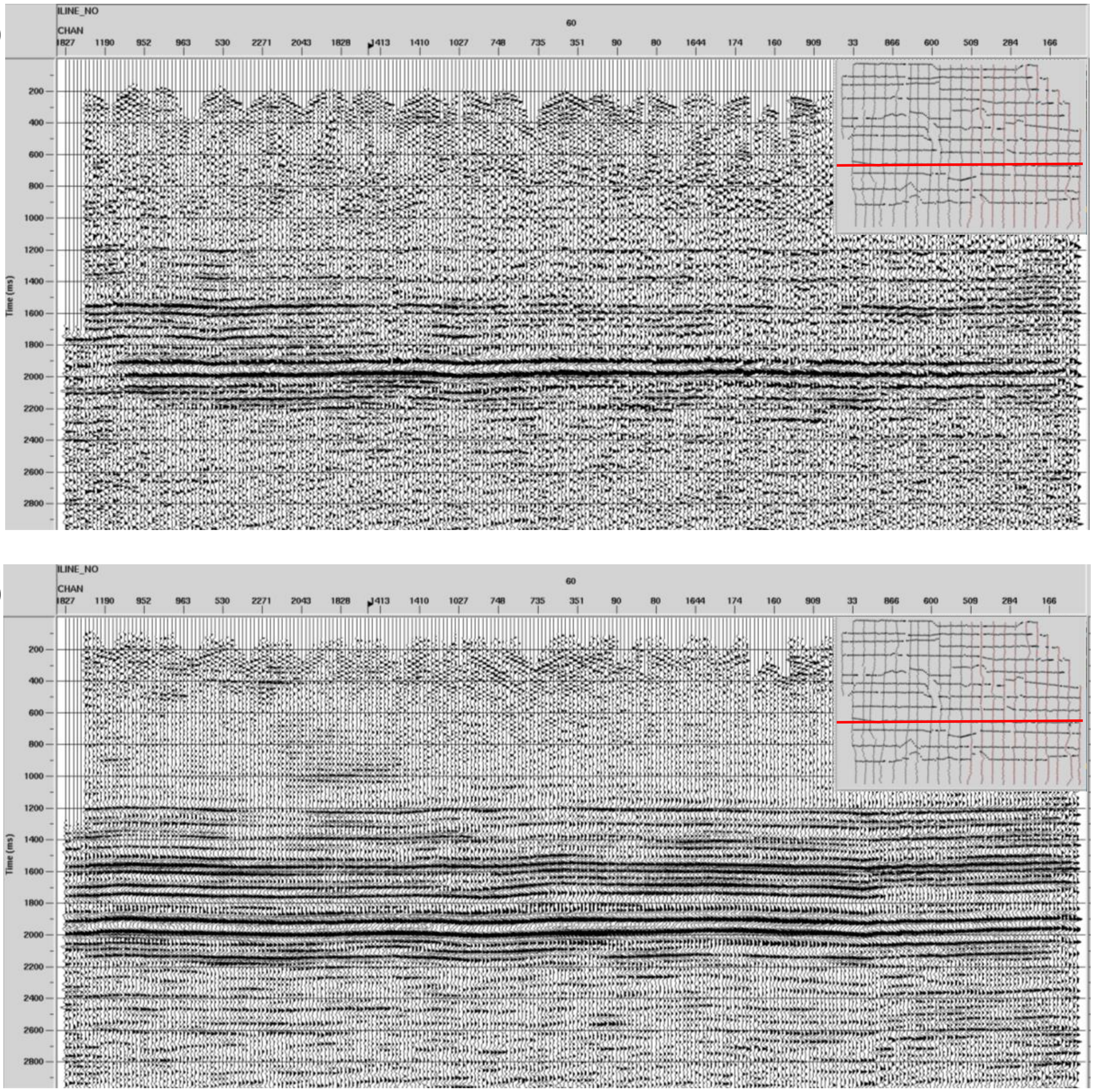

Figure 4.26: (a) A stack in the inline direction before applying F-X deconvolution and (b) after applying F-X deconvolution

Migration performed is a poststack 3D time migration using explicit finite-difference extrapolators. Figures 4.27 and 4.28 show results of second pass of residual statics, F-X deconvolution and post-stack time migration in both inline and crossline directions, respectively.

(a)

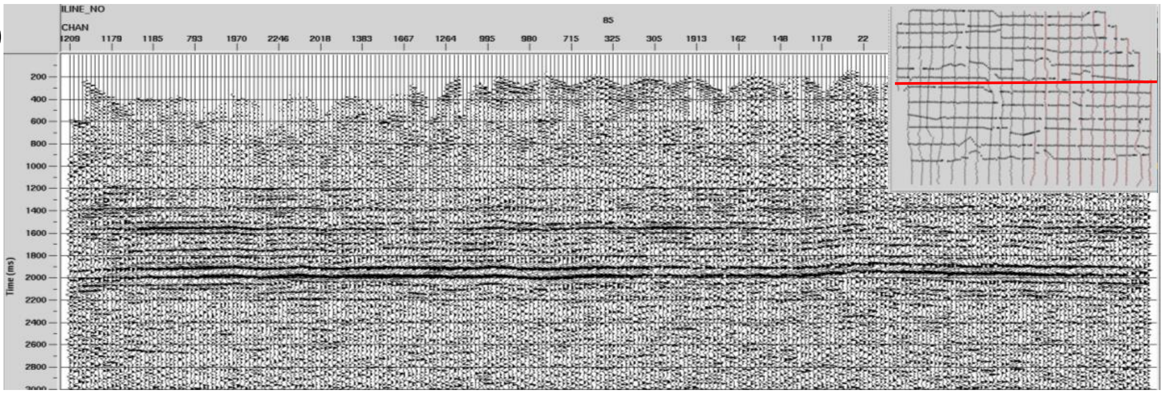

(b)

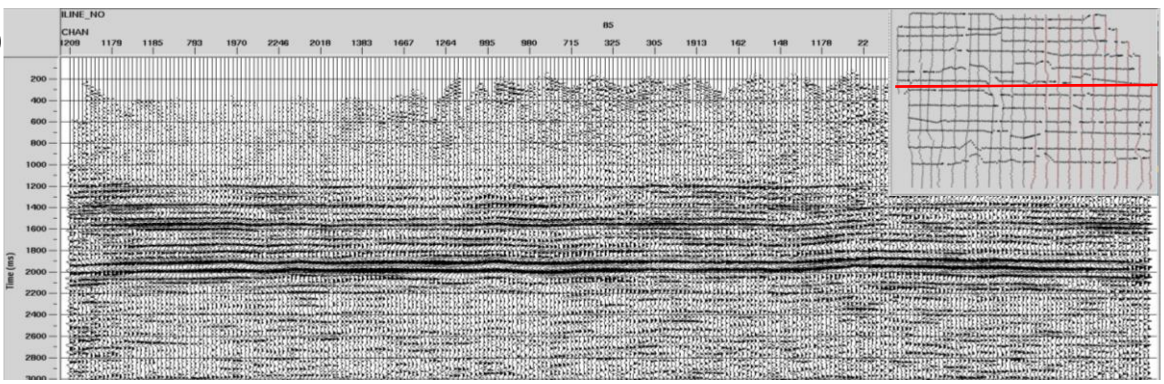

(c)

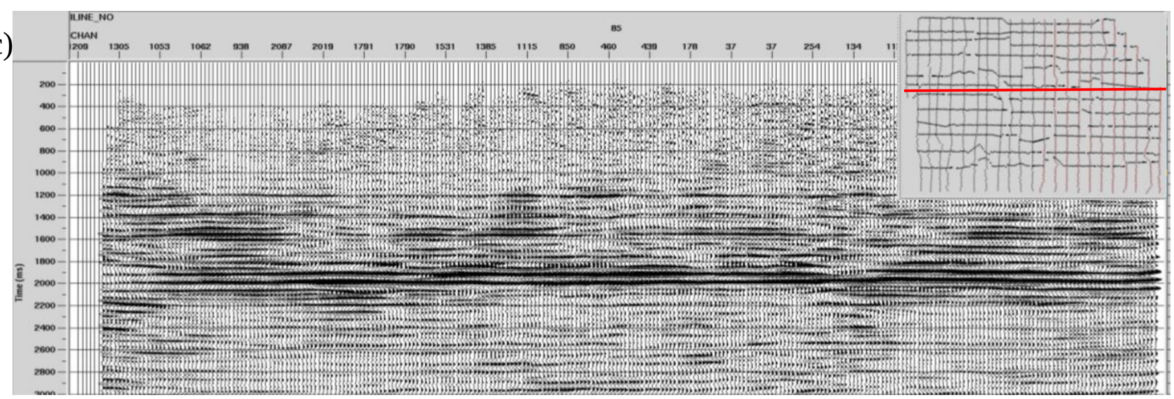

Figure 4.27: A comparison between (a) a second pass of residual statics, (b) F-X deconvolution and (c) post-stack time migration in the inline direction. The migration successfully improved the image of the deeper part of the section

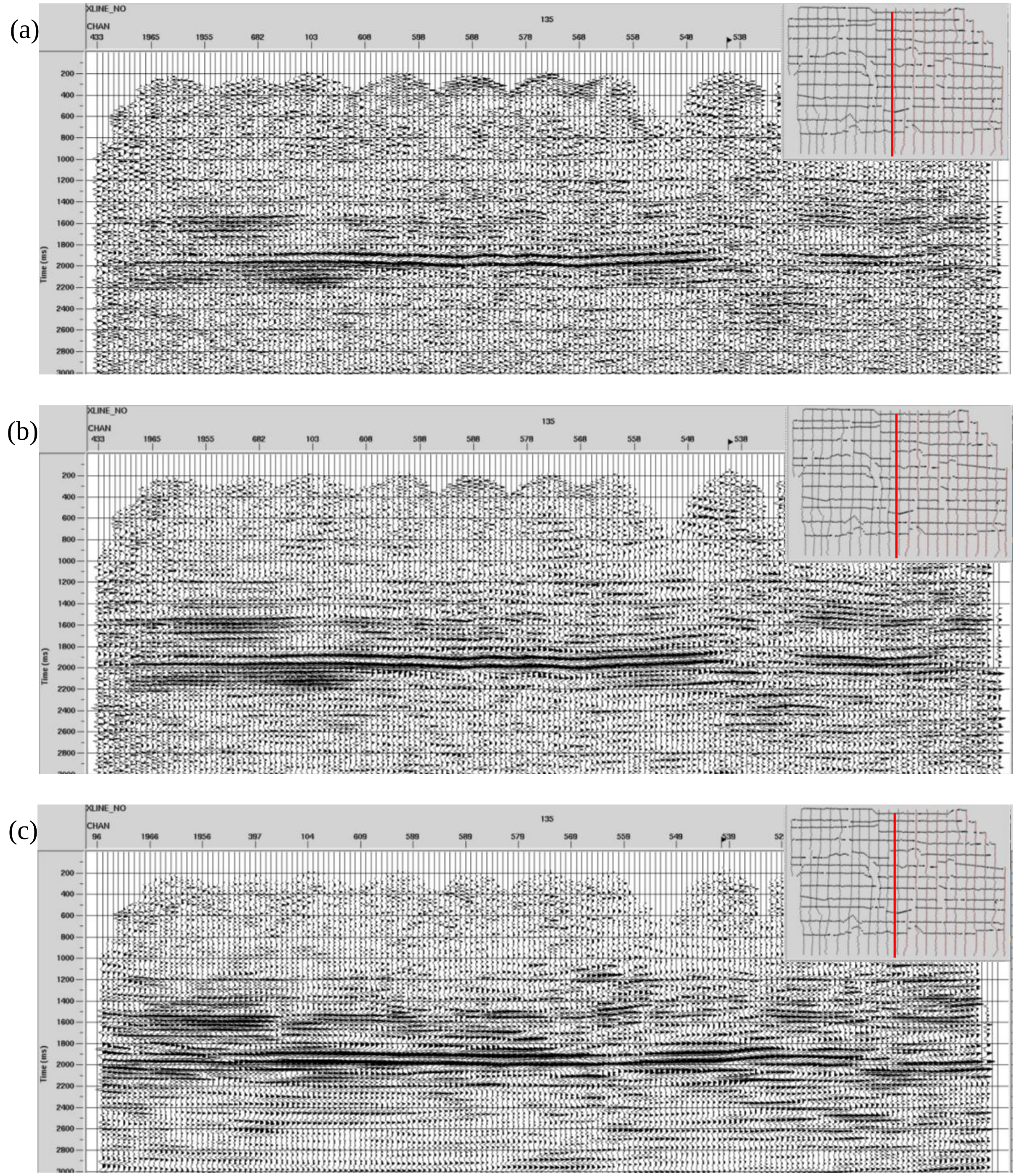

Figure 4.28: A comparison between (a) a second pass of residual statics, (b) F-X deconvolution and (c) post-stack time migration in the crossline direction. The migration successfully imaged the deeper part in the crossline section, similar to the inline section

Figures 4.29 and 4.30 show the results of the migration before and after signal enhancement zoomed to 2500 ms in inline and crossline directions, respectively.

(a)
(b)
(c)

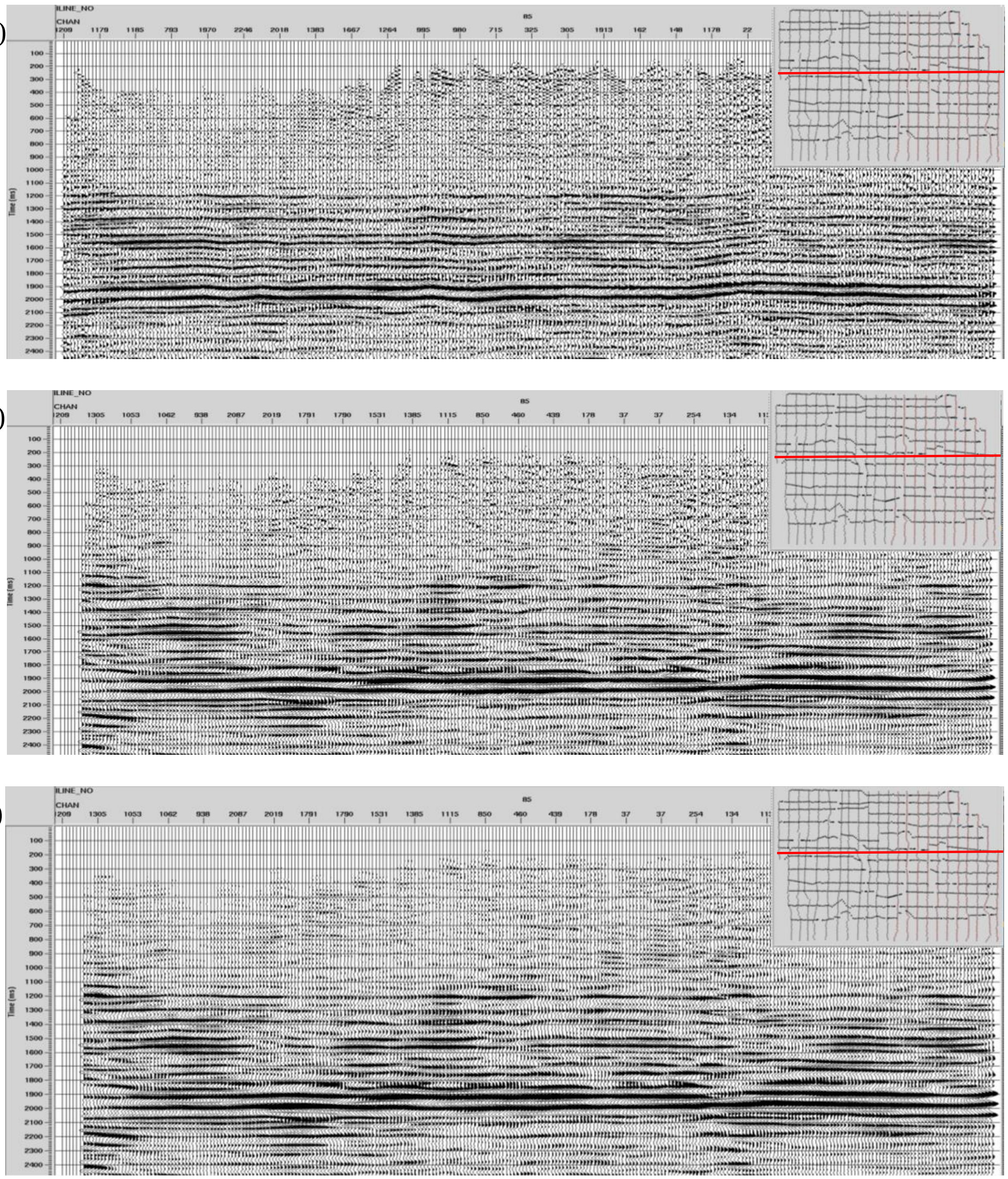

Figure 4.29: (a) Second pass of residual statics with F-X deconvolution applied, (b) post stack time migration, (c) and some signal enhancement applied. All sections are in the inline direction

(a)
(b)
(c)

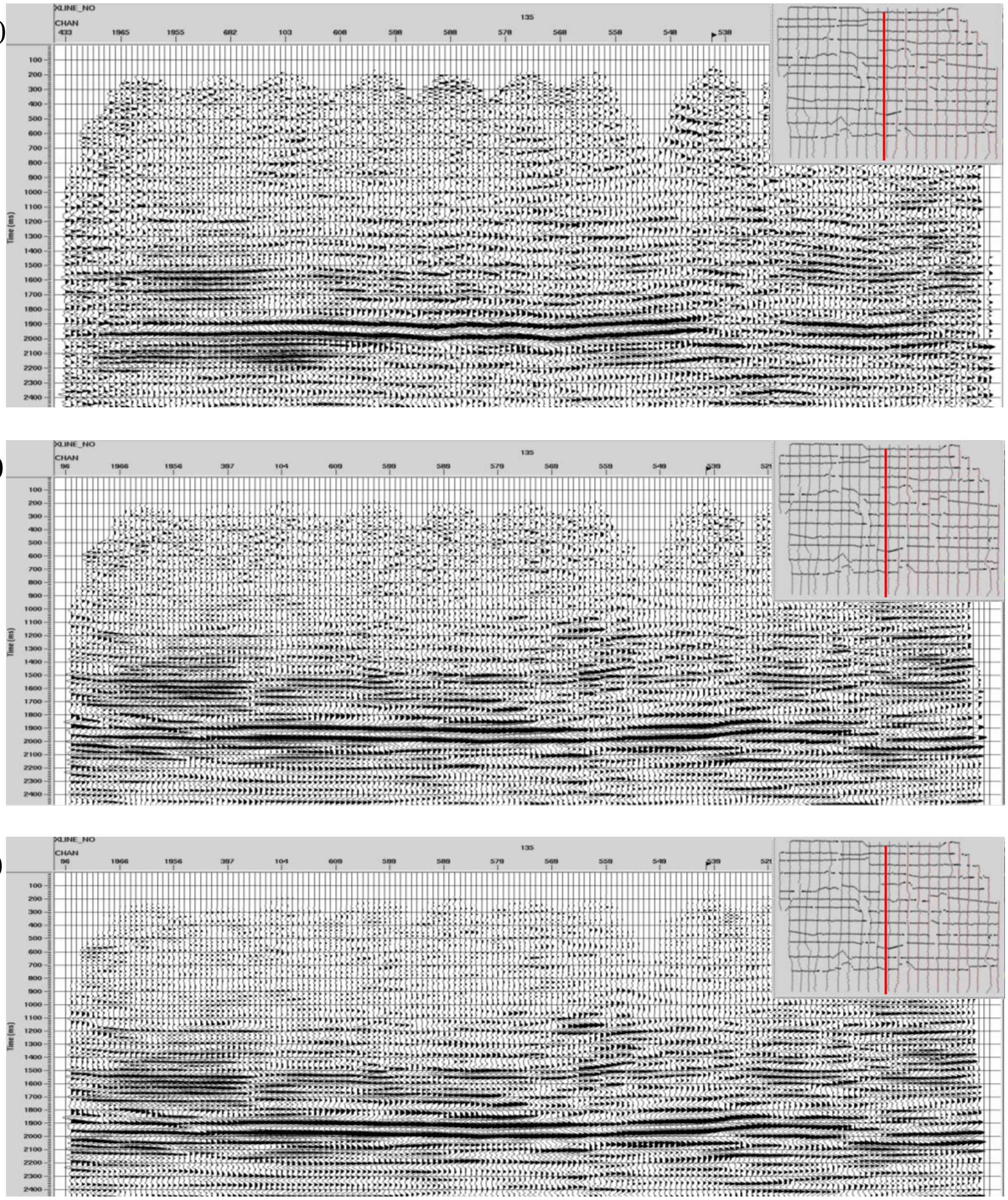

Figure 4.30: (a) Second pass of residual statics with F-X deconvolution applied, (b) post stack time migration, and (c) some signal enhancement applied to it. All sections are in the crossline direction

Finally, Figure 4.31 shows the 3D processed volume of P-P data.

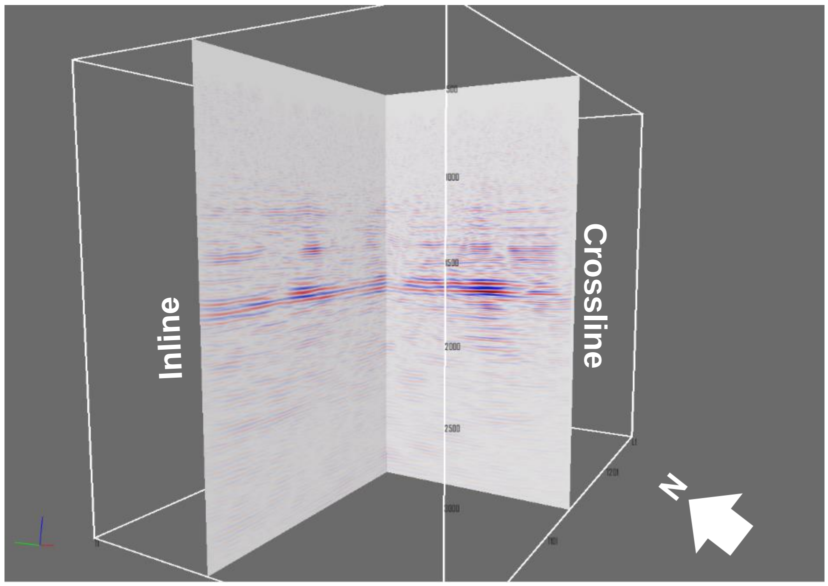

Figure 4.31: P-P migrated volume

Chapter Five: **PROCESSING 3C3D BIGSTONE P-S DATA**

5.1 Processing Workflow

The processing of P-S data is similar to the processing of P-P data except for the additional steps discussed in chapter 2. In this chapter, I reviewed the processing steps in the P-S workflow with the emphasize on those that are different from what was presented in chapter 4 when we processed the P-P data. Table 5.1 summarizes the processing workflow for P-S data.

Table 5.1: Processing workflow for P-S data

1	Geometry	10	First Pass of Residual Statics
2	Binning	11	Second Pass of Velocity Analysis
3	Rotation of Horizontal Components	12	Second Pass of Residual Statics
4	Radial Filter	13	ACP and CCP Binning
5	Elevation / Static Correction	14	ACP and CCP Stack
6	Gain Recovery / SCAC	15	NMO
7	Seismic Noise Attenuation	16	Stack
8	Surface Consistent Deconvolution	17	PP – PS Event Registration
9	First Pass of Velocity Analysis	18	Post-stack Time Migration

5.2 Processing workflow steps

5.2.1 Azimuthal Rotation of Horizontal Components

This step is to rotate the horizontal components H1 and H2 only in order to obtain the radial (R) and transverse (T) components. First, the angle ϴ between H1 component azimuth and the source-receiver azimuth should be known. The angle ϴ was calculated after we selected the H1 orientation to be 18 degrees that is consistent with the observer's report and the magnetic declination of the area at the survey time.

After that, the angle ϴ was calculated by subtracting the original azimuth from the surface azimuth. Then, the radial and transverse components were calculated using the equations 2.1 and 2.2 in chapter 2. Figure 5.1 shows an example comparison between H1, H2, radial and transverse components. One possible reason why we may observe reflections in the transverse component is due to the fractures in the subsurface that represent horizontally transverse isotropy (HTI). This results in splitting the shear wave of P-S data (Liu, 2008).

5.2.2 Binning

Binning at this early stage of processing is the same as the binning for P-P data which is the conventional CMP binning. Until completing the second pass of residuals step in processing flow, we took the best data and stacked it based on both ACP and CCP binning.

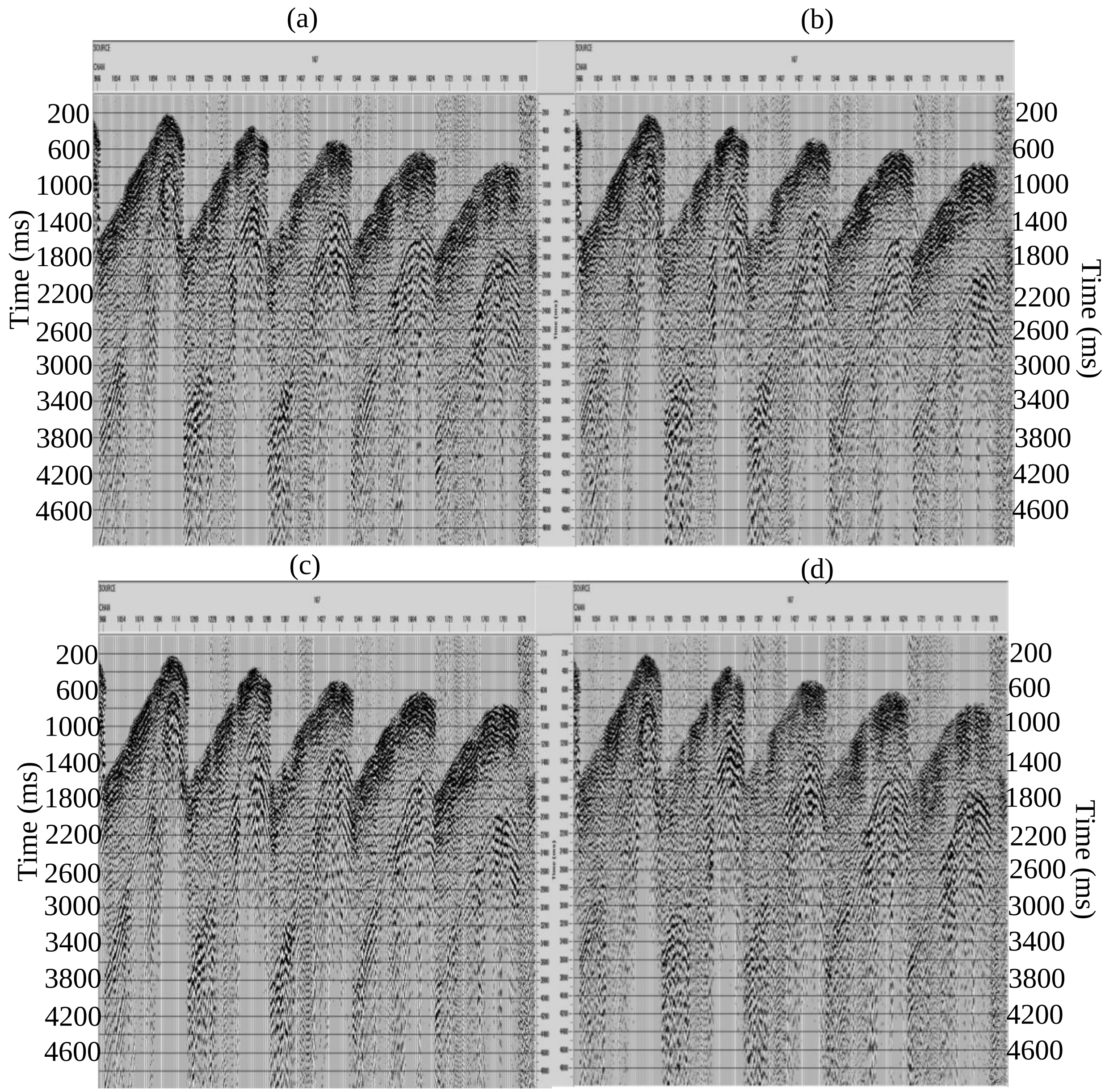

Figure 5.1: Comparison of (a) H1, (b) H2, (c) Radial and (d) Transverse

5.2.3 Radial Trace Filter

After modifying the offset trace headers as shown and explained in chapter 2, the radial and transverse components were appropriately set for the application of a radial trace filter. Figures 5.2 and 5.3 compare a shot gather of radial and transverse components before and after applying the radial trace filter, also showing the noise removed.

(a)

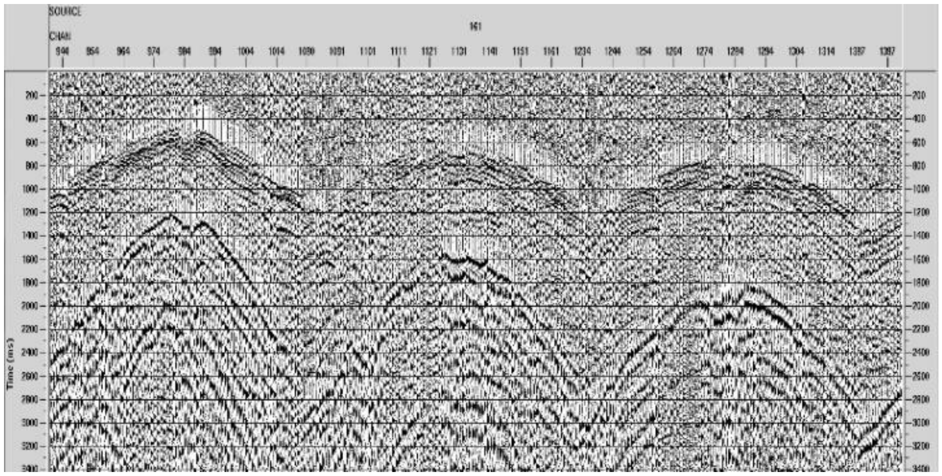

(b)

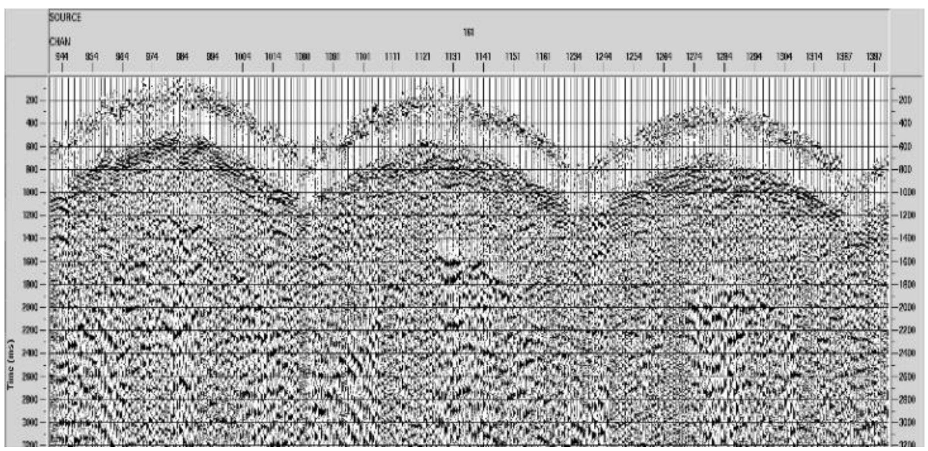

(c)

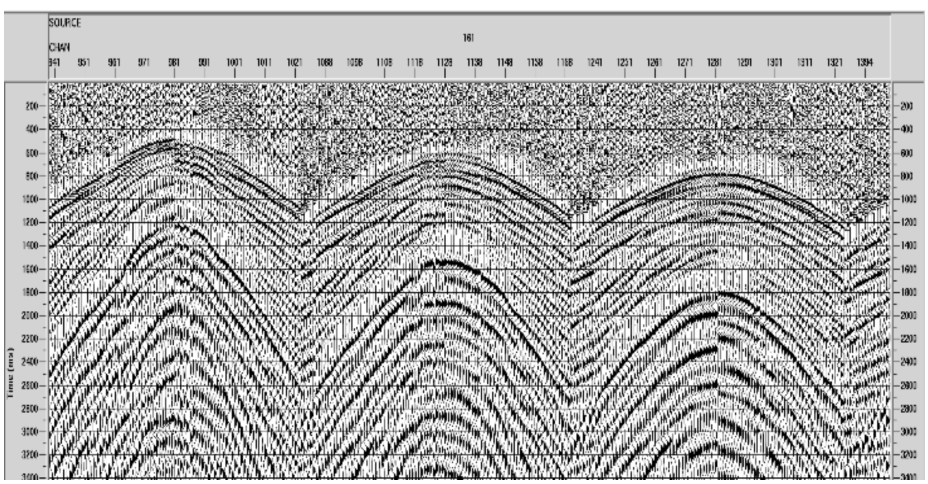

Figure 5.2: Radial component (a) before and (b) after applying the radial trace filter, and (c) the noise deleted

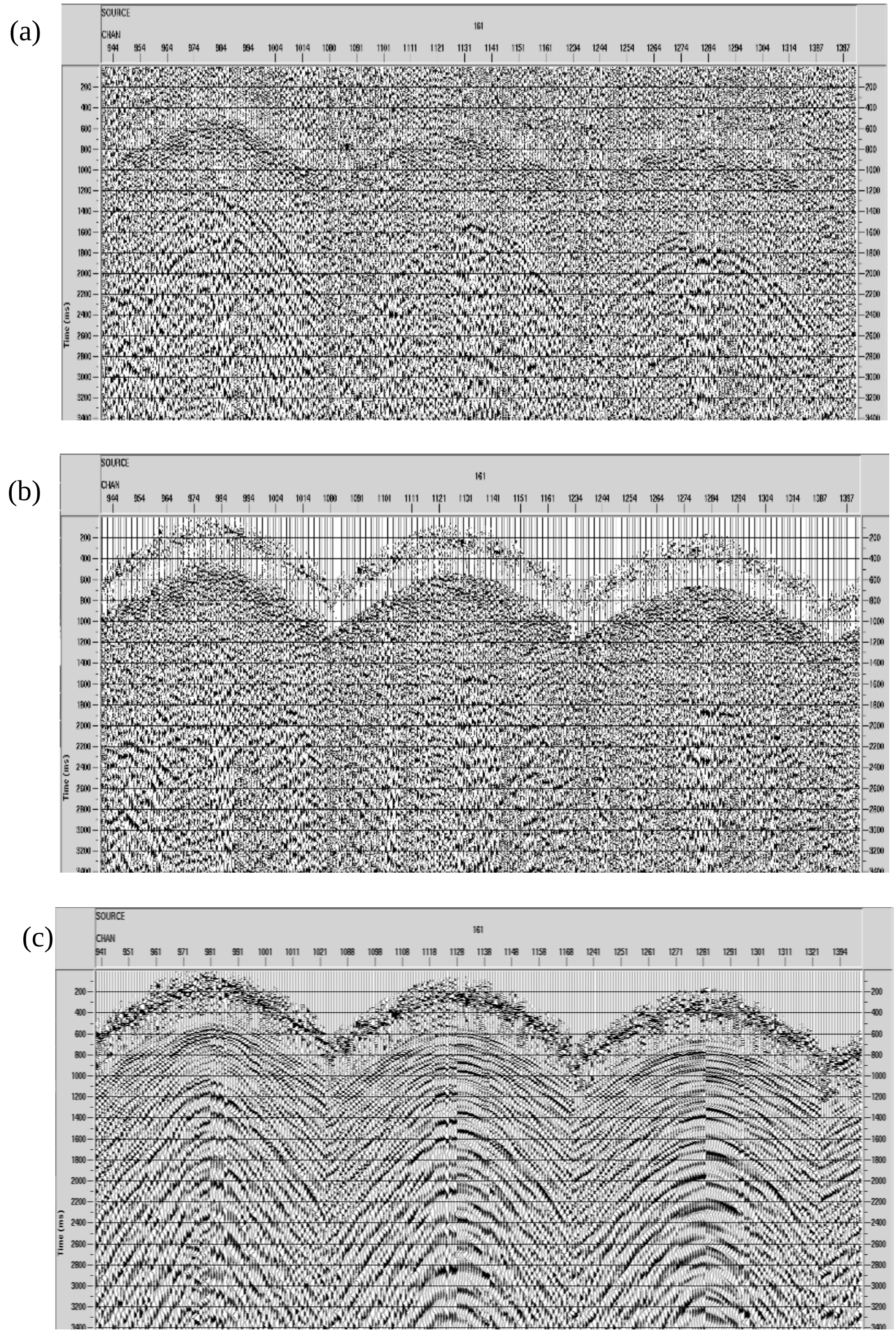

Figure 5.3: Transverse component (a) before and (b) after applying the radial trace filter, and (c) the noise deleted

5.2.4 Elevation and static correction

Elevation statics were applied in the same way as was done for the vertical component data in the previous chapter. However, weathering static correction for P-S data is different and challenging.

Since the source is the same for both P-P and P-S data, the shot statics were assumed to be the same for both datasets. Therefore, we applied the shot statics from the vertical component to the radial component. But due to the different path the rays of reflections take from the reflection points to the receivers, receiver statics will be different than the receiver statics used for the vertical component. Correcting for receiver statics was undertaken the following steps: first, we apply the shot statics we calculated for the vertical component. Then, we create common receiver stacks, and we select a horizon or horizons on the receiver stack. Following that, we smooth the picked horizon. Lastly, we subtract the original horizon from the smoothed one and these values would be our receiver static solution.

When creating the common receiver stacks, we converted P-P velocities to converted wave velocities using V_p/V_s ratio to be 2.01. Figure 5.4 shows a common receiver stack with shot statics applied, and shows the horizon picked with comparison with a smoothed one. The subtraction of these two horizons yielded the receiver statics for the P-S data (Figure 5.5). Finally, we applied the receiver statics. Figure 5.6 shows a CMP stack before and after applying the receiver statics.

5.2.5 Gain Recovery and Surface Consistent Amplitude Scaling

This step was performed exactly as we did for the vertical component in the previous chapter.

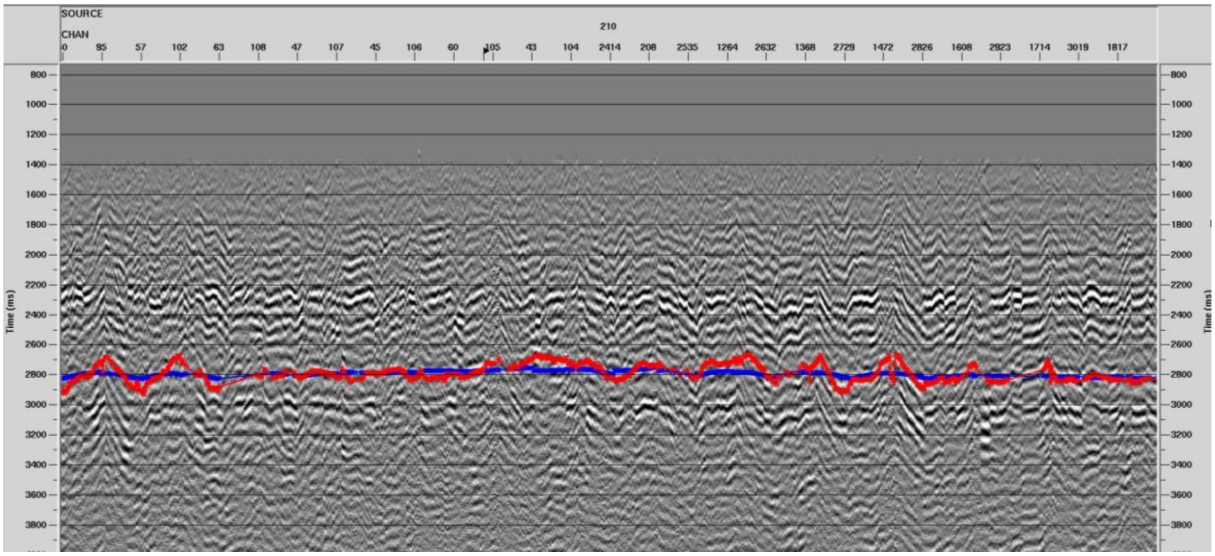

Figure 5.4: A receiver stack after applying the shot statics calculated from the P-P data. The horizon in red is the original one picked. The blue horizon is the smoothed one.

5.2.6 Seismic noise attenuation

For the vertical component processing, we applied surface wave attenuation, coherent noise attenuation and bandpass filter. But for the P-S data, we only applied the surface wave attenuation and bandpass filter to avoid removing some signal since the difference between signal and noise velocities is smaller than it is in the vertical component. In addition, we had already applied the radial trace filter on the converted wave data and applying more noise attenuation filters could be harsh on the data. Figure 5.7 shows the effect of the noise attenuation.

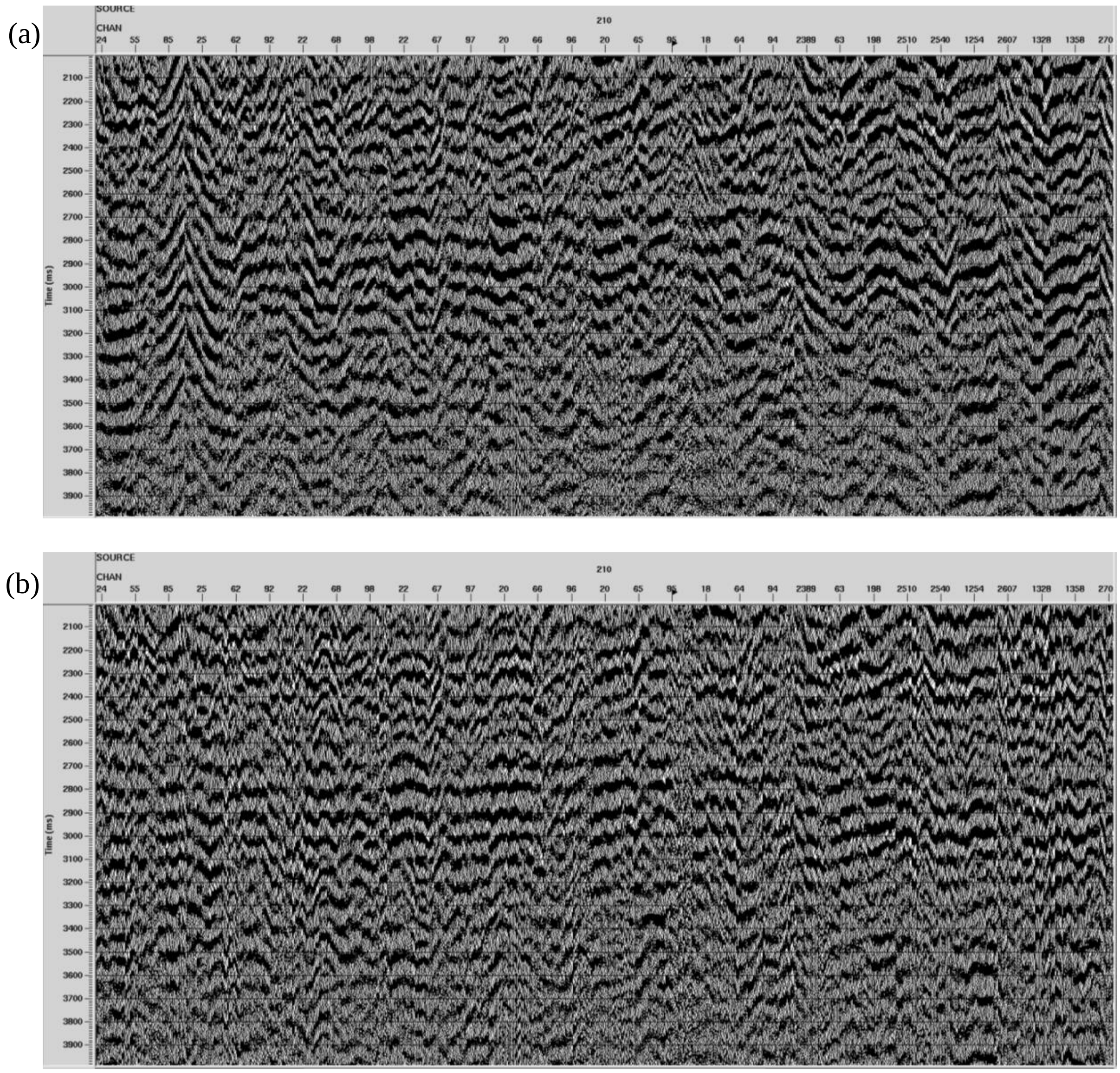

Figure 5.5: (a) Receiver stack before and (b) after applying receiver statics

5.2.7 Surface consistent deconvolution

This step was performed exactly as in the previous chapter when we processed the P-P dataset. Figure 5.8 shows the effect of deconvolution on the shot gather data of the converted wave.

Similar to the P-P data, a comparison of the amplitude spectra of the P-S data before and after applying the surface consistent deconvolution is shown in Figure 5.8. In this case deconvolution whitens the spectrum, as shown in Figure 5.9.

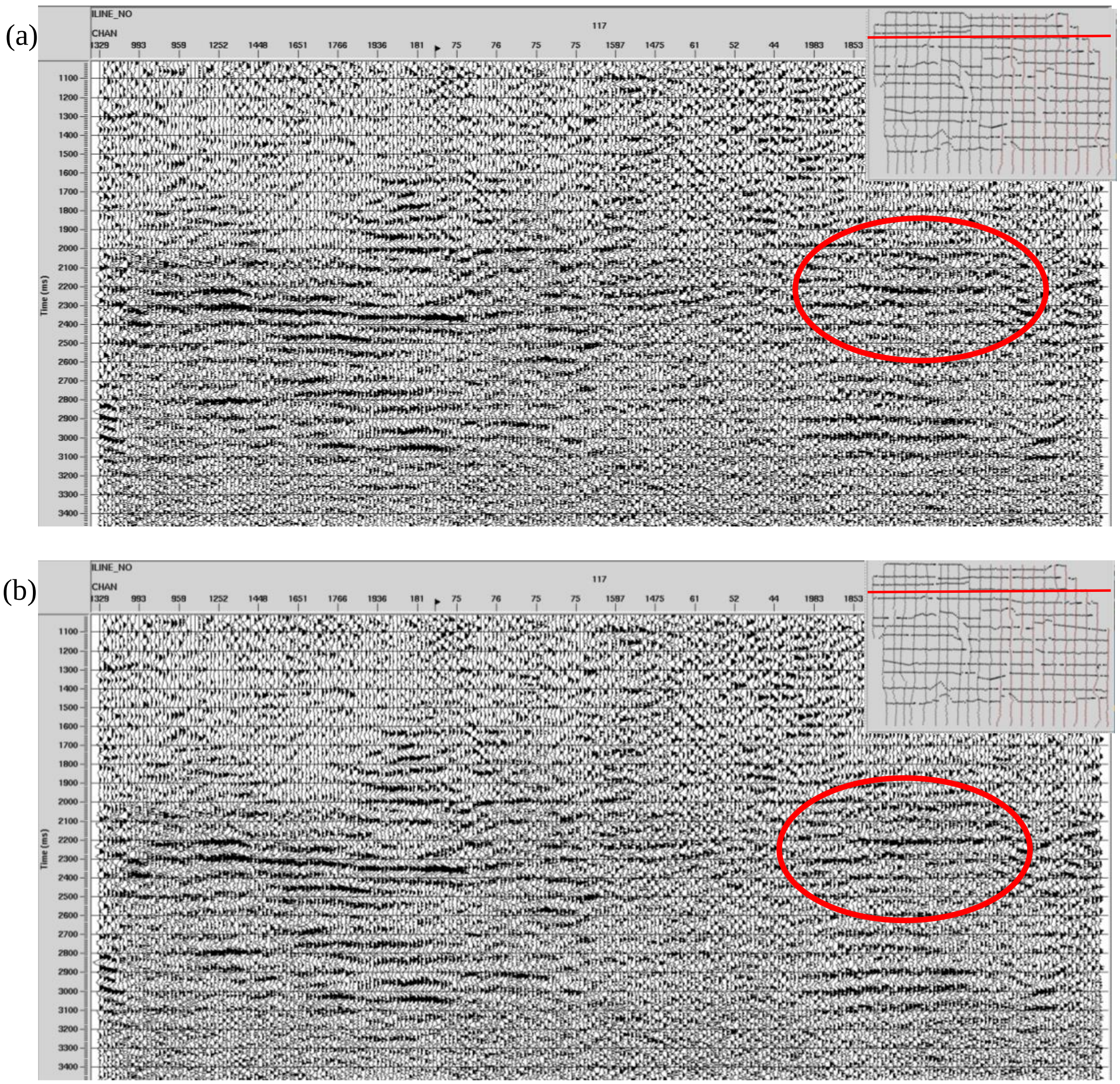

Figure 5.6: (a) CMP stack in the inline direction with only shot statics applied to it. (b) The same stack with shot and receiver statics applied. The circled area shows a better imaged reflection due to the correction of receiver statics.

(a)

(b)

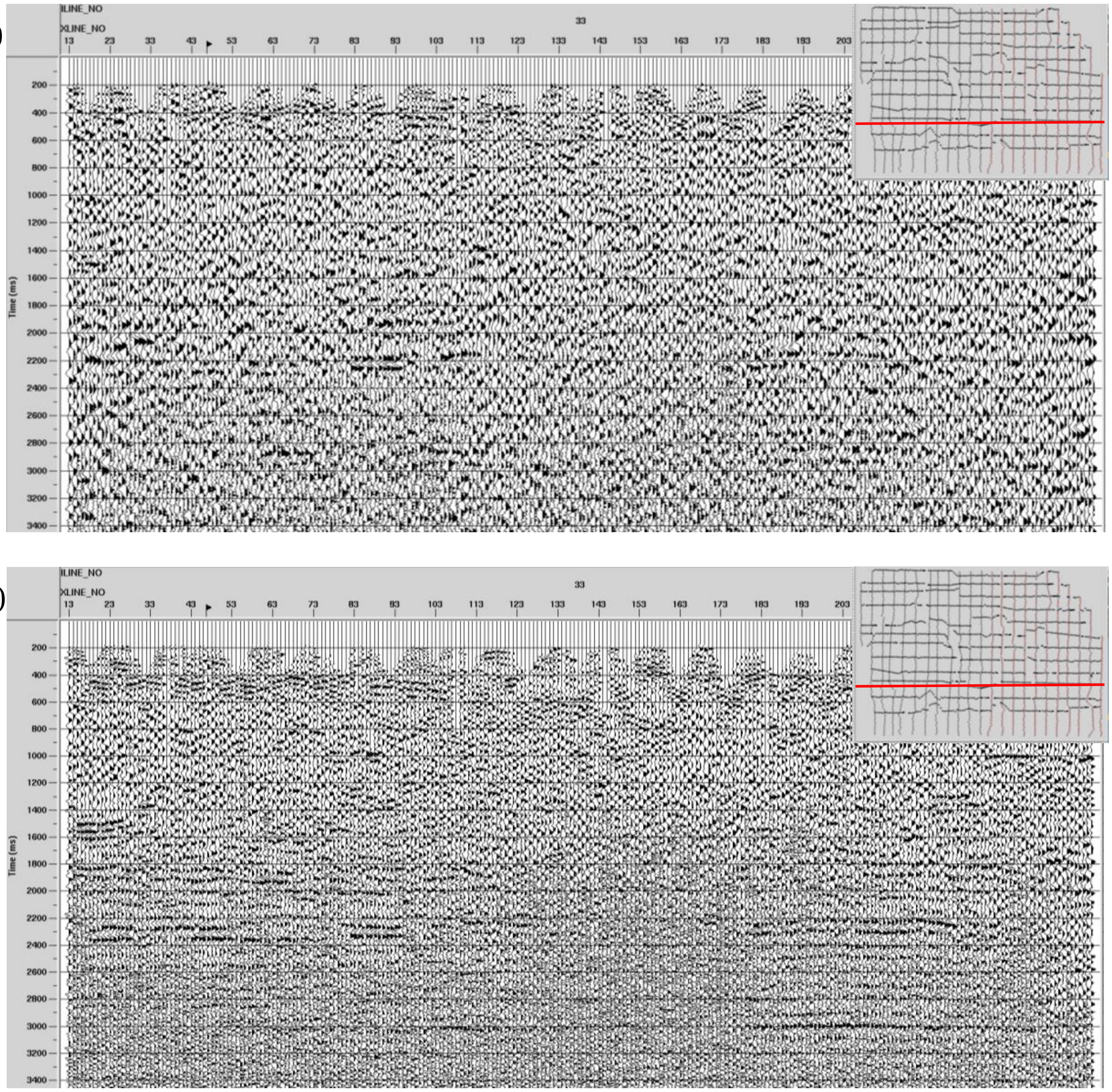

Figure 5.7: (a) A stack in the inline direction before and (b) after applying surface wave noise attenuation and bandpass filter

5.2.8 First pass of velocity analysis

Velocity analysis is one of the different steps from the P-P processing workflow. Initial Velocities were not picked for the P-S data due to the difficulty to identify and image reflections.

However, V_p velocities were converted into V_s using a V_p/V_s value of 2.01. these converted velocity functions are the ones used in the stacks from previous steps.

(a)

(b)

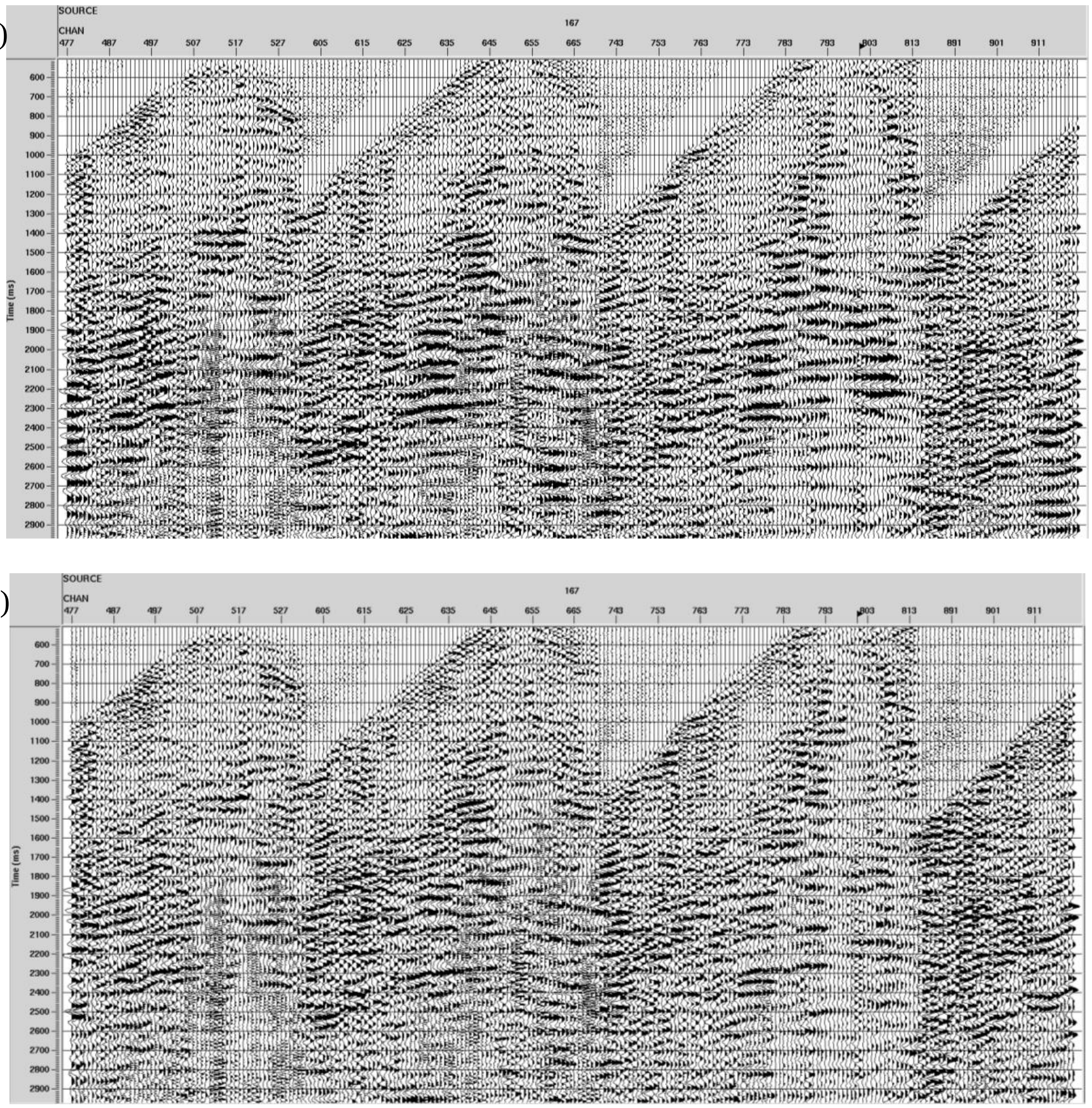

Figure 5.8: (a) A shot gather before applying surface consistent deconvolution and (b) after applying it. Reflections are sharpened after applying surface consistent deconvolution.

A comparison between the best velocity we obtained from P-P data and the velocity derived from it using the ratio $V_p/V_s = 2.01$ is shown in Figure 5.10.

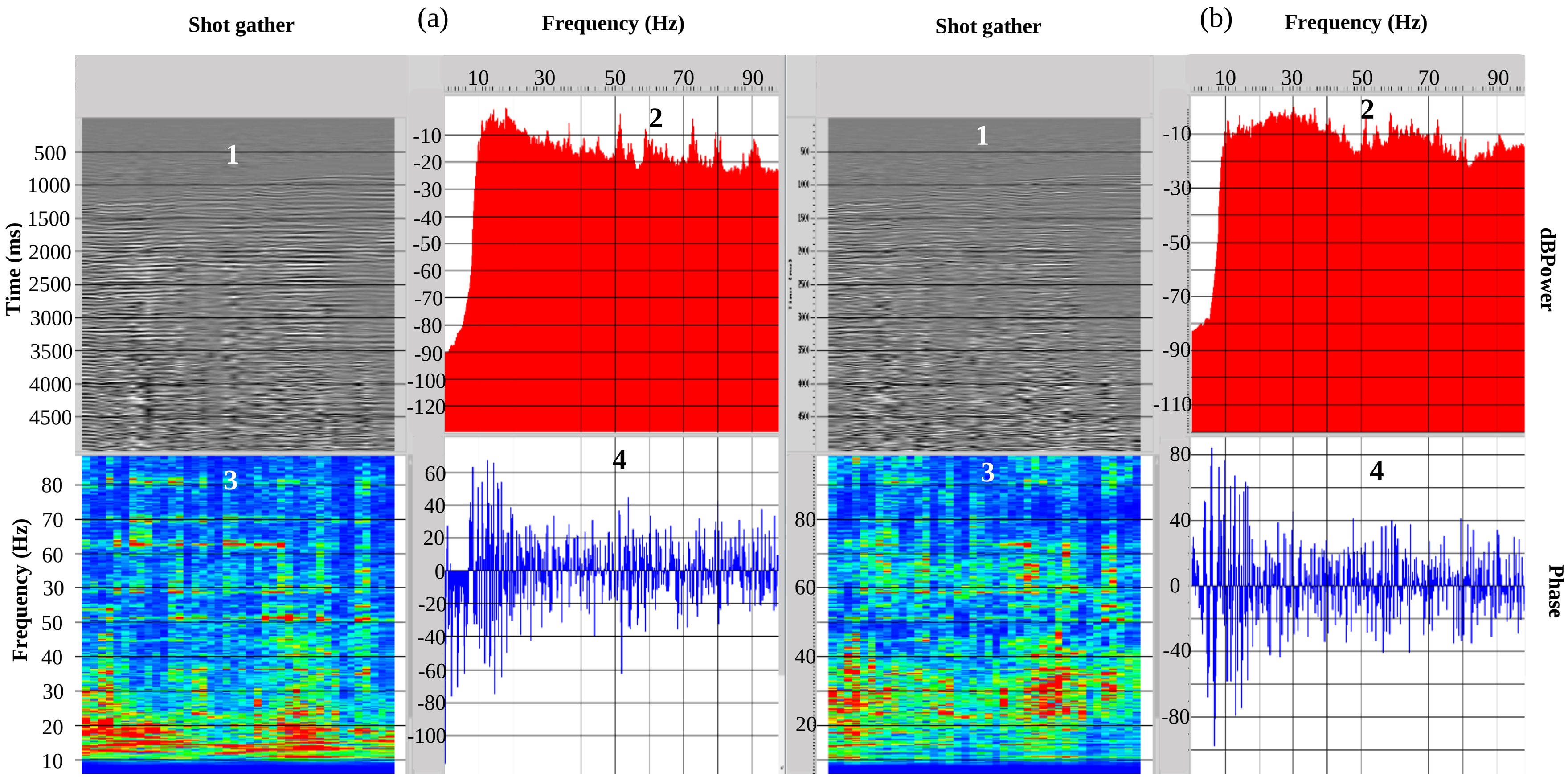

Figure 5.9: (a1) and (b1) are shot gathers. (a2) and (b2) are the amplitude spectra. (a3) and (b3) are the frequency vs offset plots. (a4) and (b4) are the phase vs frequency plots. (a) Amplitude spectra of P-S data before surface consistent deconvolution and (b) spectra analysis after applying it. Deconvolution boosted frequencies by approximately 5 db

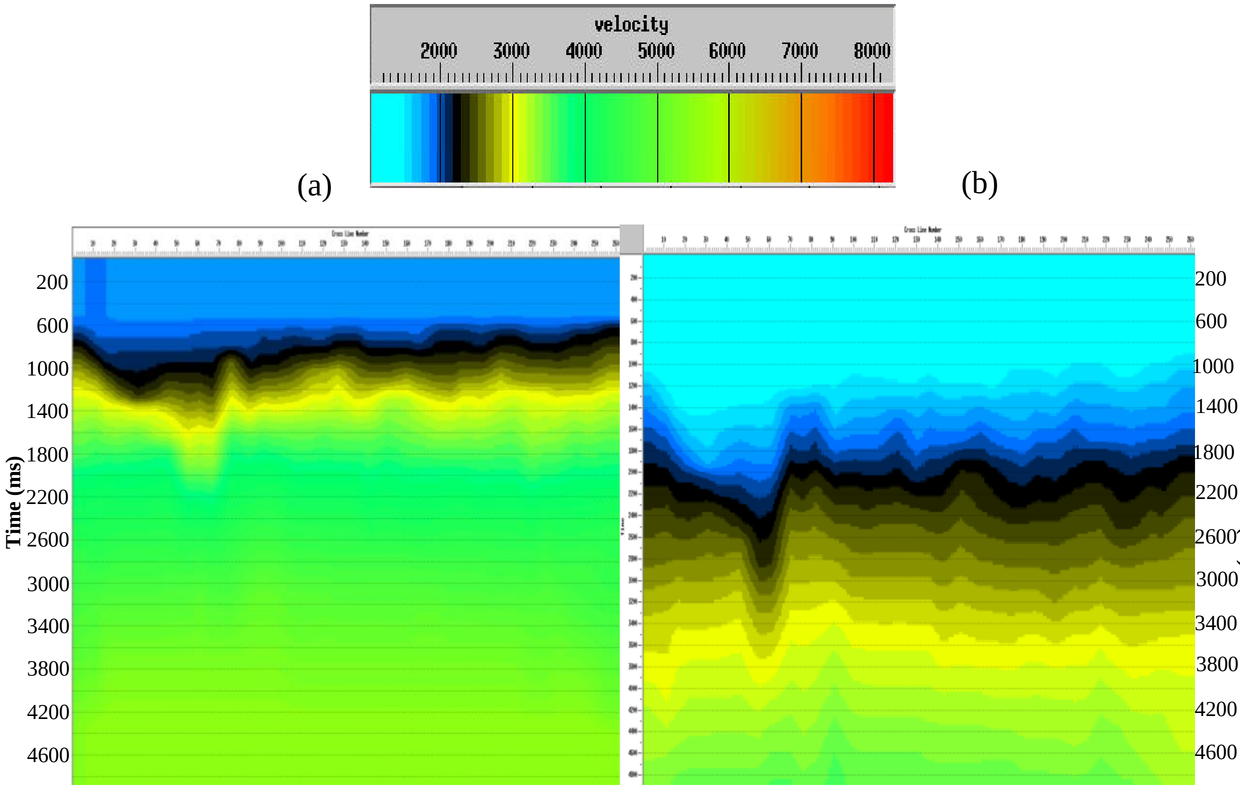

Figure 5.10: (a) RMS velocity of P-P data and (b) velocity of P-S data acquired from P-P data. These velocities from an inline that goes across the middle of the survey. The values in the color bar are in m/s

Velocity analysis is critical in P-S data processing because velocity and statics are directly related. And since we handled static correction differently in P-S data, specifically receiver statics, we expect to have variations in P-S velocity that straightforward conversion from P-P velocity will not honor. Also, reflections in P-S data are not as clear as they are in P-P data. Therefore, a sonic log data from a nearby well was used in order to help determine the velocity trend with depth and to increase our confidence in our velocity picking.

The sonic log extends to a depth of approximately 3700 m, which is approximately 2 seconds two-way traveltime. Figure 5.11 shows the sonic log with comparison to our picks.

The supergathers CDPs were computed the same way as for the P-P data.

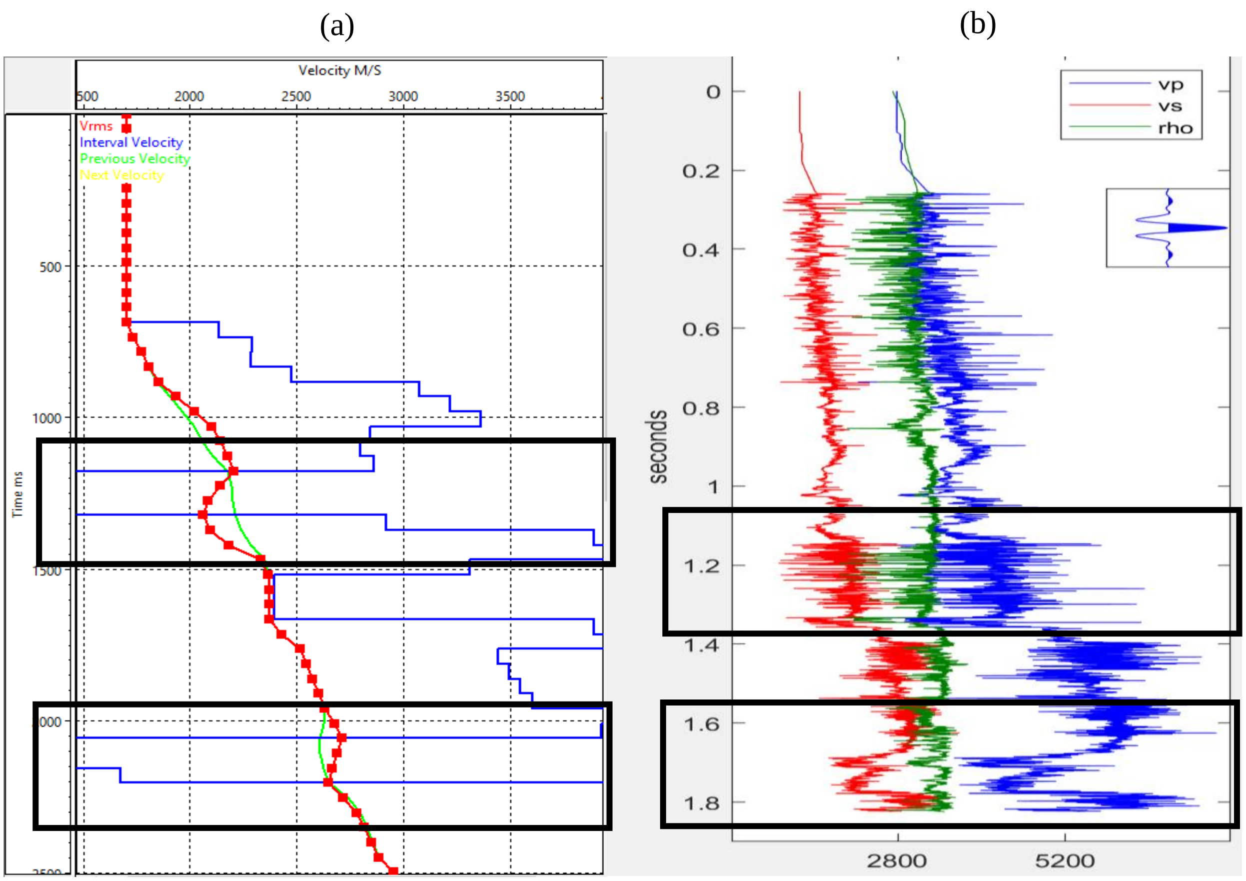

Figure 5.11: The trend of velocity variation with depth in (a) mimics the Vs from well velocity in (b). The general trend is increasing velocity with depth as normal with two kickbacks around 1.3 and 2 seconds as indicated

The first pass of velocity analysis helped improve several reflections at shallower depths that were not imaged previously. Moreover, it flattened the reflections as seen in Figure 5.12.

(a)

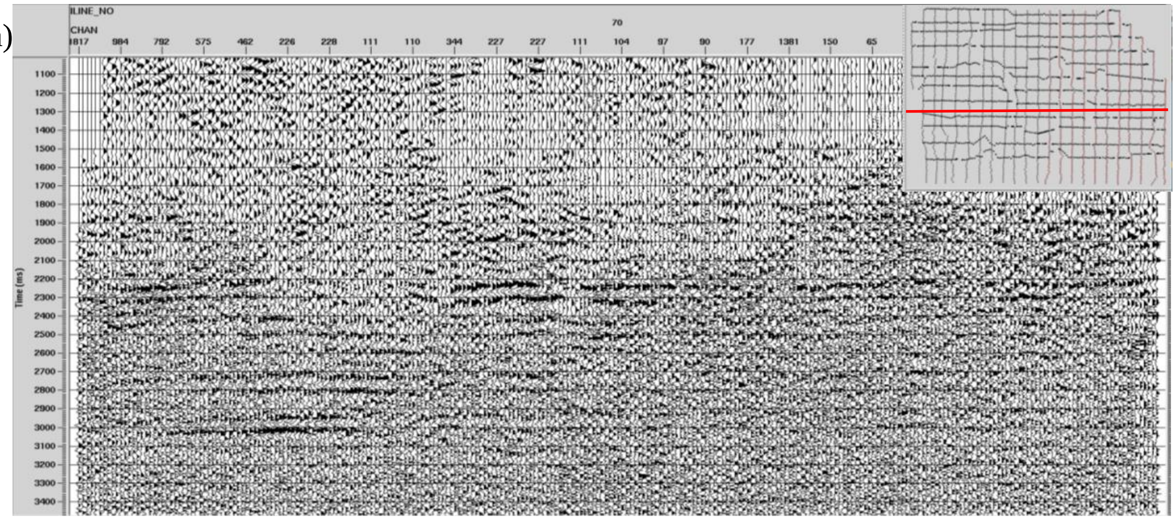

(b)

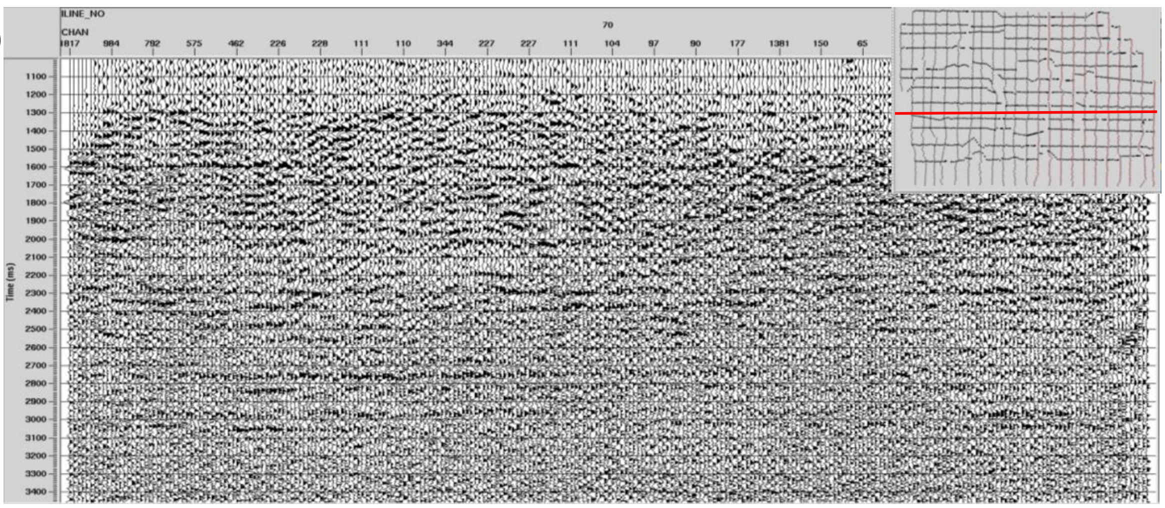

Figure 5.12: (a) A stack in the inline direction using the velocities converted from P-wave velocities. The result of first pass of velocity analysis. The new velocities in (b) imaged the reflections between 1300 – 2000 ms. It also flattened the deeper reflections. The reason why the deeper reflections look weaker because there are higher frequency reflectors in the shallow section. The deeper reflectors will be improved after residual and after removing some of the noise by F-X deconvolution later in the processing

Different velocity analysis tests were done to quality assure the velocity output. Figure 5.13 shows the results in the stack from these velocity analysis completed.

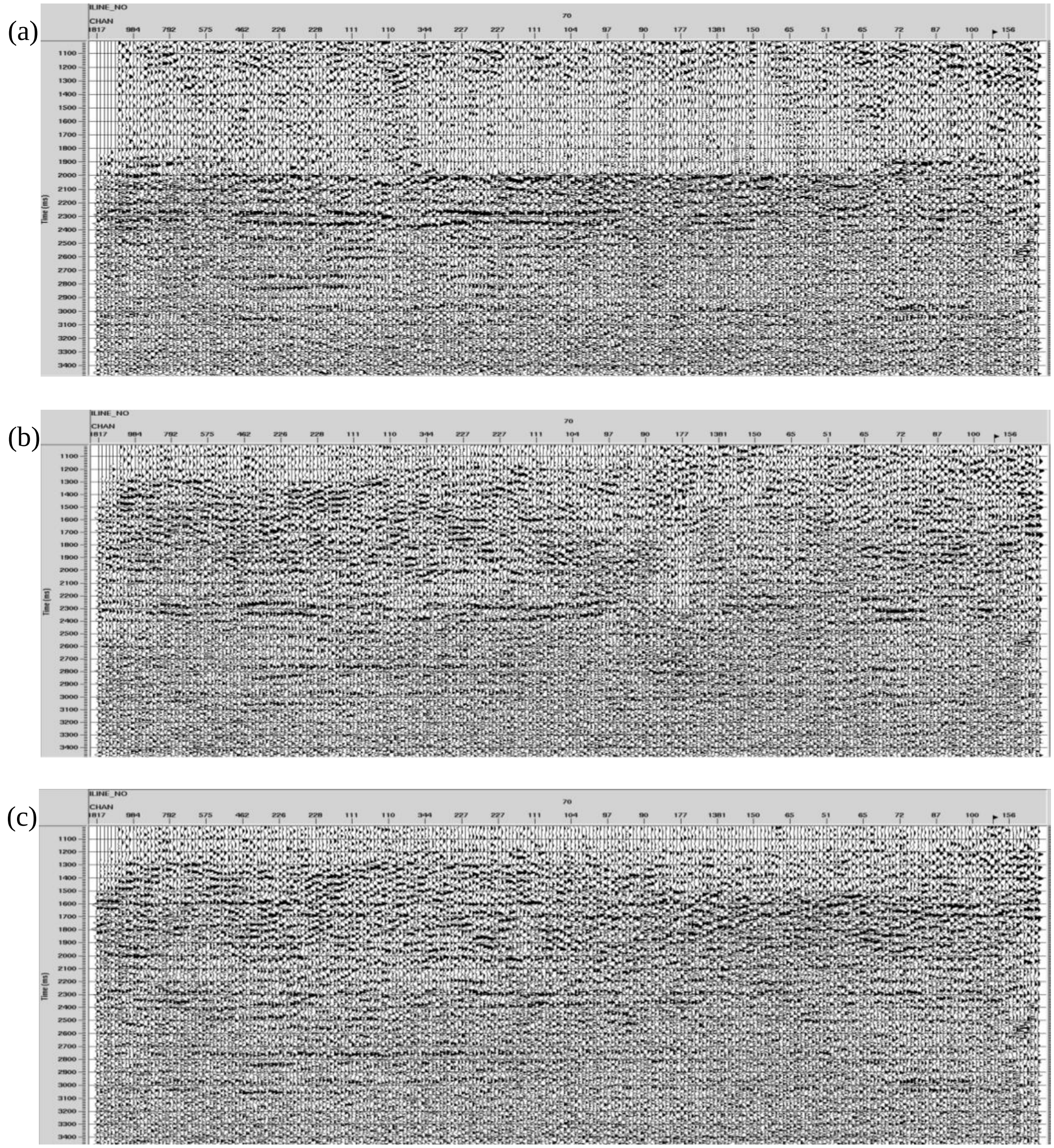

Figure 5.13: (a) First analysis was not good enough to image shallower reflectors. (b) The second one was successful in doing that. However, reflectors were not flat. (c) Lastly, velocities were able to image shallower reflectors and flat the reflectors across the stack

5.2.9 First pass of residual statics

For the residual statics, we followed the same workflow in the P-P data processing. The only difference here is we conditioned the data by applying F-X deconvolution to help pick the autostatic horizons. Figure 5.14 shows the horizons picked for residual statics and used for the calculating the residual statics. And Figure 5.15 shows the effect of residual static correction on the stacked data.

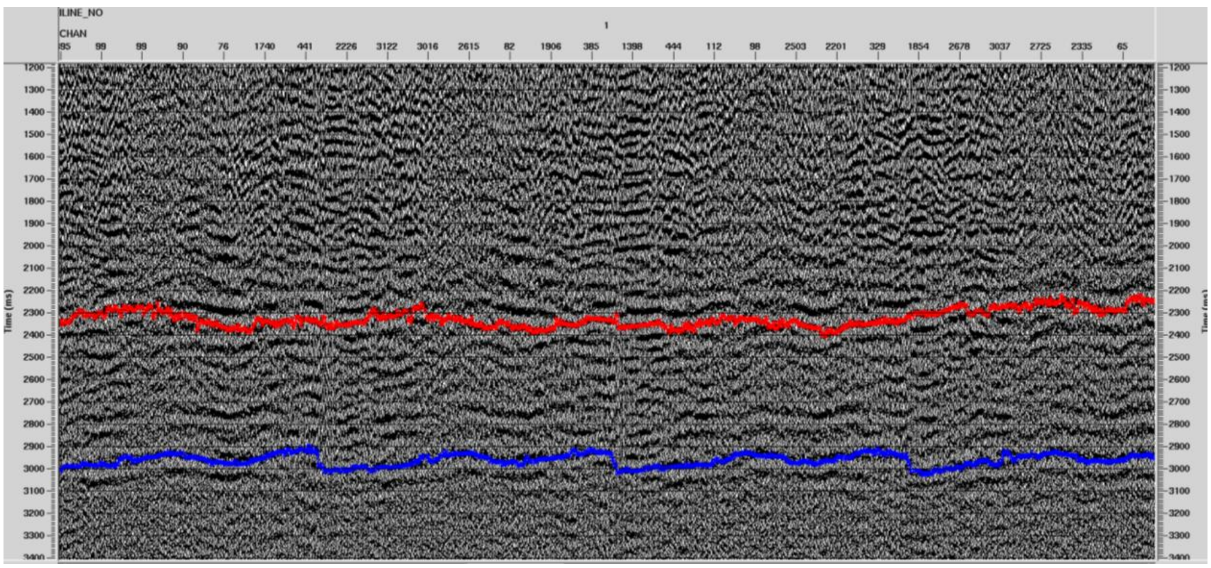

Figure 5.14: Two autocorrelation horizons are picked for the residual statics to avoid biasing

5.2.10 Second pass of velocity

The second pass of velocity step is to fine tune the first velocities that had been picked earlier. What is expected is to see a better coherence in some reflectors and flatter reflectors than before. Figure 5.16 shows the stacked data after the second pass of velocity analysis.

(a)

(b)

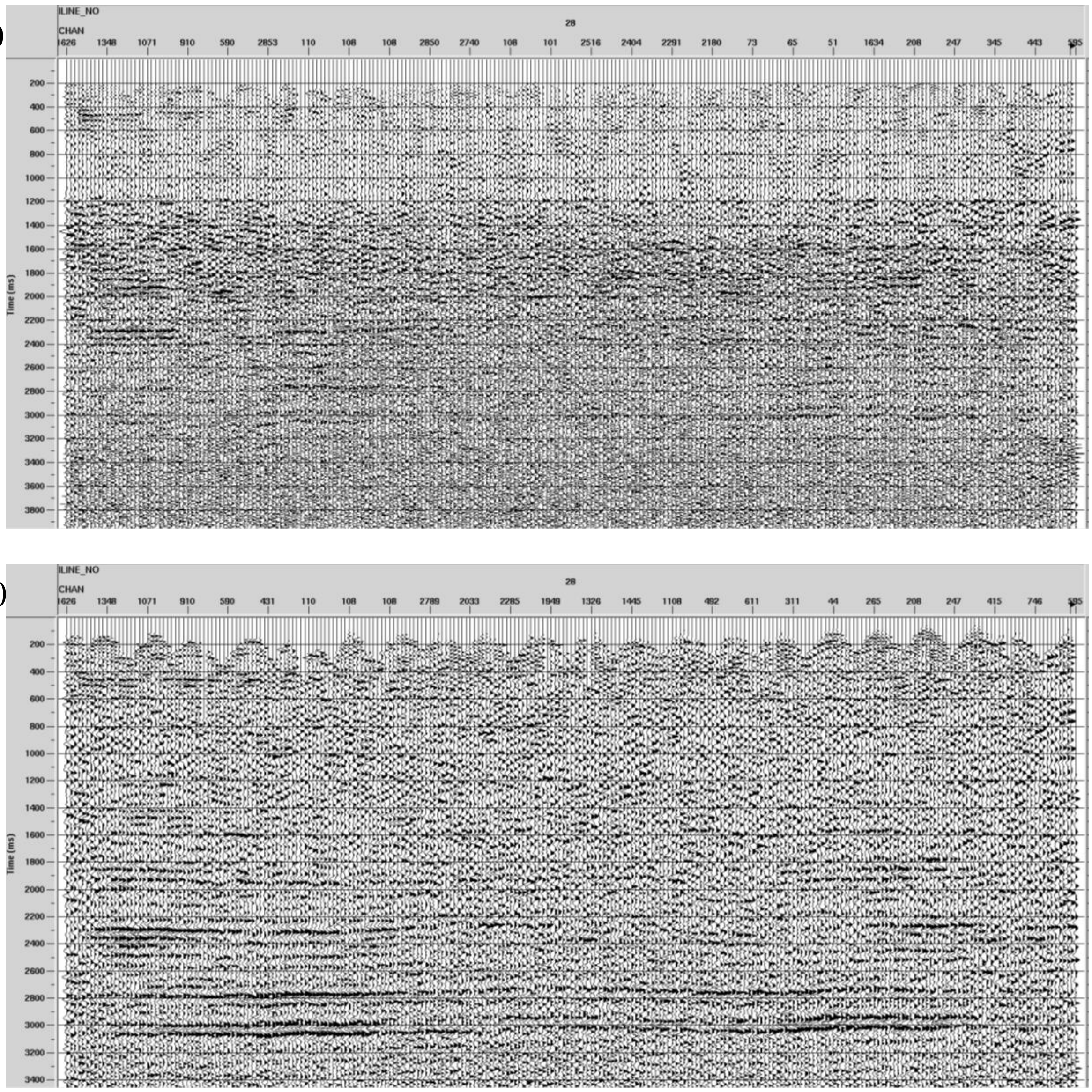

Figure 5.15: (a) An inline example of P-S data before the first pass of residual and (b) after applying the residual statics. The deeper reflectors are better imaged. Also, some of the noise in the shallower depth were removed so the reflectors are better imaged as well

5.2.11 Second pass of residual statics

Again, we picked other two autostatic horizons for the second pass of residual. However, this time we picked them on the stack volume created using the new velocities with the first pass of residual statics applied. Also, we applied F-X deconvolution to simplify the picking process. Figure 5.17 shows the two autostaic horizons picked, and Figure 5.18 shows the results of the second pass of residual statics.

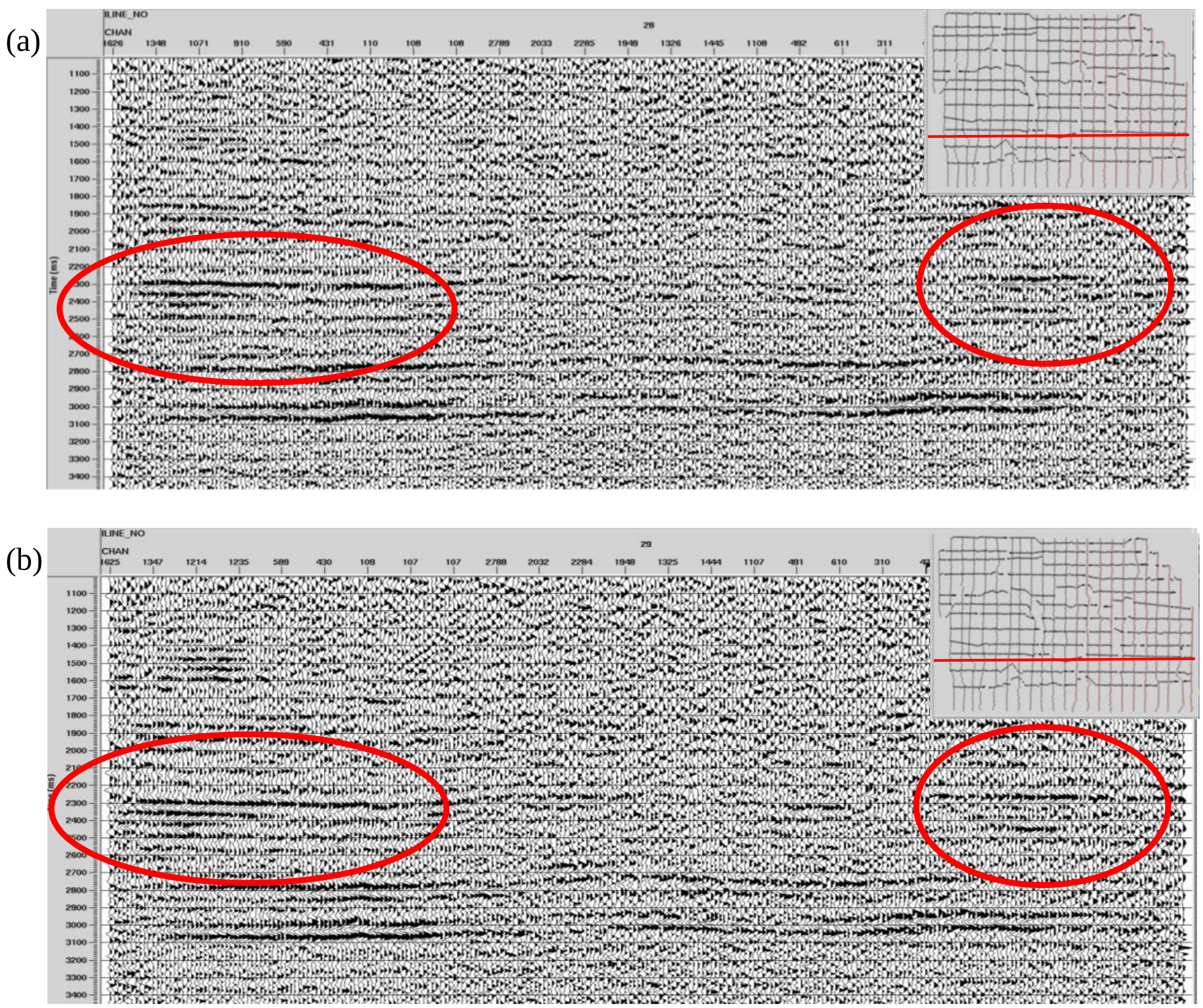

Figure 5.16: Inline example shows the effect of the second pass of velocity on the stacked data. the circled areas show the improvement caused by the new velocities

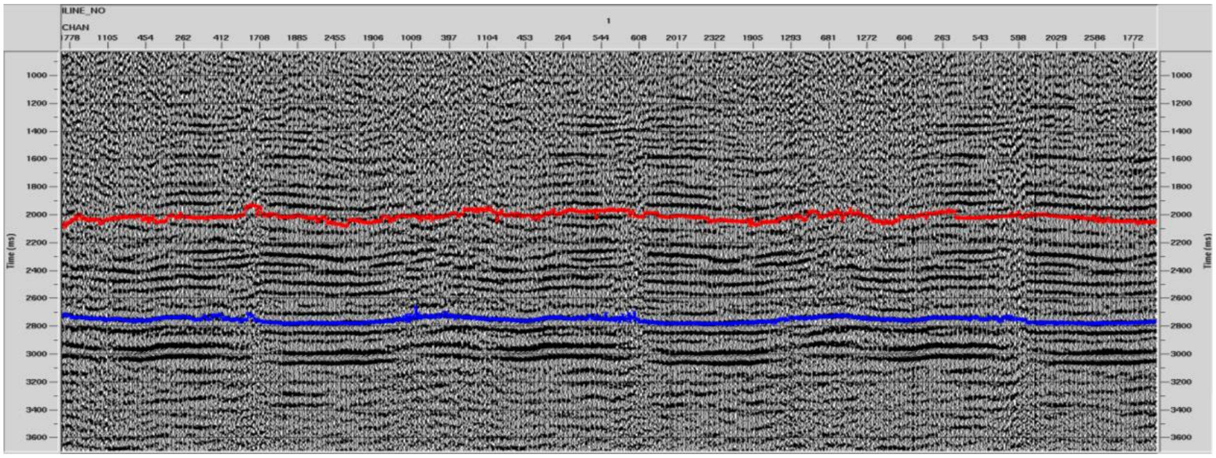

Figure 5.17: The autostatic horizons picked and used in the calculation of the second pass of residual statics

(a)

(b)

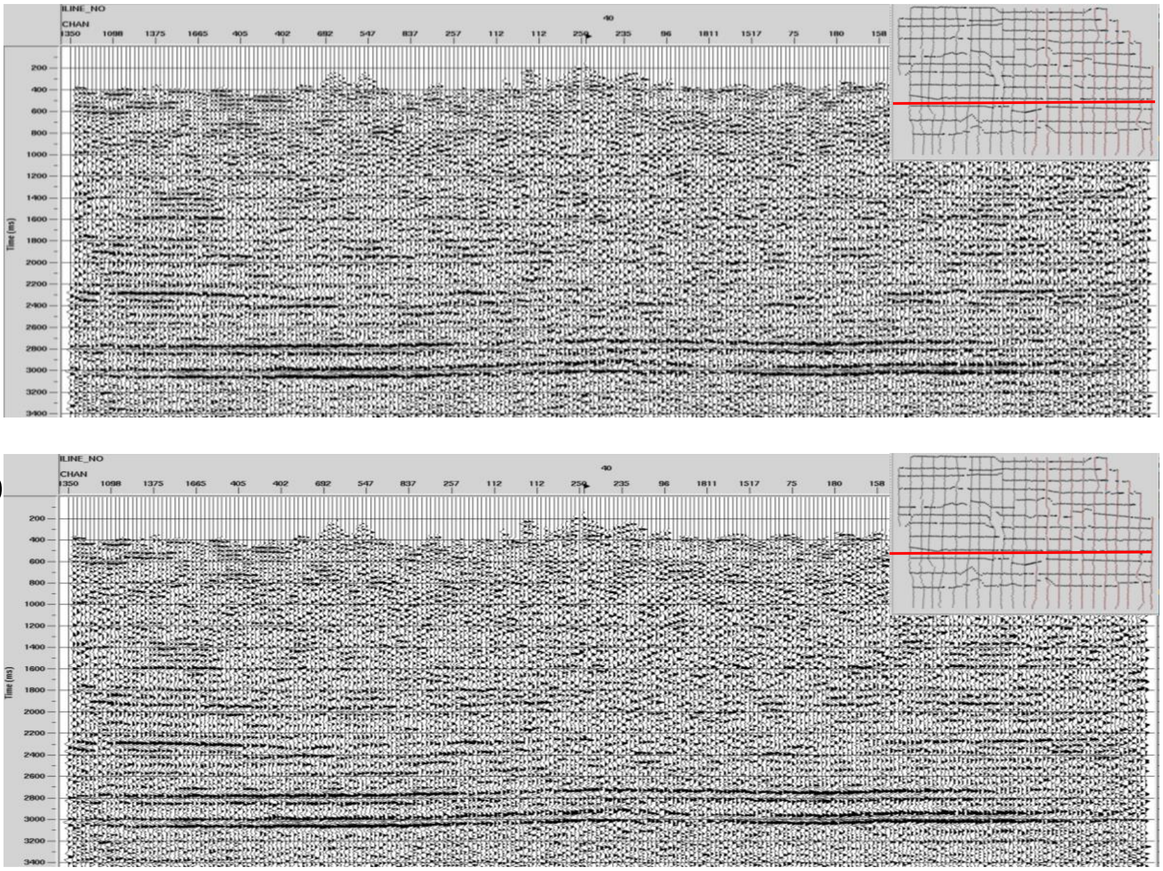

Figure 3.18: Stack section after (a) first pass of residual statics with the second pass of velocity analysis. (b) The second pass of residual statics

5.2.12 PP-PS event registration

An important step in P-S data processing is to tie the horizons of the PS data to the PP data. At this stage, the PS data is processed to an interpretable level where we can match the horizons from both volumes. We can use the synthetic stacks created in chapter 3 using well data to provide the tie of the real data. Figure 5.19 shows the synthetic stacks using sonic logs and designed wavelets.

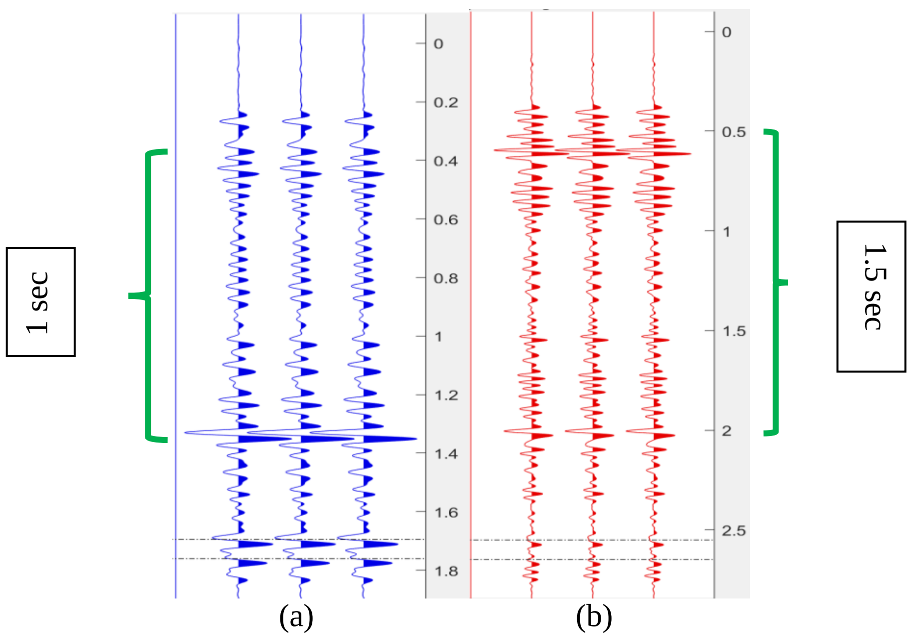

Figure 5.19: (a) PP synthetic stack and (b) PS synthetic stack

From the PP and PS synthetic tie, we see that Duvernay which is around 1800 ms ties with 2800 ms in the PS stack. In addition, event at 1500 ms in the PP stack has the same signature of the one at 2300 ms in the PS stack, and similarly the events in the PP and PS stacks at 1200 ms and 1600 ms, respectively. Traveltimes ratio between PP and PS data is approximately 1.5 seconds which is something we will evaluate in the real data.

At this point, the best stack we have of PS data is after applying the second pass of residual statics. Therefore, we will tie the horizons in the stack after applying the second pass of residual statics of PP and PS data. Moreover, post stack F-X deconvolution filter is applied to both datasets to simplify and enhance the event registration process. Figure 5.20 shows the event registration at the same inline where we correlated the velocity fields of both datasets.

(a) (b)

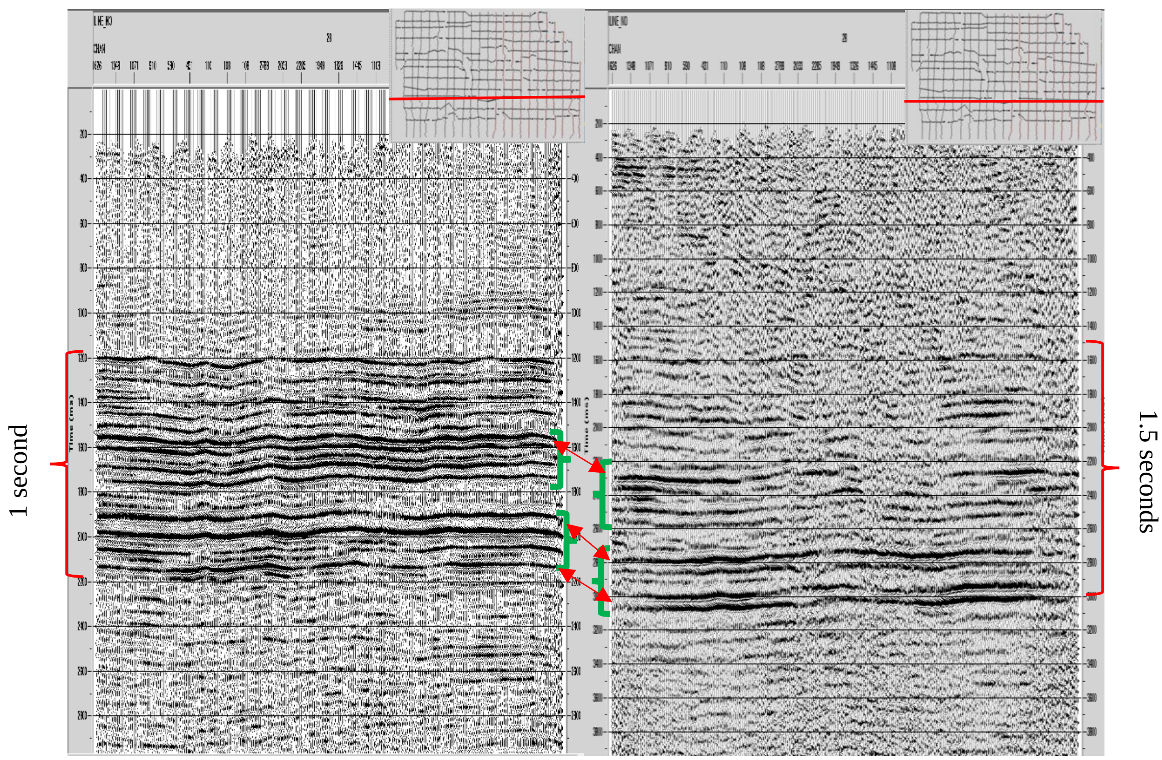

Figure 5.20: (a) PP stack after applying second pass of residual statics and (b) PS stack after applying second pass of residual statics. Red arrows show the horizons tie as expected from synthetic data and velocity fields. Horizons at 1.58s, 1.9s and 2.1 in PP data tie with horizons at 2.3s, 2.8s and 3.1s respectively. Moreover, events indicated by green braces tie with each other. Lastly, the traveltimes ratio of the whole package compared in both datasets agree with expected ratio; 1 second in PP data to 1.5 seconds in PS data

Amplitudes of P-P data and P-S data are different in Figure 5.20. That could be caused by the source amplitudes, receiver site effects, different geometrical spreading between P-wave and S-wave or that could be caused by reflection coefficients (Zoeppritz, 1919).

From Figure 5.20, we used the time of tied horizons of P-P and P-S data to calculate the interval V_p/V_s ratio using equation 5.1 (Garotta, 1987):

$$\frac{Vp}{Vs} = \frac{2\Delta Tps - \Delta Tpp}{\Delta Tpp} \tag{5.1}$$

Where $\boldsymbol{Tpp}$ is the two-way time of the wave traveling downward and reflecting upward using P-wave velocity, and $\boldsymbol{Tps}$ is the two-way time of the wave traveling downward using P-wave velocity and reflecting upward to the receiver using S-wave velocity. Table 5.2 shows the interval V_p/V_s ratios of sections indicated by tied horizons in Figure 5.20 using equation 5.1.

Table 5.2: PP and PS times used to calculate interval V_p/V_s ratios. V_p/V_s ratios are close to 2 which is the ratio expected.

T_{PP} intervals (ms)	T_{PS} intervals (ms)	Interval Vp/Vs
0 - 1580	0 - 2300	1.91
1580 - 1900	2300 - 2800	2.12
1900 - 2100	2800 - 3100	2.0

Figure 5.21 shows the tie of synthetic seismograms with real data, and the interval Vp/Vs based on the tie.

6.2.12 Post-stack time migration

From this step to the end, we followed the exact workflow followed when processing PP data. The method to prepare the PS data for migration is the same one used when processing PP data; we padded the data in both inline and crossline directions, then F-X deconvolution was applied and finally migrated 4 seconds of the data with 50 degree maximum dip to image. Figure 5.22 and 5.23 show comparisons between the second pass of residual statics and velocity analysis with migrated data in both inline and crossline directions, respectively.

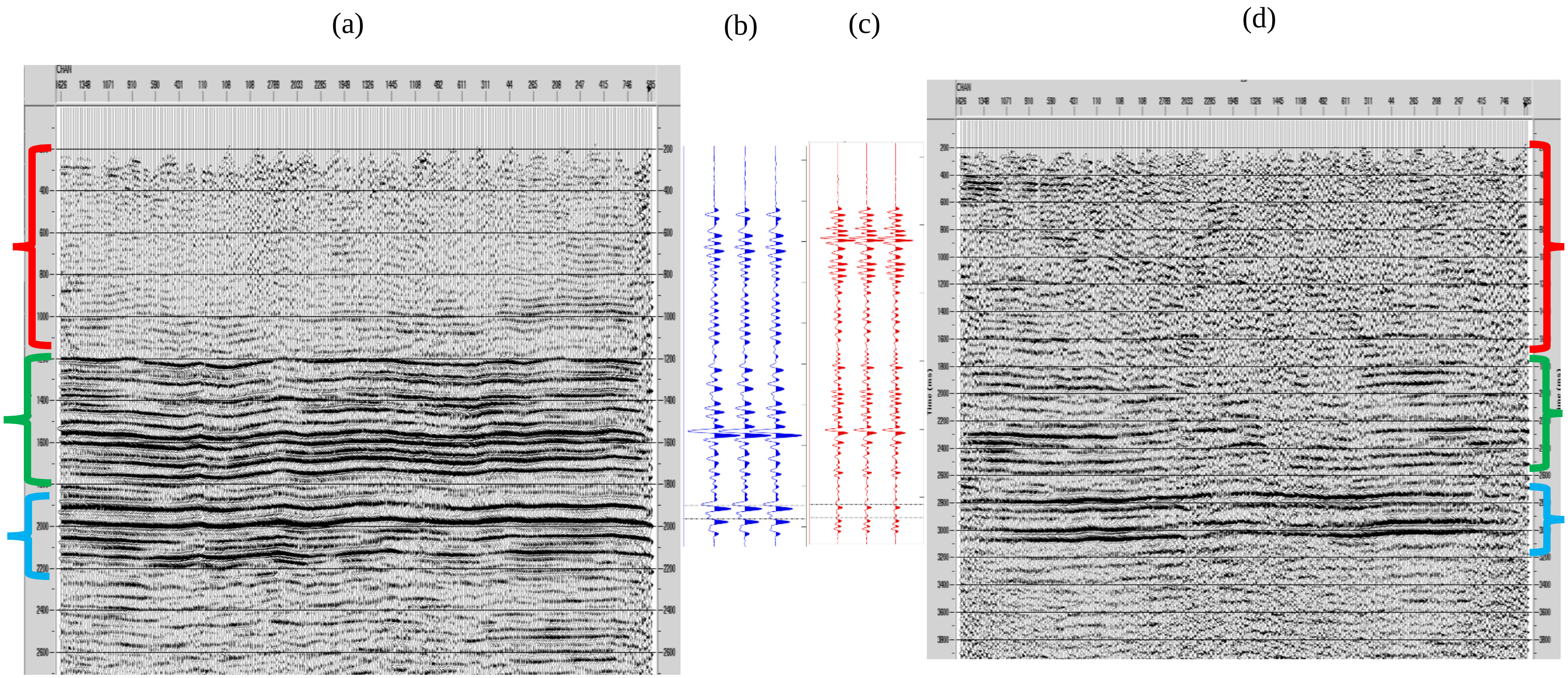

Figure 5.21: (a) P-P processed data, (b) P-P synthetic seismogram, (c) P-S synthetic seismogram and (d) P-S processed data. Interval V_p/V_s at the three indicated regions are: 1.91, 2.12 and 2 for areas indicated by red, green and blue, respectively.

(a)

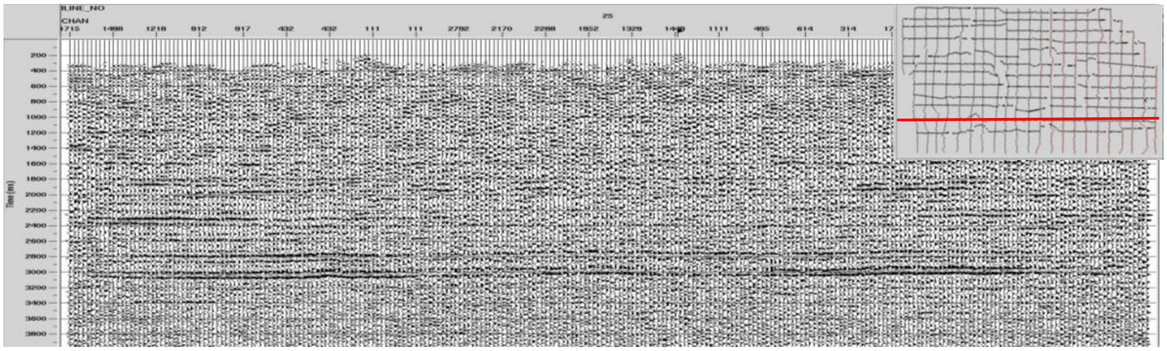

(b)

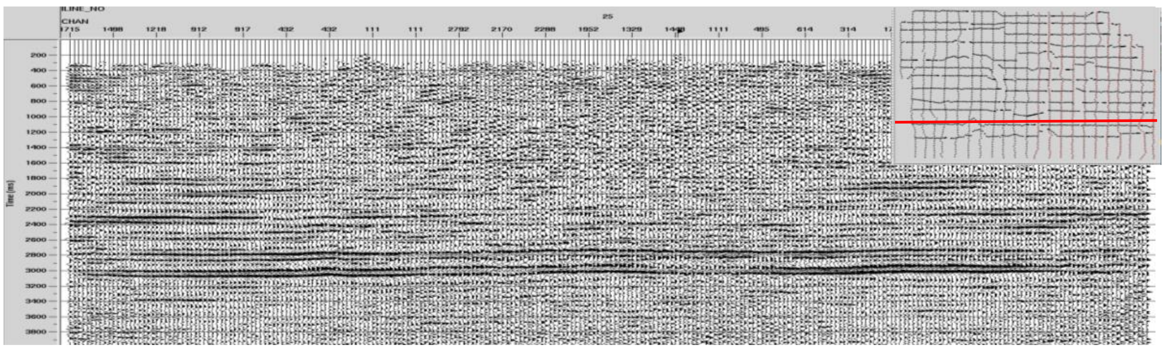

(c)

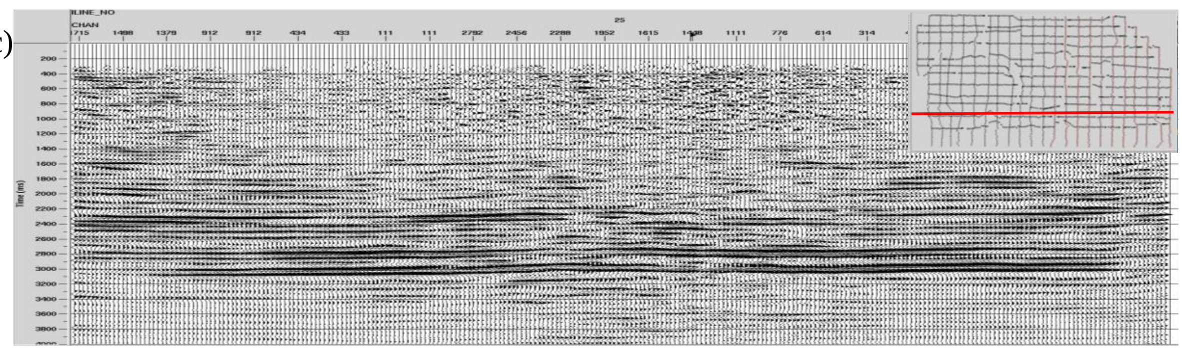

Figure 5.22: (a) An inline stack after applying the second pass of residual, (b) the same stack after applying F-X deconvolution and (c) the same stack after post stack migration

(a)
(b)
(c)

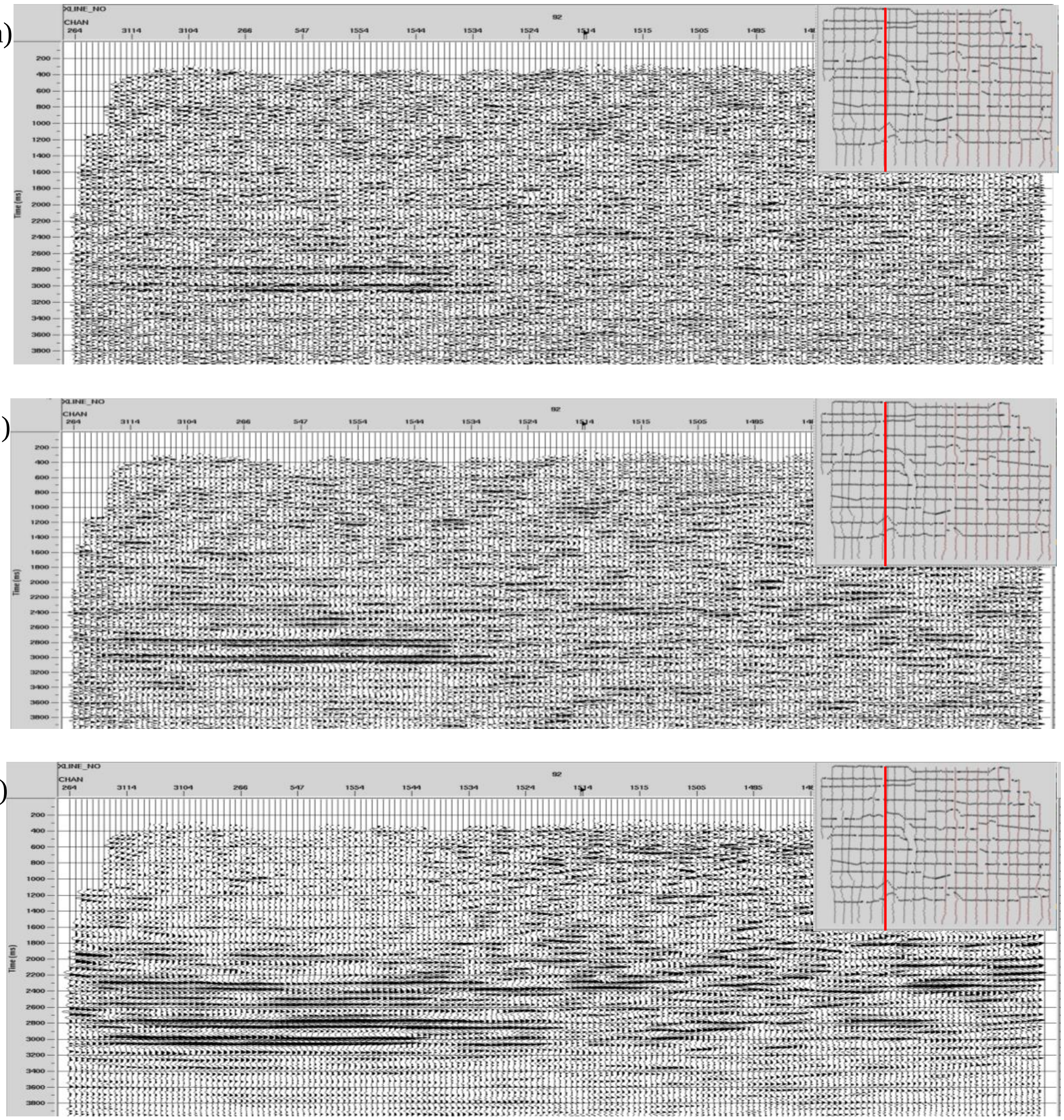

Figure 5.23: (a) A crossline stack after applying the second pass of residual, (b) the same stack after applying F-X deconvolution and (c) the same stack after post stack migration

Figure 5.24 shows a 3D processed volume of the P-S data.

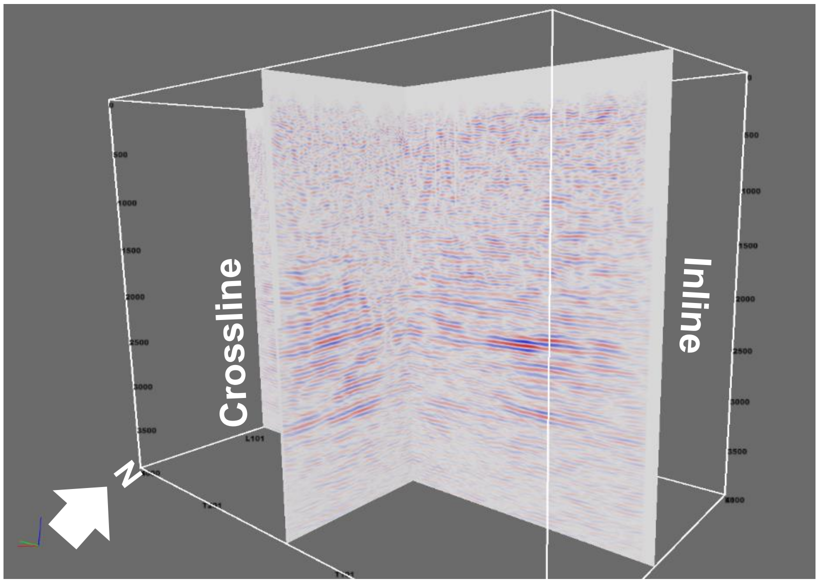

Figure 5.24: P-S migrated volume.

5.2.13 ACP and CCP stacks

As discussed in chapter 2, P-S data has different reflection geometry than P-P data where reflection points vary with depth. Reflection points are closer to the receiver at shallower depth and further from it at deeper layers (gunning 2016).

An easy way to stack P-S data is to use an asymptotic conversion point using constant V_p/V_s ratio. In this case, we used V_p/V_s ratio at the depth of interest which is 2.01. This asymptote is closer to the receiver and it is constant. This method creates what is called ACP stack.

Another method to stack P-S data is to use the RMS stacking velocities of P-P and P-S data to derive V_p/V_s ratios at different depths to honor the reflection point variation with depth. This method creates what is called CCP stack. Figure 5.25 shows the difference in reflection geometry between ACP and CCP, and Figure 5.26 shows an inline example of both ACP and CCP stacks.

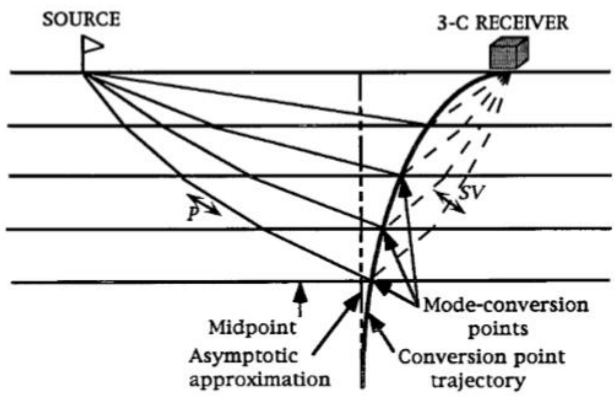

Figure 5.25: The asymptote conversion point uses a constant V_p/V_s ratio. However, common conversion points use different V_p/V_s ratios vary with depth (Schafer, 1992)

(a)

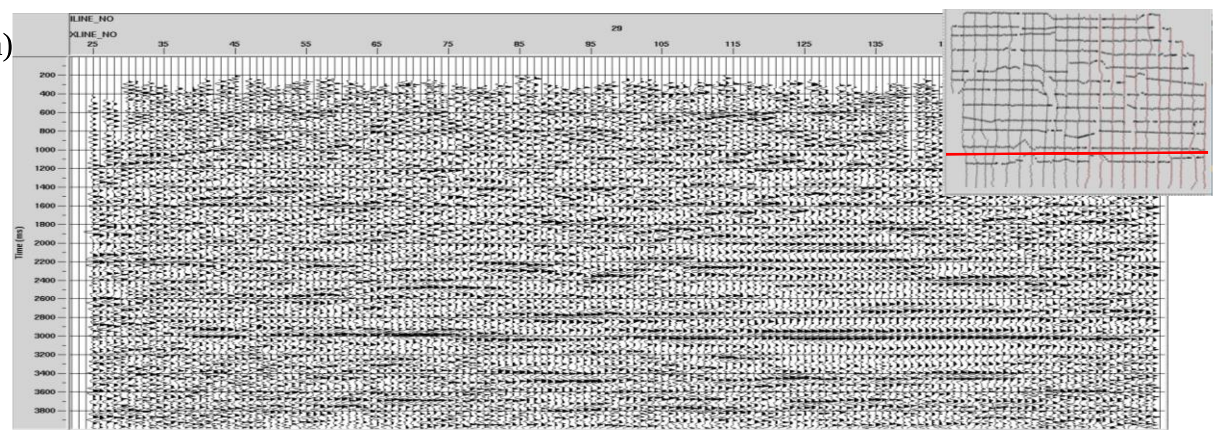

(b)

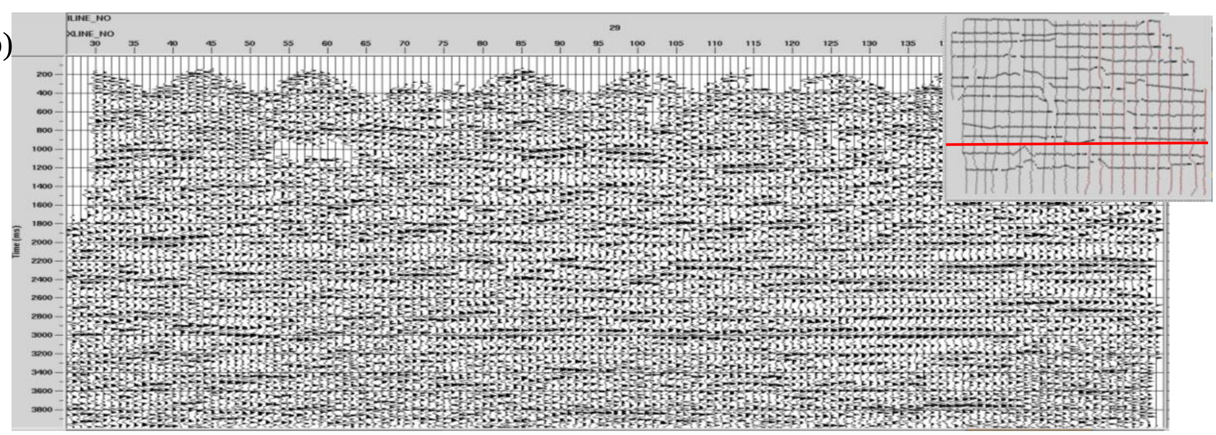

Figure 5.26: (a) ACP stack and (b) CCP stack. Constant asymptote in the ACP stack is decided based on the constant V_p/V_s ratio at the target around 2000 ms. That explains the better imaged shallow events in the CCP stack than in the ACP one. Because the difference between the asymptote and the depth variant conversion point decrease with depth

Chapter Six: **Discussion and Conclusions**

6.1 Conclusions

P-S data processing differs from P-P data processing in certain steps. These differences based on the dissimilarity of P and converted S waves characteristics. As a result, different processing approaches are required to achieve the desirable output. We can summarize the conclusions and some of the challenges in the following:

6.1.1 Receiver statics

Shot static correction for P-P and P-S data is the same since the source location in both cases is the same. However, the reflection/conversion points for P-S data are different from those of the P-P data. Thus, receiver static values for P-S data will be different than the ones of the P-P data. Moreover, it is challenging to pick first breaks on the P-S data and calculate refraction velocities as the common practice in the P-P data processing. Therefore, receiver statics are corrected using a non-surface consistent process that requires picking a horizon on the receiver stack, smoothing it, subtracting the smoothed horizon from original and applying these values as receiver static correction.

6.1.2 Velocity analysis

P-wave reflections are stronger than S wave ones. And with the signal enhancement provided by supergather CDPs, it is easier to pick P-wave velocities. That is not the case with P-S data as it is harder to see S-wave reflections.

The first step would be to convert P-wave velocities to S-wave velocities using a constant ratio. And with the help of well velocities to know the velocity trend with depth, picking velocity becomes easier.

6.1.3 Stacking

In P-P data processing, we stack the common-midpoints (CMPs). In P-S data processing however, we either stack the asymptotic common points (ACPs) or the common-conversion points (CCPs) for optimum results.

6.1.4 Synthetic data analysis

Using well velocities and designed wavelets, we were able to convolve the two to create synthetic gathers and stacks that helped us analyse the maximum offsets to include in our binning analysis.

Four survey designs for P-S data were evaluated in terms of fold, offset distribution, azimuth distribution and illumination. As a result, we concluded that re-binning the data to the optimum bins improve all the above attributes considerably.

6.2 Discussion

According to the processing done on both P-P and P-S data sets, we conclude the following:

- Survey design and acquisition parameters of 3C 3D Bigstone give good quality data that could be processed following a conventional processing workflow and give interpretable subsurface images. That is due to the geology of the area without complex structures or steeply dipping layers.

- Calculating receiver statics for this P-S data required good velocity to create the receiver stacks. Velocity had an important impact on this step.
- Radial trace filter is an effective tool to remove noise from P-S data without attenuating signals.
- The velocity analysis for P-S data is challenging and time consuming without having well data. Having sonic log data helps guessing the pattern of the velocity function and saves time testing different velocity trends.
- Using the P-P and P-S processed data, we could tie the events from both stacks and calculate the interval V_p/V_s which could be incorporated in further interpretations.

6.3 Future work

As we saw the effect of re-binning synthetic data on the optimum bins, the same improvement is expected on the real data. Optimum bins will increase the fold and improve the offset and azimuth distribution which as result will improve the stacks. In addition, the re-binned data will make velocity analysis easier and that will result in better stacking velocities.

Another suggestion would be to do a pre-stack time migration and pre-stack depth migration to enhance the imaging of the data.

References

Schafer, A.W., 1992. *A comparison of converted-wave binning methods using a synthetic model of the Highwood Structure, Alberta*. CREWES Research Report, 4.

Canales, L.L., 1984. Random noise reduction. In *SEG Technical Program Expanded Abstracts 1984* (pp. 525-527). Society of Exploration Geophysicists.

Garotta, R., & Grange, P. (1987). Comparison of responses of compressional and converted waves on a gas sand. In SEG Technical Program Expanded Abstracts 1987 (Vols. 1–0, pp. 627–630). Society of Exploration Geophysicists

Guevara, S., 2017. *PS-wave processing in complex land settings: statics correction, wave-mode separation, and migration* (Doctoral dissertation, University of Calgary).

Henley, D.C., 2007b, Radial filtering 3D data, CREWES Research Report, 19

Isaac, J.H., 1996, Seismic methods for heavy oil reservoir monitoring, Ph.D. thesis, University of Calgary, Department of Geology and Geophysics

Lawton, D.C., 1993. Optimum bin size for converted-wave 3-D asymptotic mapping. *CREWES Research Report (University of Calgary)*, *5*(28), pp.1-14.

Liu E. and Martinez A., 2008. Seismic Fracture Characterization, Concepts and Practical applications. EAGE Education Tour Series.

Margrave, G.F., Lamoureux, M.P., Grossman, J.P. and Iliescu, V., 2002. Gabor deconvolution of seismic data for source waveform and Q correction. In *SEG Technical Program Expanded Abstracts 2002* (pp. 2190-2193). Society of Exploration Geophysicists.

Moser, T.J., 1991. Shortest path calculation of seismic rays. *Geophysics*, *56*(1), pp.59-67.

ProMAX, 1997, a reference guide for the ProMAX geophysical processing software. Landmark, a Halliburton Company. Vol. 2.

Richards, P.G. and Aki, K., 1980. *Quantitative seismology: theory and methods* (p. 13). Freeman.

Ronen, J. and Claerbout, J.F., 1985. Surface-consistent residual statics estimation by stack-power maximization. *Geophysics*, *50*(12), pp.2759-2767.

Sheriff, R.E., 2004. what is Deconvolution. *Search and Discovery Article*, *40131*.

Stewart, R.R., Gaiser, J.E., Brown, R.J. and Lawton, D.C., 2002. Converted-wave seismic exploration: Methods. *Geophysics*, *67*(5), pp.1348-1363.

Stewart, R.R., Gaiser, J.E., Brown, R.J. and Lawton, D.C., 2003. Converted-wave seismic exploration: Applications. *Geophysics*, *68*(1), pp.40-57.

Thurston, J.B., Howell, C.E., Lawton, D.C. and Stewart, R.R., 1990. A mode-converted (P-SV) synthetic seismogram. *CREWES Research Report*, *22*, pp.372-386.

Weir, R.M., Eaton, D.W., Lines, L.R., Lawton, D.C. and Ekpo, E., 2018. Inversion and interpretation of seismic-derived rock properties in the Duvernay play. *Interpretation*, *6*(2), pp.SE1-SE14.

Xu, C., 2011. *Oil reservoir assessment using multicomponent seismic data* (Doctoral dissertation, University of Calgary).

Yilmaz, Ö., 2001. *Seismic data analysis: Processing, inversion, and interpretation of seismic data*. Society of exploration geophysicists.

Zelt, C.A., Azaria, A. and Levander, A., 2006. 3D seismic refraction traveltime tomography at a groundwater contamination site. *Geophysics*, *71*(5), pp.H67-H78.

Zoeppritz, K., 1919. Erdbebenwellen vii. *Nachrichten von der Gesellschaft der Wissenschaften zu Göttingen, Mathematisch-Physikalische Klasse*, *1919*, pp.57-65.

Zuleta, L.M. and Lawton, D.C., 2011. PS survey design. In *SEG Technical Program Expanded Abstracts 2011* (pp. 127-131). Society of Exploration Geophysicists.